Optimising the Structure of Metal-Insulator-Metal Diodes for Rectenna Applications

ETOR, DAVID

Optimising the Structure of Metal-Insulator-Metal Diodes for Rectenna Applications

by

David Etor

A Thesis presented for the degree of
Doctor of Philosophy

School of Engineering and Computing Sciences
Durham University

November 2016

Optimising the Structure of Metal-Insulator-Metal (MIM) Diodes for Rectenna Applications

Abstract

The work in this thesis investigates the design and fabrication of metal-insulator-metal (MIM) diodes using an ultrathin organic insulator. The organic insulating layer was found to be compact, highly conformal, and uniform, effectively overcoming the main design challenge in MIM diodes. The fabricated diodes have strong nonlinear current-voltage characteristics with a zero-bias curvature coefficient and a voltage responsivity among the best values reported in the available literature. The fabrication process is simple and carried out at low temperature, which is cost effective, and can potentially be ported to large-area roll-to-roll manufacturing. An encapsulation method to prevent MIM junctions' degradation has also been developed.

Following the successful production of these MIM devices on a rigid substrate, with the fabrication only requiring low-temperature processing, the diodes were successfully fabricated on a flexible substrate with results similar to those fabricated on a rigid substrate. The flexible substrate diodes show no significant degradation in performance when stressed in a one-off bending experiment, although extreme mechanical stress testing does produce some loss in quality.

Also, an elegant method for matching the impedance of an antenna to that of a MIM diode was successfully developed, for optimal external conversion efficiency where the diodes are used in a rectenna device. The responsivity of the impedance-matched rectenna is approaching an order of magnitude higher than that of a control device without a matching network. The fabrication, electrical characterisation and physical analysis of both the MIM diodes and rectennas are discussed in detail in this thesis.

Declaration

I hereby declare that the work carried out in this thesis is based on research performed at the School of Engineering and Computing Sciences, Durham University, UK. No part of this thesis has been previously submitted for any degree and is not currently being submitted in candidature for any other degree. It is all my own work unless referenced to the contrary in the text.

Signed.....

David Etor

Acknowledgements

I would like to extend my sincere gratitude to my supervisors, Prof. David Wood and Dr Claudio Balocco. Without their endless guidance, support, teaching and encouragement I would not have been able to achieve this thesis. I'd also like to thank Dr Linzi E Dodd who took part in supervising me and guided me through many experimental procedures during the early stages of my PhD work. I would also like to thank Dr Mike Cooke and Dr Chris Pearson for their help with AFM analysis, OTS processing and many other processes in the cleanroom. Thank you to Dr Kieran Massey for his help with the cryostat.

My appreciation is also extended to Prof. Damian Hampshire and Dr Mark J Raine for their suggestions and help with the use of their cold-head in Physics department.

I wish to thank all my colleagues I have worked with during the course of my PhD work; you have helped make what has been a very challenging period of my life, interesting and enjoyable from time to time.

I would like to thank my family, especially my wife Mabel for her enormous support and encouragement throughout my time at university. But for her, I probably would have quit in my early days. I thank my son David Jr for arriving just before I finished writing my thesis; his being up at nights crying or cooing kept me awake most of those nights, which was helpful in a way, as I would write while keeping an eye on him.

Finally, I would like to thank God whom I believe granted me good health and sanity throughout the period of my study. Without Him, I ultimately would have not been able to achieve this feat.

Dedicated to

My wife *Mabel Momo Etor* and my son *David Sokoato Etor*

Publications

Journal articles

- D. Etor, L. E. Dodd, D. Wood and C. Balocco, "High-performance rectifiers fabricated on a flexible substrate" *Appl. Phys. Lett.* 109, 193110 November 2016.
- D. Etor, L. E. Dodd, D. Wood and C. Balocco, "An Ultrathin Organic Insulator for Metal–Insulator–Metal Diodes," *IEEE Trans. Electron Devices,* Vol. 63, No 7, pp. 2887–2891, July 2016.
- D. Etor, L. E. Dodd, D. Wood and C. Balocco, "Optimising Power Transfer in Rectennas via Impedance Matching at GHz frequencies" *Manuscript submitted for publication in IEEE Transactions on Microwave Theory and Techniques.*

Conferences

- D. Etor, L. E. Dodd, D. Wood & C. Balocco, "Enhanced Narrow-Band Operation of Ultra-Fast Rectennas," *IRMMW-THz Conf.* M5P.12, Copenhagen, Denmark, September, 2016.
- D. Etor, L. E. Dodd, D. Wood & C. Balocco, "Metal-Insulator-Metal Diodes Fabricated on Flexible Substrates," *IRMMW-THz Conf.* M5P.12, Copenhagen, Denmark, September, 2016.
- D. Etor, L. E. Dodd, D. Wood & C. Balocco, "High Frequency Metal-Insulator-Metal (MIM) Diodes for Thermal Radiation Harvesting," *IRMMW-THz Conf.* Hong Kong, August, 2015.

- D. Etor, L. E. Dodd, D. Wood & C. Balocco, “Impedance Matching At THz Frequencies: Optimizing Power Transfer in Rectennas,” *IRMMW-THz Conf.* Hong Kong, August, 2015.
- D. Etor, L. E. Dodd, D. Wood & C. Balocco, “Novel Low-Cost Ultra-High-Speed Diodes for Electromagnetic Energy Harvesting,“ *URSI Atlantic Radio Sci. Conf.* Gran Canaria, Spain, May, 2015.

Contents

Nomenclature

Abbreviations

RFID	Radio Frequency Identification
PMGI	Polymethylglutarimide
PE	Plasma Etch
RIE	Reactive Ion Etch
ALD	Atomic Layer Deposition
LED	light-emitting-diode
SAM	Self-Assembled Monolayer
MIM	Metal Insulator Metal
TEM	Transmission Electron Microscopy
ToFSIMS	Time of Flight Mass Spectrometry
VNA	Vector Network Analyser
TMA	Trimethylaluminum
OTS	Octadecyltrichlorosilane
PET	Polyethylene Terephthalate
PI	Polyimide
RTA	Rapid Thermal Anneal
AFM	Atomic Force Microscopy
SEM	Scanning Electron Microscope
SE	Schottky Emission

FNT	Fowler-Nordheim Tunnelling
DT	Direct Tunneling
PFE	Poole-Frenkel Emission
HC	Hopping Conduction
PSPD	Position-Sensitive Photo Diode

Symbols

γ	Curvature Coefficient	1/V
γ_{-ZB}	Zero Bias Curvature Coefficient	1/V
V	Applied Voltage	V
R	Resistance	Ω
$R0$	Zero Bias Resistance	Ω
Z_{IN}	Input Impedance	Ω
Z_o	Characteristic Impedance	Ω
R_v	Voltage Responsivity	V/W
f	Frequency	Hz
V_{OUT}	Diode Output Voltage	V
P_{RF}	Radio Frequency Input power	W
f_c	Cut-off Frequency	Hz
V_{DO}	Magnitude of Diode Rectified Voltage	
V_o	Amplitude of RF Input Voltage	V
s_{11}	Reflection Coefficient	dB
R_s	Series Resistance	Ω
C_P	Parallel Capacitance	F
ΔT	Change in Temperature	K
T_{hot}	Hot Temperature	K

T_{cold}	Cold Temperature	K
α_b	Seebeck Coefficient	VK^{-1}
T	Absolute Temperature	K
ρ	Electrical Resistivity	Ωm
k_{th}	Thermal conductivity	$Wm^{-1}K^{-1}$
P_{OUT}	Rectenna Output Power	W
P_{IN}	Input power	W
η_C	Rectenna Efficiency	%
C_D	Diode Capacitance	F
d	Insulator Thickness	m
ε_o	Permittivity of Free Space	Fm^{-1}
ε_i	Insulator Relative Permittivity	
A	Diode junction Area	m^2
N_L	Diode Non-Linearity	AV^{-2}
V_{AC}	AC Input Voltage from Antenna	V
R_D	Diode Resistance at a Given Bias Voltage	Ω
I	Current	A
I_{DC}	DC Current from Diode	A
λ	Wavelength	m
A^*	Effective Richardson Constant	$Am^{-2}K^{-2}$
m_0	Free Electron Mass	kg
m^*	Effective Electron Mass in Metal	kg
q	Electron Charge	C
ϕ_B	Schottky barrier height	eV
k_B	Boltzmann's Constant	JK^{-1}
h	Planck's constant	Js

J	Current Density	Acm^{-2}
J_{SE}	Schottky Emission Current Density	Acm^{-2}
m_T^*	Tunneling Effective Mass in Dielectric	kg
J_{DT}	Direct Tunnelling Current Density	Acm^{-2}
J_{FNT}	Fowler-Nordheim Tunnelling Current Density	Acm^{-2}
ϕ_T	Trap Energy Level	eV
J_{PFE}	Poole-Frenkel Emission Current Density	Acm^{-2}
a	Mean Distance between Trap Sites	m
n	Electron Concentration in Conduction Band of Insulator	m^{-3}
E_a	Activation Energy	J
R_A	Antenna Resistance	Ω
Υ_P	Wave Propagation Constant	
α	Radiation Attenuation Constant	Np/m
β	Wave Propagation Speed	m/s
Z_L	Load Impedance	Ω
k	Phase Constant	rad/m
x	Transmission Line Length	m
Z_S	Source Impedance	Ω
Z_{eq}	Equivalent Impedance	Ω
Y_L	Transmission Line Admittance	S
G_L	Transmission Line Conductance	1/Ω
B_L	Transmission Line Susceptance	S

Chapter 1

Introduction and Aims

1.1 Introduction

The rectenna is a device consisting of a rectifier coupled with an antenna, which can convert electromagnetic radiation into DC electrical power [1-3]. This device is generating enormous interest for potential applications, including high frequency signals rectification, thermal imaging, the detection of terahertz radiation, and the recovery of heat energy [2-4]. This is due to the ability of the device to operate at ultra-high frequencies given the existence of broadband antennas which can operate within a wide range of frequencies. Fast rectifiers, such as metal-insulator-metal (MIM) junctions, Schottky diodes, and more recently the self-switching nanodiodes, are often used as the rectifying component [4-6] due to their ability to operate at frequencies well into the terahertz range.

The major drawback of the rectenna device, however, is the relatively low external conversion efficiency, caused mainly by the mismatch between the impedance of the rectifier and that of the antenna [6].

Although there are varieties of devices that can be used as the rectifying component for the rectenna, this work will focus on the production of the MIM diode. This consists of two metals separated by a thin insulating layer (only a few nm thick), corresponding to only a

few atomic layers. With the conventional deposition methods [7-9], this often results in a defective layer [8-9], with a large number of pin holes, short-circuiting the diode terminals and drastically reducing yield. To overcome this problem, this thesis presents the development of a new technique for the manufacturing of MIM diodes. The technique involves a low temperature process, where the insulator self-assembles in a monolayer onto a metal surface. The low temperature process not only provides reduced production costs, but also allows the fabrication of diodes onto a flexible plastic substrate, which is an added advantage particularly in the emerging field of plastic electronics where flexibility is a key property. The materials used in this process are safe and can be dispose of easily.

Also, this work presents a simple and elegant method for matching the impedance of an antenna to a rectifier with a relatively high impedance, for optimal rectenna external conversion efficiency. The fabrication, electrical characterisations and physical analysis of both the MIM diodes and rectennas are discussed in detail in this work.

1.2 Thesis structure

Chapter 1: This chapter introduces the thesis, outlines the motivation and aims of the research and also summarises the content of each subsequent chapter.

Chapter 2: This chapter discusses the theory of the MIM diode, which includes the working principle of the device, and the parameters that influence the operation. Furthermore, the design and fabrication considerations, which affect the conduction mechanisms that may occur in the diode during operation, are also discussed.

Chapter 3: This chapter discusses the existing and potential applications where the MIM diode can be used, including electromagnetic energy harvesting, high-frequency detection, mixers and radio frequency identification (RFID) applications. Other existing electromagnetic energy harvesting technologies are also discussed in order to clearly

highlight the viability of the MIM diode technology, and the new possibilities opened up in the advancement of these applications, in a world where devices are being miniaturised and need to operate at higher frequencies and be more efficient.

Chapter 4: This chapter discusses the techniques employed in fabricating and characterising the MIM diodes both electrically and physically. The electrical analysis includes the diodes' *J-V* characteristics where associated common figures of merit, including curvature coefficient and resistance are discussed in detail.

Chapter 5: This chapter discusses the fabrication and tests of MIM diodes using octadecyltrichlorosilane (OTS) as the insulator which self-assembles as a monolayer on a metal surface. The diodes fabrication processes and electrical analysis are discussed. An encapsulation method to prevent the degradation of rectified current associated with the MIM diodes has also been developed, and is discussed in detail.

Chapter 6: This chapter discusses the manufacture of Ti/OTS/Pt MIM diodes on a flexible substrate formed using polyimide (PI). The PI substrate formation, electrical analysis of the fabricated diodes, which includes asymmetry, *J-V* characteristics, yield and lifetime reliability are all discussed in detail.

Chapter 7: This chapter discusses the fabrication and electrical DC characterisation, including current density, curvature coefficient, current ratio, and yield of MIM diodes with Al_2O_3 insulator, deposited using the atomic layer deposition (ALD). The comparisons of the diodes' DC electrical results with those of the OTS insulator diodes are discussed.

Chapter 8: This chapter discusses the production of a rectenna and the development of an elegant impedance-matching method for narrowband rectennas. The impedance-matching method used two coplanar strip lines emerging from the antenna feed-point, to correct for the reactive component of the antenna impedance on one side, and to connect the rectifier

and transform its impedance on the other side. Numerical simulations considering a model rectenna with a MIM diode with impedances up to several kΩ were effectively matched, and are discussed. Also, microwave characterisation of the fabricated devices (impedance-matched and non-matched) is discussed.

Chapter 9: This chapter provides the conclusions drawn from this work and makes suggestions for potential further investigations.

1.3 Thesis Aims

One of the aims of this project is to investigate the use of an alternative method for creating a thin insulator for MIM diodes, rather than the conventional methods used, which often result in the production of defective thin films. An OTS self-assembled monolayer (SAM), which consists of carbon chains that are strongly packed together (pin-hole free) with an overall thickness of approximately 2 nm [10-12] will be explored as an alternative method of producing an insulating layer. The material (OTS) self-assembles in a monolayer onto a metal surface, and due to the nature of self-assembly, a second layer cannot grow on top of the first one, resulting in an extremely uniform thickness over large areas determined by the SAM chemistry. The uniformity associated with this material when deposited is expected to significantly improve the rectification capability of the diodes and the uniformity of electrical results between different diodes.

Another aim of this work is to manufacture MIM devices on a flexible plastic substrate. This will be on the back of the successful production of the OTS diodes, since the OTS deposition is a low temperature process.

Furthermore, this thesis aims to develop an effective impedance-matching method for matching the impedance of an antenna to that of a rectifier in order to improve power

transfer between the two components, which will result in a more efficient rectenna device.

References

[1] W. C. Brown, “The History of Power Transmission by Radio Waves,” *IEEE Trans. Microwave Theory Tech.* Vol. MTT-32, No. 9, pp. 1230-1242, (1984).

[2] R. E. Drullinger, K. M. Evenson, D. A. Jennings, F. R. Petersen, J. C. Bergquist, L. Burkins, and H.U. Daniel, “2.5 THz Frequency Difference Measurements in the Visible Using Metal-Insulator-Metal Diodes,” *Appl. Phys. Lett*. Vol. 42, pp. 137-138, (1983).

[3] K. J. Siemsen and H. D. Riccius, “Experiments With Point-Contact Diodes in the 30-130 THz Region,” *Appl. Phys. Lett*. *A*, Vol. 35, pp. 177-187, (1984).

[4] Y. Pan, C. V. Powell, A. M. Song, and C. Balocco, “Micro Rectennas: Brownian Ratchets for Thermal-Energy Harvesting”, *Appl. Phys. Lett*. Vol. 105, 253901, (2014).

[5] C. H. Lee and Y. H. Chang, “Design of a Broadband Circularly Polarized Rectenna for Microwave Power Transmission”, *Microwave and Optical Technol. Lett.* Vol. 57, pp. 702-706, (2015).

[6] J. L. Hesler and T. W. Crowe, “NEP and Responsivity of THz Zero-Bias Schottky Diode Detectors”, *32nd Int. Conf. Infrared Millimeter Waves (IRMMW),* pp. 844-845, (2007).

[7] L. E. Dodd, A. J. Gallant, and D. Wood, “Ti-TiOx-Pt Metal-Oxide-Metal Diodes Fabricated via a Simple Oxidation Technique”, *MRS Proceedings*, Vol. 1415, pp. 1-4, (2012).

[8] L. E. Dodd, A. J. Gallant, and D. Wood, “Controlled Reactive ion Etching and Plasma Regrowth of Titanium Oxides of Known Thickness for Production of Metal-Oxide-Metal Diodes”, *IET Micro and Nano Letters*, Vol. 8, No. 8, pp. 476-478, (2013).

[9] L. E. Dodd, “Fabrication Optimization of Metal-Oxide-Metal Diodes”, *PhD thesis*, pp 127-132, http://etheses.dur.ac.uk/9474/1/Linzi_Dodd_d51hqe_thesis.pdf?, Accessed online: 04 July 2016.

[10] S. Rena, S. Yanga, Y. Zhaob, J. Zhoua, T. Xua and W. Liu, “Friction and Wear Studies of Octadecyltrichlorosilane SAM on Silicon”, *Tribology Letters*, Vol. 13, Issue 4, pp 233-239, (2002).

[11] K. H. Cha, and D. E. Kim, “Investigation of the Tribological Behavior of Octadecyltrichlorosilane Deposited on Silicon” *Wear*, Vol. 251, Issues 1–12, pp 1169–1176, (2001).

[12] Y. Liu, L. K. Wolf, and M. C. Messmer, “A Study of Alkyl Chain Conformational Changes in Self-Assembled n-Octadecyltrichlorosilane Monolayers on Fused Silica Surfaces”, *Langmuir,* Vol. 17 Issue 14, pp 4329–4335, (2001).

Chapter 2

Metal – Insulator – Metal (MIM) Diode Theory

2.1 Introduction

This chapter discusses the theory of the MIM diode which includes how the diode operates, and the parameters that influence the operation. Furthermore, the design and fabrication considerations, which affect the conduction mechanisms that may occur in the diode during operation, are also discussed.

2.2 MIM diode operation

The Metal–Insulator–Metal (MIM) diode is an ultra-fast switching device capable of operating well into the terahertz frequency range, made possible by the use of the quantum tunneling effect – a promise which was highlighted over thirty years ago, but which could not be implemented properly at the time due to fabrication difficulties [1-5].

The MIM diode consist of a thin dielectric layer sandwiched between two (base and top) metal electrodes as shown in Figure 2.1, where electrons flow from one metal electrode to the other in a direction relative to polarity, through the dielectric film [6-7].

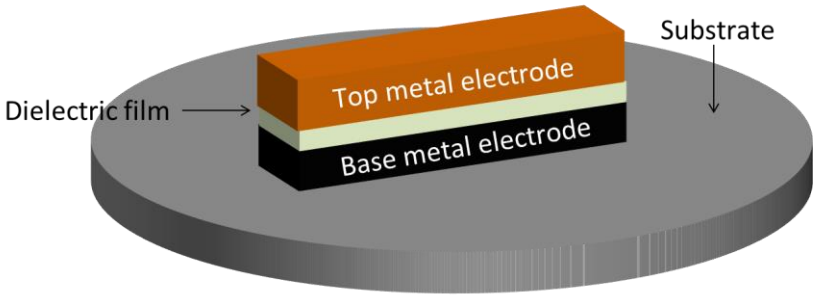

Figure 2.1 – Schematic of a metal–insulator–metal structure.

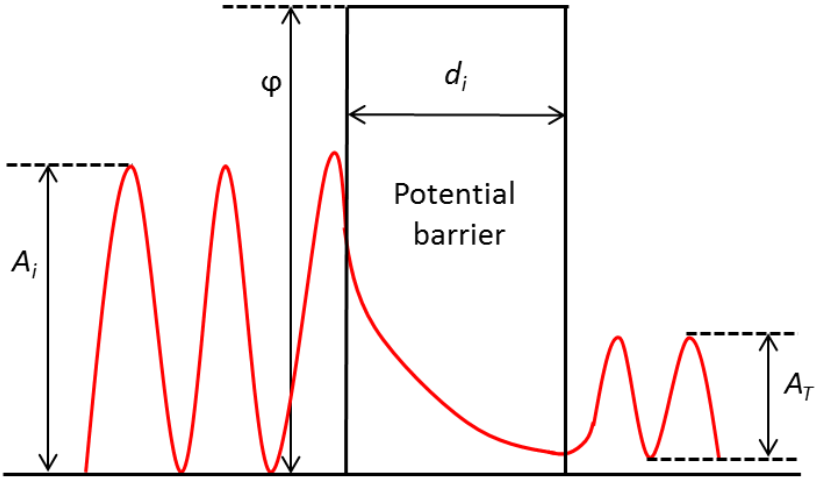

Figure 2.2 – Incident electron wave function with the energy of the electrons less than that of the potential barrier φ, being transmitted through the barrier (quantum mechanism). The amplitude of the transmitted wave A_T is attenuated to A_i due to reflection.
d_i is the thickness of the potential barrier.

In classical mechanics, electrons cannot traverse from one electrode to another, through a barrier, if the energy of the incident electron is less than that of the potential barrier. This is in contrast with quantum mechanics, which states that an incident particle with energy, less than that of a potential barrier, has the probability of tunneling through the potential barrier if the barrier is sufficiently thin [8]. As can be seen in Figure 2.2, an incident electron wave function tunnels through a potential barrier and surfaces at the other end with the same frequency but reduced amplitude. It is worth noting that the probability of the quantum mechanical tunneling has an exponential dependence on the thickness of the

potential barrier, as can be seen in Figure 2.2 where the electron wave decays exponentially as it travels through the barrier. This highlights the importance of the thickness of the potential barrier; as if not sufficiently thin the electron wave is likely to decay to zero level before it is able to travel to the other end – in which case, tunneling has not taken place. The thickness of the potential barrier needs to be <5 nm for there to be a possibility of tunneling occurring [9]. The inherent high speed (which depends on the thickness and dielectric constant of a potential barrier) of the MIM diode due to the tunneling effect is the main reason the device is attracting much attention by researchers for energy harvesting, detection devices etc. [10-12].

2.3 Design considerations

The diode may have a symmetric or asymmetric *J-V* characteristic depending on the shape of the tunneling barrier, which is to a large extent determined by a number of factors, including the work function difference between the two metal electrodes utilised [13]. Dissimilar electrodes create different energy barrier heights at each electrode-barrier interface due to the work function difference. As a result, an asymmetric tunneling current is generated [13-14]. Although in theory the diode *J-V* characteristic is symmetric if the work function of the two metal electrodes is the same as shown in Figure 2.3(a), (and asymmetric if the work function is dissimilar as shown in Figure 2.3(b)), in reality, the diode is unlikely to have a symmetrical *J-V* characteristic despite the work function of the two metal electrodes being the same, due to the roughness of the surface of the crystalline metal film when deposited, which is often large enough to cause imperfection of the metal-insulator interface across the diode junction area [14-15].

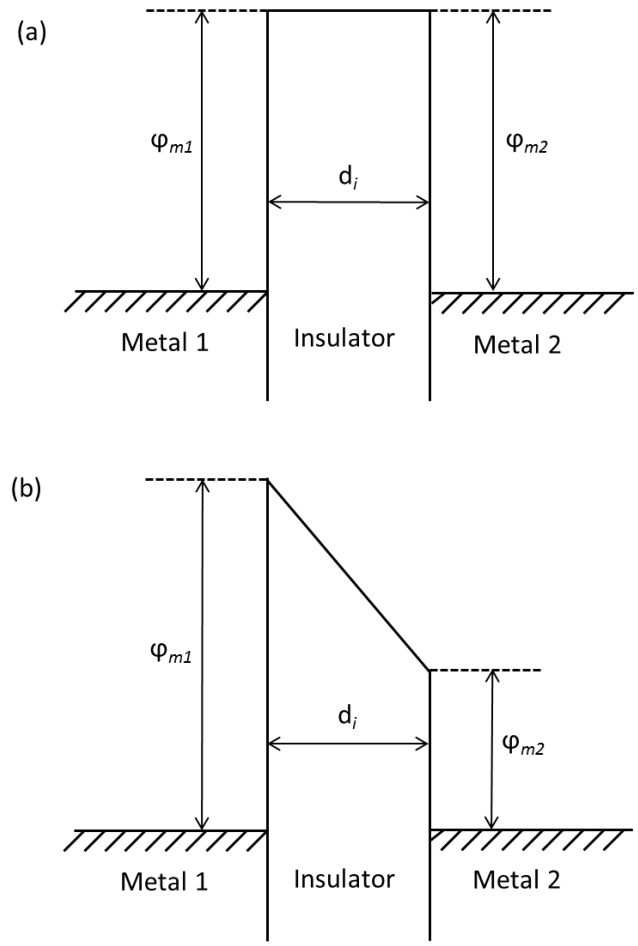

Figure 2.3 – (a) Schematic energy band diagram showing how the work functions of metal electrodes provide a symmetric tunneling barrier and (b) asymmetric tunneling barrier. φ_m and d_i are the barrier height and barrier thickness respectively.

Some other groups have proposed that the problems associated with the roughness of the surface of the crystalline metal film can be significantly reduced by utilising amorphous metals, which are said to have lower surface roughness when deposited on a substrate [8, 16].

In applications such as energy harvesting and detection, it is best that the diode has an asymmetric *J-V* characteristic, as this can be further optimised to operate the diode without the need for an externally applied bias [13].

The MIM diode junction can be considered as a parallel plate capacitor with its capacitance expressed as [11]:

$$C_D = \varepsilon_i \varepsilon_o \frac{A}{d} \tag{2.1}$$

where ε_i is the relative dielectric constant of the insulator, ε_o is the dielectric constant of free space, A is the junction area of the structure, and d the insulator thickness.

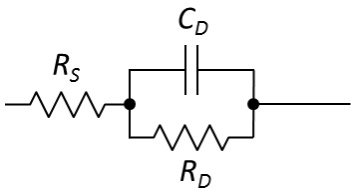

Figure 2.4 – Basic MIM diode junction circuit diagram, with R_S being series resistance from a connecting lead, C_D and R_D in parallel denoting the diode. C_D is the capacitance of the diode, and R_D the resistance of the diode.

The absolute value of the capacitor impedance $|Z_C|$ decreases as the frequency of the circuit (shown in Figure 2.4) input signal increases, as expressed in Equation 2.2 [10].

$$|Z_C| = \left|\frac{1}{2\pi f C_D}\right| \tag{2.2}$$

If the frequency is high enough, $|Z_C|$ will become much less than the resistance R_D, hence the circuit can be approximated as the series between R_S and R_D, meaning that Equation 2.3 is true, where capacitance has a significant effect on the diode's response time. With a larger capacitance, the diode's response time increases, hence reducing the cut-off frequency, as expressed in Equation 2.3 [10].

$$f_c = \frac{1}{2\pi R_S C_D} \tag{2.3}$$

In order to maximise the diode cut-off frequency, the diode capacitance musts to be very small. This can be achieved by making the diode junction area smaller (sub-100 nm^2 to obtain a cut-off frequency higher than 30 THz). If the diode is to be used for a narrow frequency band rectenna application, the diode junction area dimension is not significant, as the capacitance can be eliminated by matching the impedance of the diode with the impedance of the antenna, meaning that, theoretically, the diode's cut-off frequency becomes infinite. Impedance matching is discussed in detail in Chapter 8.

2.4 Technological challenges

Historically, the first high speed MIM like diodes were produced using a thin metallic wire (mostly tungsten) with its tip sharpened to a small area and in contact with an oxide layer (which serves as the insulator) formed on top of a metal surface as can be seen in Figure 2.5.

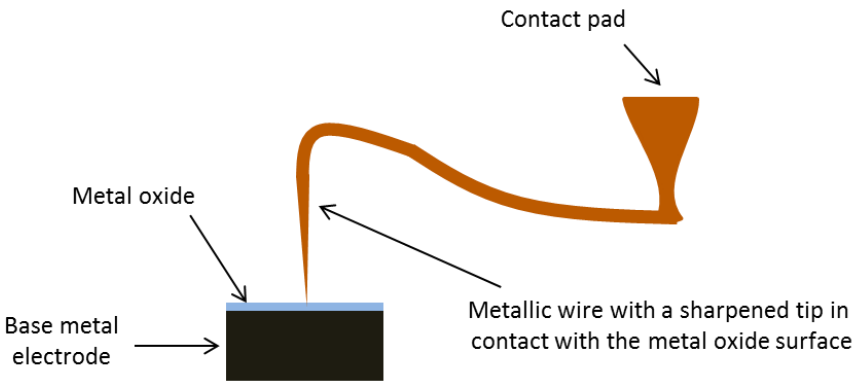

Figure 2.5 – Schematic diagram of a point-contact diode.

This type of structure is known as a point-contact diode. The fabrication technique used allowed for an extremely small junction area to be created in a relatively straightforward manner. The only part that needs to be thinned to the desired diode junction area

dimension is the tip of the top metallic wire, and this can be performed either chemically [17] or electrically [5]. Fabricated point-contact MIM diodes, as in [1, 4-5], had good electrical results, but were limited by the point-contact which had a poor mechanical stability. It is non-trivial to maintain a stable contact between the thinned metallic wire tip and the oxide layer without damaging the device. The mechanical instability associated with this structure affects its performance significantly. A mechanical improvement on the point-contact structure is the planar thin-film diode. The planar structure consists of two overlapping metal strips, separated by a thin dielectric layer, as shown in Figure 2.6. The parts and fabrication process involved with the planar structure are similar to those of the point-contact diode, except for the top metal electrode. While the top electrode of the point-contact diode is a thinned metallic wire, that of the planar structure is a metal strip deposited in the same manner as the bottom metal electrode. The major drawback with this technique however is the difficulty in successfully defining the required extremely small overlap area which forms the diode junction, in a manner that is quick and cost effective.

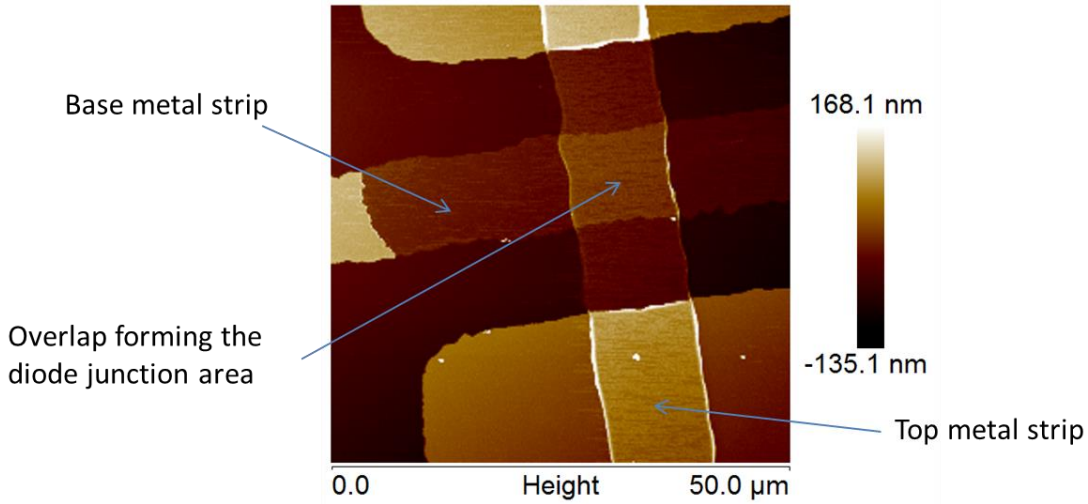

Figure 2.6 – AFM picture showing a planar MIM diode crossover.

2.5 Metal electrode strips considerations

As stated in Section 2.3, the diode's properties, with regards to its *J-V* characteristics (i.e. being symmetric or asymmetric), can be largely determined by the choice of metals utilised, and their nature (i.e. roughness or uniformity) when deposited. The base metal strip needs to be that which can be readily oxidised if the choice of technique for forming the dielectric layer onto the metal is by growing it. In which case, if metals such as titanium and aluminium are chosen, in order to ensure repeatability and the production of a high quality film, an initial etch process must take place in a controlled manner before the growth of the desired thickness of the dielectric layer (which in most cases is an oxide). This needs to occur in order to remove any native oxide, which may have formed on the metal surface, as these type of metals rapidly form a thin (a few nanometres) native oxide when in the presence of air. However, if the formation of the dielectric layer is by deposition, then a metal, irrespective of its properties relative to the atmosphere, can be used as the base metal because the dielectric film formed in this manner is not dependent on the base metal. The deposition technique is easier and more reliable, as an inert metal can be used as the base metal, in which case this will ensure that no native oxide is formed on the metal prior to the deposition of the desired thickness of the dielectric layer.

2.6 Insulating layer considerations

Apart from the size of the diode junction area, which, to a large extent, determines the diode's response in terms of cut-off frequency, another very important part of the diode is the insulating layer. The thickness and quality (i.e. roughness and uniformity) of the insulator affects the nature of the diode's responses including the current it is able to rectify and the conduction mechanisms that occur within. The quality of the insulating layer is partly determined by the quality of the metal film underneath it and largely determined

by the method used in forming it. If the surface of the base metal on which the insulating layer is being formed is rough, due to the nanometre scale thickness of the insulating film, the insulating layer is most likely to have similar defects.

There are two main ways of producing the insulating layer: growth and deposition. The common methods for growing the layer (mostly oxides) include exposure of a base metal to elevated temperature environments (i.e. furnace oxidation), and plasma oxidation, where a metal oxide is produced at the end of the process. Another method is by immersing a base metal in a solution of a Self-Assembled-Monolayer (SAM), with the details explained in Section 4.4.4, and allowing the SAM to form on the metal. In addition, e-beam evaporation, atomic layer deposition (ALD) or sputtering can be used for depositing the dielectric layer. The ALD can also be used for depositing an organic insulating layer.

The deposition technique is a preferred option with regards to the production of an insulating film on a surface, as it means that the deposited layer is independent of the base metal, thus providing significant flexibility in production. However, using e-beam evaporation or sputtering for the deposition of a very thin layer (a few nanometres) of smooth and uniform insulating film can be problematic due to the lack of reproducibility. However, for relatively thick (above 7 nm) dielectric films, these methods have been reported to work well [22, 23]. One possible technique for producing very thin and high quality layers is atomic layer deposition (ALD), which allows uniform deposition of varieties of materials down to thicknesses less than 3 nm in a repeatable manner [24-30].

The nature and quality of a dielectric layer is dependent on the surface it is being produced on, and the production technique used. However, it is worth nothing that it is possible to successfully alter an existing metal oxide dielectric layer to have more desirable features. The main method for achieving this is either by thermal or via electrical annealing. For example, annealing can be used to remove defects in oxide layers [31], to alter the

stoichiometry [32], or to alter the roughness [33]. Furthermore, annealing can also be used to alter the devices and their associated conduction mechanisms [32]. For example, in [34], Fowler-Nordheim conduction in GaN diodes was converted to Poole-Frenkel conduction via exposure to hydrogen, due to hydrogen's ability to alter the charge at the metal-insulator interface thus changing the barrier height.

2.7 DC characterisation of MIM diodes

Curvature coefficient γ, expressed in Equation 2.4 [10, 17], is a Figure of merit used to characterise the MIM structure. It is the ratio of the second derivative to the first derivative of the diode's *J-V* curve, and is typically used in quantifying the non-linearity of the structure's *J-V* characteristics at a given voltage.

$$\gamma = N_L R|_{V=V_g} \tag{2.4}$$

where N_L is the second derivative (non-linearity) of the diode at a given voltage V_g, as expressed in Equation 2.5.

$$N_L = \frac{d^2 I}{dV^2}\Big|_{V=V_g} \tag{2.5}$$

and R the diode resistance at a given voltage V_g, defined by Equation 2.6.

$$R = \left(\frac{dI}{dV}\right)^{-1}\Big|_{V=V_g} \tag{2.6}$$

The parameters stated above can be obtained directly via electrical measurement or from polynomial fitting to the diode *I-V* characteristics raw results.

2.8 MIM diode as a detector

Where the diodes are used in applications such as high-frequency detection, as can be seen on Figure 2.7, where the diodes may be coupled with an antenna, the high-frequency voltage coming from the antenna to the diode is small; consequently, the nonlinearity of the diode is also low.

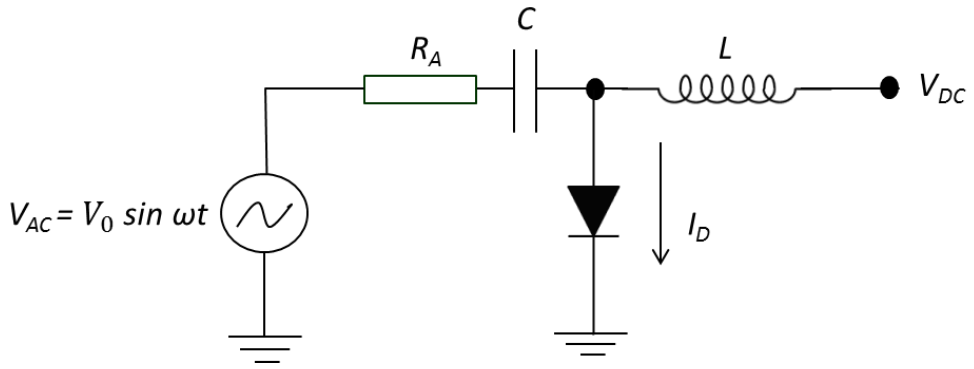

Figure 2.7 – Basic circuit diagram of a detector (adapted from [17]). R_A depicts an antenna, *C* a capacitor, which means an antenna can neither radiate nor receive a DC signal. *L* is an inductor due to the leads which is considered as an open circuit to an AC signal.

At lower voltage regimes, the total diode rectified current is best approximated using a Taylor series expansion. The diode total current is therefore expressed in Equation 2.7 as:

$$I_{Tot} = I(V_{DC}) + \frac{dI}{dV}\Big|_{V_{DC}} . V_{AC} + \frac{1}{2}\frac{d^2I}{dV^2}\Big|_{V_{DC}} . {V_{AC}}^2 + \cdots \tag{2.7}$$

where

$$V_{AC} = V_0 \sin \omega t \tag{2.8}$$

is the sinusoidal voltage fed into the diode by the antenna, and V_0 is the amplitude of the sinusoidal voltage. This implies that:

$$V_{AC}{}^2 = V_0{}^2 \sin^2 \omega t \tag{2.9}$$

Therefore Equation 2.7 becomes:

$$I_{Tot} = I(V_{DC}) + \frac{dI}{dV}\Big|_{V_{DC}} . V_0 \sin \omega t + \frac{1}{2}\frac{d^2I}{dV^2}\Big|_{V_{DC}} . V_0{}^2 \sin^2 \omega t + \cdots \tag{2.10}$$

In order to obtain the diode DC current (I_{DC}), the sinusoidal components present in I_{Tot} are averaged. The first derivative term becomes insignificant, as $\overline{V_0 \sin \omega t} = 0$, whereas $\overline{V_0{}^2 \sin^2 \omega t} = \frac{V_0{}^2}{2}$. Therefore, the diode DC current can be expressed as:

$$I_{DC} = I(V_{DC}) + \frac{V_0{}^2}{4}\frac{d^2I}{dV^2}\Big|_{V_{DC}} \tag{2.11}$$

If the diode is used at zero-bias, then $I(V_{DC}) = 0$, hence;

$$I_{DC} = \frac{V_0{}^2}{4}\frac{d^2I}{dV^2}\Big|_{V_{DC}} \tag{2.12}$$

By factoring in the RF power [17];

$$P_{RF} = \frac{V_0{}^2}{4R} \tag{2.13}$$

being fed the diode (by the antenna), then the diode DC current becomes:

$$I_{DC} = \frac{V_0{}^2}{4R_D} . \frac{d^2I}{dV^2} \Big/ \frac{dI}{dV} \tag{2.14}$$

The diode voltage is expressed as [17]:

$$I_{DC} = \frac{V_0{}^2}{4} . \frac{d^2I}{dV^2} \Big/ \frac{dI}{dV} \tag{2.15}$$

In summary, in manufacturing metal-insulator-metal (MIM) diodes for rectifying applications, the work function difference between the metals chosen needs to be maximised [19-20], a uniform dielectric layer that is sufficiently thin (a few nm) needs to be deposited for a higher probability of electron tunnelling occurring within the structure [19, 21]. Furthermore, the size of the diode junction needs to be reduced significantly (to nanometer dimensions) in order to maximise the diode's cut-off frequency.

2.9 Conduction mechanisms in MIM diodes

As mentioned earlier, in a MIM structure, electrons flow from one metal electrode to the other through the insulating layer between the metals depending on the bias voltage polarity and the difference in the metal work functions. This makes the insulating layer a significant part of the MIM diode. Here the conduction mechanisms responsible for transporting electrons through the insulator are discussed. The conduction mechanisms are in two categories, namely; the electrode-limited and bulk-limited conduction mechanisms [35]. The electrode-limited conduction mechanisms depend on the electrical properties of the electrode-dielectric interface, i.e. the height of the barrier located at the electrode-dielectric interface. Electrode-limited conduction mechanisms include Schottky (thermionic) Emission (SE), Fowler-Nordheim Tunnelling (FNT) and Direct Tunneling (DT). The bulk-limited conduction mechanisms include Poole-Frenkel Emission (PFE) and Hopping Conduction (HC). These mechanisms depend only on the electrical properties of the dielectric [35]. Figure 2.8 illustrates how these conduction mechanisms can be classified.

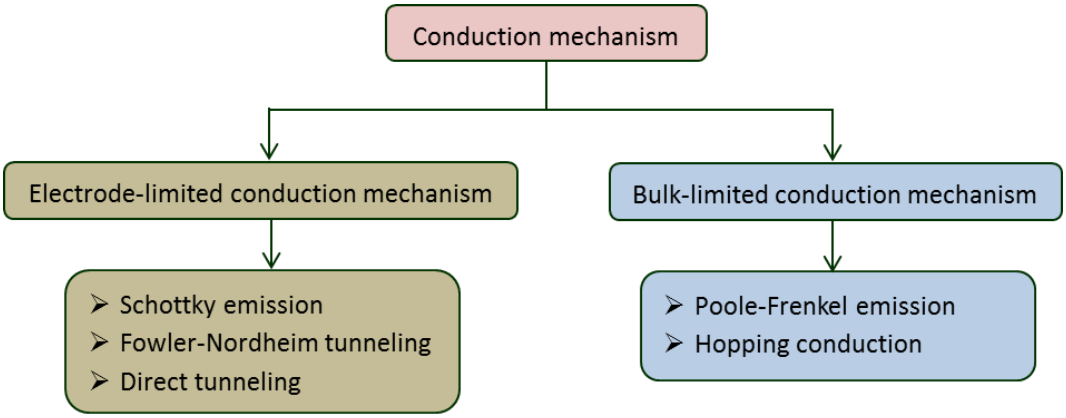

Figure 2.8 – Classification of conduction mechanisms in dielectric films (adapted from [35]).

Distinguishing the various conduction mechanisms that may occur in the diode is essential, as it gives an insight on how fast the diode switches at different operating conditions, such as applied voltage and temperature. Also, a number of conduction mechanisms may sometimes jointly contribute to the transport of current through the dielectric layer.

2.9.1 Electrode-limited conduction mechanisms

The electrode-limited conduction mechanisms depend mainly on the electrical properties of the electrode-dielectric interface. The mechanisms in this class are discussed below.

2.9.1.1 Schottky Emission

Schottky Emission (SE) is a conduction mechanism which occurs by the influence of thermal energy. If charge carriers (electrons) in an electrode are thermally induced well enough, the electrons possess a high probability of overcoming the energy of the barrier at the electrode-dielectric interface and proceed to the conduction band of the dielectric [35]. Figure 2.9 shows a schematic MIM energy band diagram illustrating this type of conduction mechanism.

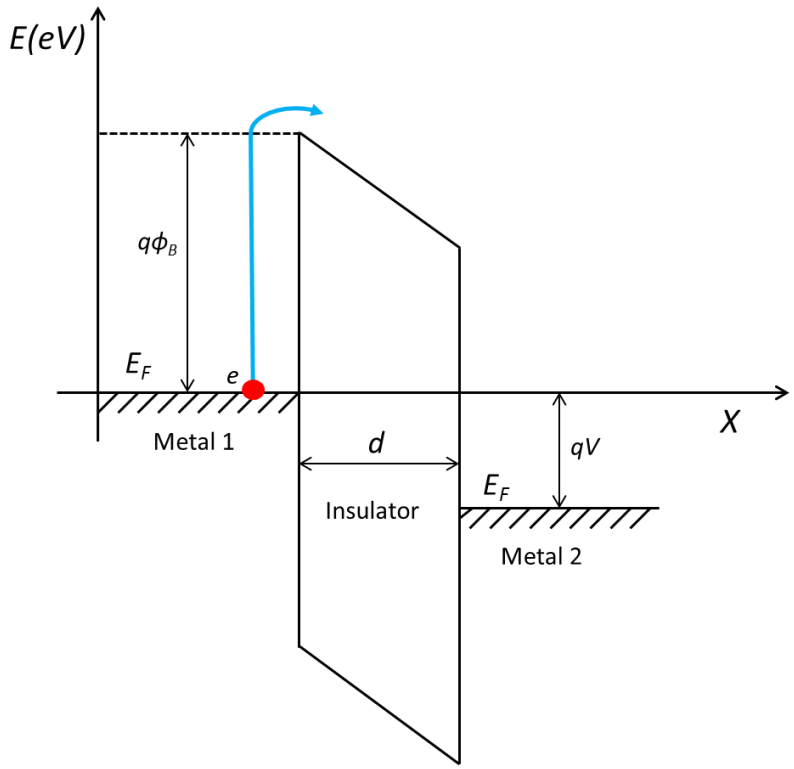

Figure 2.9 – Energy band diagram of Schottky emission occurring in a MIM structure under bias. $q\phi_B$ is the barrier height at the metal-insulator interface, E_F is the Fermi level, *d* is the insulator thickness, *qV* is the bias voltage and *e* represents an electron (adapted from [35]).

SE is most often the conduction mechanism which occurs in metal-insulator interfaces, especially at relatively high temperatures. The Schottky emission, which occurs in a MIM structure, is expressed as [35, 36]:

$$J_{SE} = \left\{A^* T^2 \exp\left[\frac{-q(\phi_B - \sqrt{qV/4\pi\varepsilon_i\varepsilon_0})}{k_B T}\right]\right\} - \left\{A^* T^2 \exp\left[\frac{-q(\phi_B + \sqrt{qV/4\pi\varepsilon_i\varepsilon_0})}{k_B T}\right]\right\} \quad (2.16)$$

where

$$A^* = \frac{4\pi q {k_B}^2 m^*}{h^3} = \frac{120 m^*}{m_0} \quad (2.17)$$

A^* = effective Richardson constant

m_0 = free electron mass

m^* = effective electron mass in dielectric

T = absolute temperature

q = electronic charge

$q\phi_B$ = Schottky barrier height

k_B = Boltzmann's constant

h = Planck's constant

Equation 2.6 can be interpreted as a current density $A^*T^2\exp\left[\frac{-q(\phi_B-\sqrt{qV/4\pi\varepsilon_i\varepsilon_0})}{k_BT}\right]$ flowing from metal-1 to metal-2, and another, $A^*T^2\exp\left[\frac{-q(\phi_B+\sqrt{qV/4\pi\varepsilon_i\varepsilon_0})}{k_BT}\right]$ flowing from metal-2 to metal-1 [36].

Where a typical SE has occurred, the plot of In(J/T^2) as a function of $V^{1/2}$ should be linear, and is best tested for at a high temperature and low voltage [37].

2.9.1.2 Direct Tunnelling

Direct Tunnelling (DT) is a fast conduction mechanism and relies on a quantum mechanical effect, where electrons tunnel through the full barrier thickness even when the applied bias is very small (i.e. V<ϕ_B) [35]. The tunnelling of the electrons through the full barrier thickness, as illustrated in Figure 2.10, is made possible by a barrier or insulator that is without defects and is sufficiently thin (typically <4 nm) [8]. In which case, the DT conduction mechanism dominates the flow of current in the MIM structure [8, 35, 37]. DT can be tested for in a structure by measuring the *J-V* characteristic of the structure at low temperature (e.g. <30 K) where thermionic emission is sufficiently suppressed, and plotting In(J/V^2) as a function of 1/V. The resultant plot should be linear at points where the applied voltage is very low (in few mV). The expression for the direct tunneling current is given as [36, 38]:

$$J_{DT} = J_0\left[\left\{\phi_B \exp\left(-A_S\sqrt{\phi_B}\right)\right\} - \left\{(\phi_B + V)\exp\left(-A_S\sqrt{\phi_B + V}\right)\right\}\right] \quad (2.18)$$

where

$$J_0 = \frac{q^2}{2\pi h {d_i}^2} \quad (2.19)$$

$$A_S = \frac{4\pi d_i\sqrt{2qm^*}}{h} \quad (2.20)$$

d_i is the thickness of the dielectric film, and all other terms are as defined previously.

As with the SE current density, Equation 2.18 can be interpreted as a current density $J_0\left[\phi_B \exp\left(-A_S\sqrt{\phi_B}\right)\right]$ flowing from metal-1 to metal-2, and another, $J_0\left[(\phi_B + V)\exp\left(-A_S\sqrt{\phi_B + V}\right)\right]$ flowing from metal-2 to metal-1 [36].

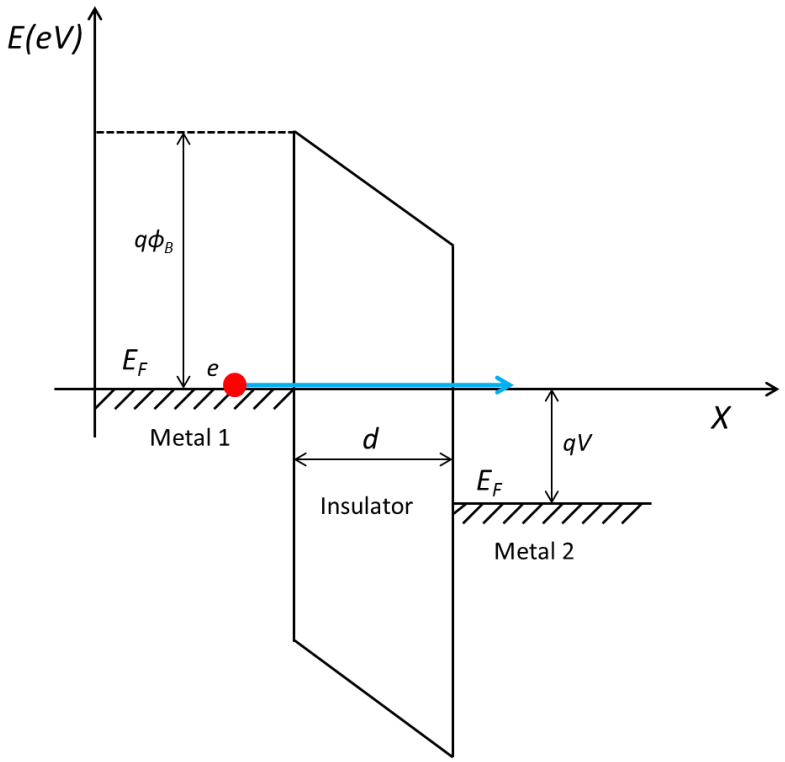

Figure 2.10 – Schematic MIM energy band diagram of direct tunneling tunnelling conduction mechanism (adapted from [35]).

2.9.1.3 Fowler-Nordheim Tunnelling

Fowler-Nordheim Tunnelling (FNT) is another ultra-fast conduction mechanism similar to DT, which occur in MIM structures. But unlike the DT where current flows from one electrode to the other through the full insulator thickness due to a very thin insulator, FNT occurs when the insulator thickness is large (>5 nm) and the applied bias is much larger (Volts) than the barrier height $q\phi_B$. The large applied bias causes the incident electrons on the insulator to have a high energy, enough to shrink the thick insulator (making it have a triangular shape), and penetrate into its conduction band [35] as shown in Figure 2.11. FNT is faster than DT because here electrons flow through a barrier with thickness, significantly reduced due to the shrinking caused by the large bias.

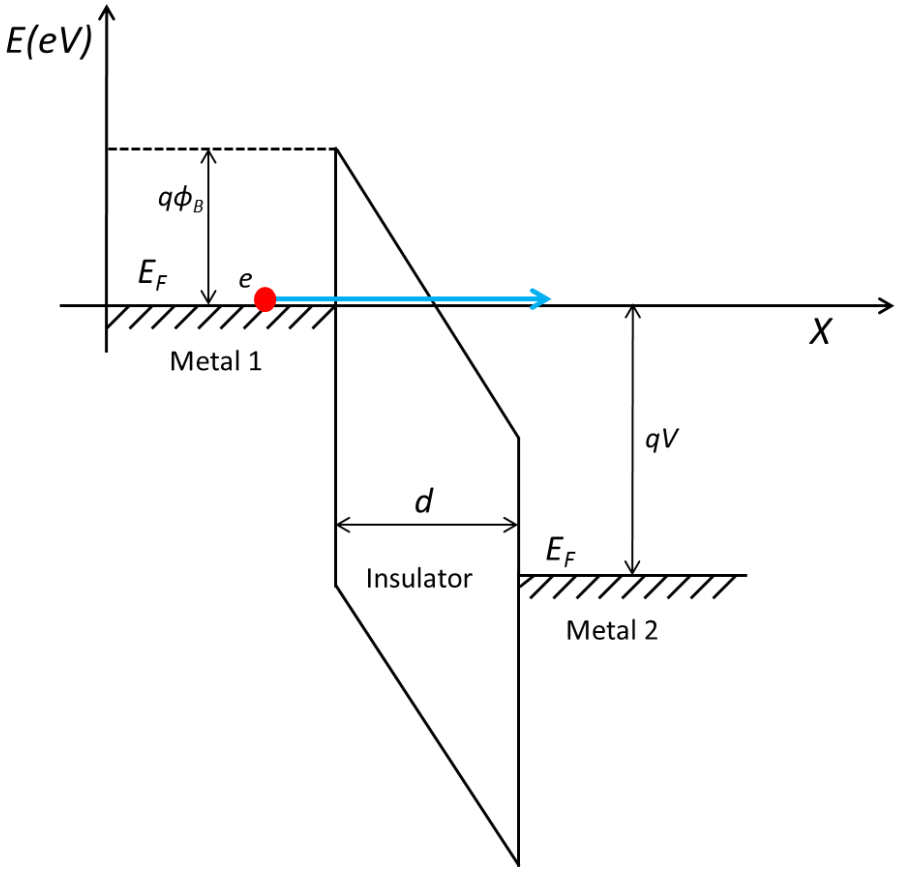

Figure 2.11 – Schematic MIM energy band diagram of Fowler-Nordheim tunnelling conduction mechanism (adapted from [35]).

The FNT current is expressed in Equation 2.21 [35];

$$J_{FNT} = \frac{q^3 V^2}{8\pi h \phi_B} \exp\left[\frac{-8\pi(2qm_T^*)^{1/2}}{3hV}\phi_B^{3/2}\right] \quad (2.21)$$

where m^* is the tunneling effective mass in the dielectric, while all other terms are as defined earlier.

FNT current can be tested for by measuring the *J-V* characteristic of the diode at low temperature (e.g. <30 K) where thermionic emission is suppressed, and plotting $\ln(J/V^2)$ as a function of 1/V [37]. FNT conduction mechanism dominates the flow of current in a MIM structure if the plot of $\ln(J/V^2)$ as a function of 1/V is linear at high applied bias [35, 37]. The test for this conduction mechanism is not applicable in this project, as our diodes have a small irreversible breakdown voltage (±0.35 V).

2.9.2 Bulk-Limited Conduction Mechanisms

Bulk-Limited Conduction Mechanisms relies only on the electrical properties of the dielectric. Mechanisms in this class are discussed below.

2.9.2.1 Poole-Frenkel Emission

Poole-Frenkel Emission (PFE) is a conduction mechanism similar to Schottky Emission, as it is also influenced by thermal excitation of electrons. But rather than electrons overcoming the energy of the barrier at the electrode-dielectric interface and moving into the conduction band of the dielectric, they do so from traps present in the dielectric [39] as shown in Figure 2.12.

Consider an electron in a trap; the potential energy of the electron can be reduced by an applied electric field across the dielectric film. The reduction in potential energy may

increase the probability of the electron being thermally excited out of the trap into the conduction band of the dielectric, thereby contributing to the rectified current [35, 39-41].

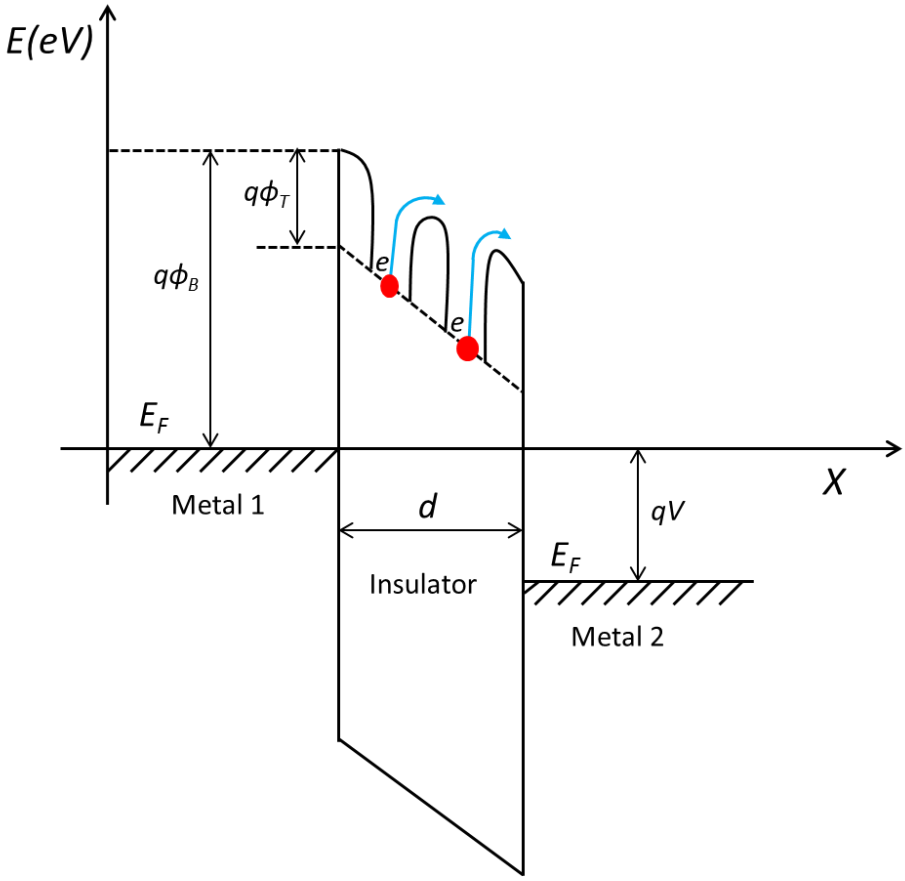

Figure 2.12 – Schematic MIM energy band diagram of Poole-Frenkel emission conduction mechanism. $q\phi_T$ represents trap energy level (adapted from [35]).

This type of conduction mechanism is more often found in defected dielectric films [39-41]. The current density due to the Poole-Frenkel emission is expressed as [35, 40-41]:

$$J_{PFE} = CE\exp\left[-\frac{q\phi_T - \sqrt{q^3E/\pi\varepsilon_i\varepsilon_0}}{k_BT}\right] \quad (2.22)$$

where C is a proportionality constant. PFE is often observed at high temperature and high applied electric field owing to the fact that the process depends on thermal activation under an electric field [35]. It can be tested for by measuring the *J-V* characteristic of the

diode at high temperature, and plotting In(*J/V*) as a function of $V^{1/2}$. The resultant plot should be linear at high applied voltage if the conduction mechanism has occurred [41].

2.9.2.2 Hopping Conduction

Hopping conduction mechanism is due to the tunnelling effect of trapped electrons in dielectric films hopping from one trap site to another [35]. Unlike in the PFE where the electrons can overcome the trap barrier through thermal activation, the electron energy is lower than the energy of the barrier between adjacent trap sites. However, the electron can still penetrate through [35]. This is similar to DT but occurs within the dielectric only. Figure 2.13 shows the schematic energy band diagram of hopping conduction.

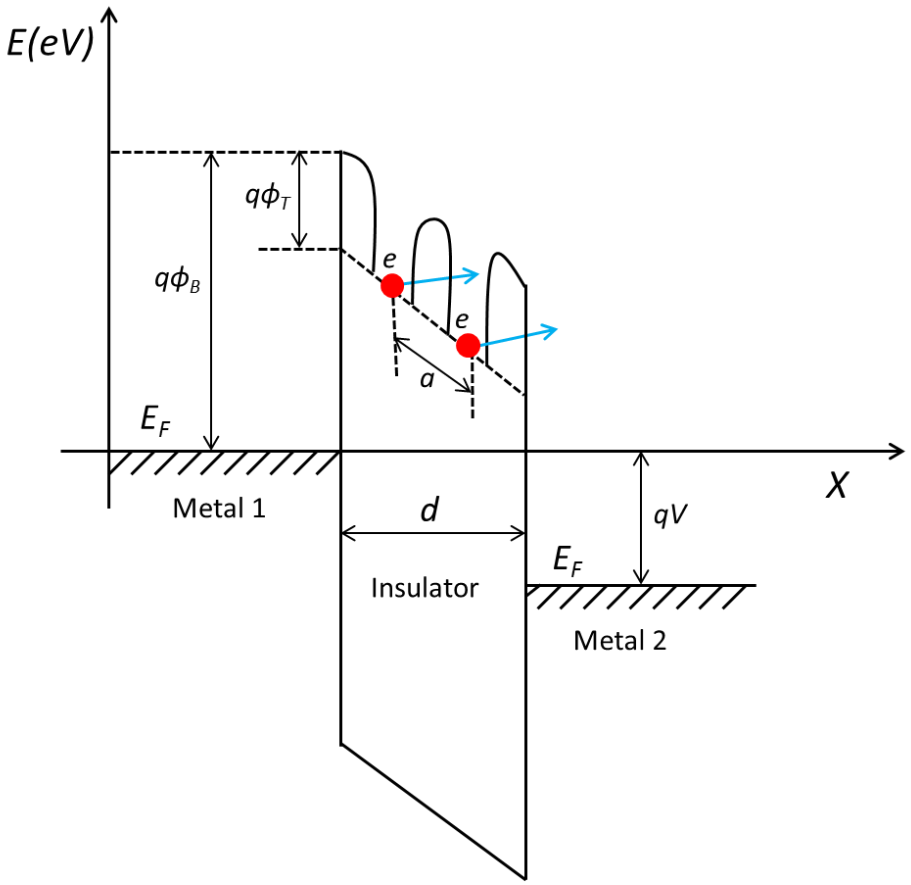

Figure 2.13 – Schematic MIM energy band diagram of hopping conduction mechanism. $q\phi_B$ is the barrier height, $q\phi_T$ is the trap energy level, and a is the mean distance between trap sites.

The hopping conduction mechanism is expressed as [35];

$$J_H = qanv.\exp\left[\frac{qaV - E_a}{k_B T}\right] \tag{2.23}$$

where a is the mean hooping distance between trap sites, *n* is the electron concentration in the conduction band of the dielectric, v is the frequency of thermal vibration of electrons at trap sites, and E_a is the activation energy [35].

2.10 Combined conduction mechanism

Although it is more desirable for only specific conduction mechanisms to occur in devices for specific applications throughout the device operation, in reality a single conduction mechanism does not fully describe the conduction mechanism taking place. Depending on the operating conditions, such as frequency, applied voltage and temperature levels, a combination of conduction mechanisms may be present with one dominating in certain instances.

2.11 Summary

The MIM diode theory has been discussed. It included the diode's operating principles and the parameters, which influence its operations such as metals and their work functions, and the insulating layer. The various types of conduction mechanisms that might occur in the diode during operation were also discussed. Among the conduction mechanisms, it was discussed that the fastest process where high speed rectification can be achieved in the MIM diode is Fowler-Nordheim Tunnelling. However, it is not feasible to carry out a test for it on our devices, as they have a small irreversible breakdown voltage compared to the applied voltage regime (tens of volts) needed for Fowler-Nordheim Tunnelling to occur. Furthermore, it was discussed that, in most cases, a combination of more than one

conduction mechanism may occur in the diode with one dominating in certain operational conditions.

References

[1] E. Sakuma, and K. M. Evenson, “Characteristics of Tungsten-Nickel Point Contact - Diodes Used as Laser Harmonic-Generator Mixers”, *IEEE J. Quant. Electron.* Vol. QE-IO, Issue 8, pp. 600-603, (1974).

[2] K. M. Evenson, J. S. Wells, L. M. Matarrese, and L. B. Elwell, “Absolute Frequency Measurements of The 28 and 78 μm cw Water Vapor Laser Lines”, *Appl. Phys. Lett.* Vol. 16, Issue 4, pp. 159-162, (1970).

[3] K. M. Evenson, D. A. Jennings, and F. R. Petersen, “Tunable Far-Infrared Spectroscopy”, *Appl. Phys. Lett.* Vol. 44, Issue 6, pp. 576-578, (1984).

[4] R. E. Nelson, “Point-Contact Diodes in terms of P-N Junction Theory”, *Electron Devices Trans.* Vol. 6, Issue 3, pp. 270 – 277, (1959).

[5] S. P. Kwok, G. I. Haddad, and G. Lobov, “Metal-Oxide-Metal (M-O-M) Detector,” *J. Appl. Phys.* Vol. 42, Issue 2, pp. 554-563, (1971).

[6] I. E. Hashem, N. H. Rafat, and E. A. Soliman, “Theoretical Study of Metal-Insulator-Metal Tunneling Diode Figures of Merit,” *IEEE J. Quantum Electron.* Vol. 49, No. 1, pp. 72-79, (2013).

[7] M. Bareiß, D. Kalblein, C. Jirauschek, A. Exner, I. Pavlichenko, B. Lotsch, U. Zschieschang, H. Klauk, G. Scarpa, B. Fabel, W. Porod, and P. Lugli, “Ultra-Thin Titanium Oxide,” Appl. Phys. Lett. Vol. 101, 083113, pp. 1-4, (2012).

[8] E. W. Cowell III, N. Alimardani, C. C. Knutson, J. F. Conley Jr., D.A. Keszler, B. J. Gibbons, and J. F. Wager, “Advancing MIM Electronics: Amorphous Metal Electrodes,” *Adv. Mater*. Vol. 23, pp. 74–78, (2011).

[9] L. E. Dodd, A. J. Gallant, and D. Wood, “Controlled Reactive Ion Etching and Plasma Regrowth of Titanium Oxides of Known Thickness for Production of Metal-Oxide-Metal Diodes”, *Micro and Nano Letters*, Vol. 8, Issue 8, pp. 476-478 (2013).

[10] S. Krishnan, H. La Rosa, E. Stefanakos, S. Bhansali, and K. Buckle, “Design and Development of Batch Fabricatable Metal–Insulator–Metal Diode and Microstrip Slot Antenna as Rectenna Elements,” *Sensors and Actuators A,* Vol. 142, pp. 40–47, (2008).

[11] M. Bareiß, A. Hochmeister, G. Jegert, U. Zschieschang, H. Klauk, R. Huber, D. Grundler, W. Porod, B. Fabel, G. Scarpa, and P. Lugli, “Printed Array of Thin-Dielectric Metal-Oxide-Metal (MOM) Tunneling Diodes,” *J. Appl. Phys.* Vol. 110, 044316, pp. 1-5, (2011).

[12] M. Bareiß, P. M. Krenz, G. P. Szakmany, B. N. Tiwari, D. Kälblein, A. O. Orlov, G. H. Bernstein, G. Scarpa, B. Fabel, U. Zschieschang, H. Klauk, W. Porod, and P. Lugli, “Rectennas Revisited”, *IEEE Trans. on Nanotechnol*. pp. 1-4, (2012).

[13] L. E. Dodd, S. A. Shenton, A. J. Gallant and D. Wood, “Improving Metal-Oxide-Metal (MOM) Diode Performance via the Optimization of the Oxide Layer”, *Journal of Electronic Materials,* Vol. 44, pp. 1361-1366, (2015).

[14] C. Fumeaux, W. Herrmann, F.K. Kneubuhl, and H. Rothuizen, “Nanometer thin-film Ni-NiO-Ni diodes for detection and mixing of 30 THz radiation,” *Infrared Phys. and Technol.* Vol. 39, no. 3, pp. 123–183, (1998).

[15] M. R. Abdel-Rahman, F. J. Gonzalez and G. D. Boreman, “Antenna-coupled metal-oxide-metal diodes for dual-band detection at 92.5 GHz and 28 THz,” *Electronics Letters,* Vol. 40, no. 2, pp. 116–118, (2004).

[16] N. Alimardania, and J. F. Conley, Jr., “Enhancing Metal-Insulator-Insulator-Metal Tunnel Diodes via Defect Enhanced Direct Tunneling,” *Appl. Phys. Lett.* Vol. 105, 082902, pp. 1-5, (2014).

[17] B. Rakos, “Investigation of Metal-Oxide-Metal Structures for Optical Sensor Applications,” *PhD thesis*, p. 27, https://curate.nd.edu/show/c247dr29087, Accessed online: 29 January 2016.

[18] H. U. Daniel, B. Maurer and M. Steiner, “A Broadband Schottky Point Contact Mixer for Visible Laser Light and Microwave Harmonics,” *Appl. Phys*. Vol. 30, pp. 189-193, (1983).

[19] L. E. Dodd, “Fabrication Optimization of Metal-Oxide-Metal Diodes”, *PhD thesis*, pp. 57, http://etheses.dur.ac.uk/9474/1/Linzi_Dodd_d51hqe_thesis.pdf?, Accessed online: 29 January 2016.

[20] B. Tiwari, J. A. Bean, G. H. Bernstein, P. Fay and W. Porod, “Thermal Infrared Detection using Dipole Antenna-Coupled Metal-Oxide-Metal Diodes*,” Journal of Vacuum Science and Technol.* Vol. 27, no. 1, pp. 11–14, (2009).

[21] B. M. Kale, “Electron Tunneling Devices in Optics,” Optical Engineering, Vol. 24, No. 2, pp. 267–274, (1985).

[22] T. W. Hickmott, “Defect Conduction Bands, Localization, and Temperature Dependent Electron Emission from Al-Al2O3-Au Diodes,” *Journal of Applied Physics,* Vol. 108, pp. 1-8, (2010).

[23] I. Hotovy, D. Donoval, J. Huran, S. Hascik, L. Spiess, M. Gubisch and S. Capone, “NiO Nanostructured Film with Pt Coating Prepared by Magnetron Sputtering,” *Czechoslovak Journal of Physics*, Vol. 56, No. 2, pp. B1192–B1198, (2006).

[24] M. B. E. Griffiths, P. J. Pallister, D. J. Mandia, and S. T. Barry, “Atomic Layer Deposition of Gold Metal”, *Chem. Mater.,* Vol. 28, pp 44−46, (2016).

[25] P. G. Gordon, A. Kurek, and S. T. Barry, “Trends in Copper Precursor Development for CVD and ALD Applications”, *ECS J. Solid State Sci. Technol.,* vol. 4, Issue 1, pp 3188-3197, (2015).

[26] A. Niskanen, T. Hatanpaä, K. Arstila, M. Leskelaä, and M. Ritala, “Radical-Enhanced Atomic Layer Deposition of Silver Thin Films Using Phosphine-Adducted Silver Carboxylates”. *Chem. Vap. Deposition,* Vol. 13, pp. 408−413, (2007).

[27] X. Wang, S. M. Tabakman, and H. Dai, “Atomic Layer Deposition of Metal Oxides on Pristine and Functionalized Graphene”, *J. AM. CHEM. SOC.* Vol. 130, pp 8152–8153, (2008).

[28] D. M. Hausmann, E. Kim, J. Becker, and R. G. Gordon, “Atomic Layer Deposition of Hafnium and Zirconium Oxides Using Metal Amide Precursors”, *Chem. Mater.* Vol 14, pp 4350-4358, (2002).

[29] K. Kukli, M. Ritala, M. Schuisky, M. Leskelä, T. Sajavaara, J.i Keinonen, T. Uustare, and A. Hårsta, “Atomic Layer Deposition of Titanium Oxide from TiI_4 and H_2O_2”, *Chem. Vap. Deposition*, Vol. 6, Issue 6, pp 303-310, (2000).

[30] Ultratech, “Savannah G2 ALD System”, http://www.annealsys.com/docs/Savannah_G2_Datasheet-22-04-14-06.pdf Accessed online: 15 January 2016.

[31] Y. Katsuta, A. E. Hill, A. M. Phahle, and J. H. Calderwood, “D.C. and A.C. Conduction in Amorphous Titanium Dioxide Thin Films,” *Thin Solid Films*, Vol. 18, No. 1, pp. 53–62, (1973).

[32] E. McCafferty and J. P. Wightman, “An X-ray Photoelectron Spectroscopy Sputter Profile Study of The Native Air-Formed Oxide Film on Titanium,” *Applied Surface Science,* Vol. 143, No. 1-4, pp. 92–100, (1998).

[33] J. J. Huang, C. W. Kuo, W. C. Chang and T. H. Hou, “Transition of Stable Rectification to Resistive-Switching in Ti/TiO2/Pt Oxide Diode,” *Applied Physics Letters*, Vol. 96, (2010).

[34] Y. Irokawa, “Hydrogen Interaction with GaN Metal-Insulator-Semiconductor Diodes,” *Physica B*, Vol. 407, No. 15, pp. 2957–2959, (2012).

[35] F. C. Chiu, “A Review on Conduction Mechanisms in Dielectric Films,” *Advances in Materials Science and Engineering,* Vol. 2014, pp. 1-18, (2014).

[36] S. M. Sze, and Kwok K. Ng, “Physics of Semiconductor Devices,” *3rd Edition, published by John Wiley & sons, Inc. Hoboken, NJ,* pp. 448-451, (2007).

[37] F. C. Chiu, “Interface Characterization and Carrier Transportation in Metal/HfO_2/ Silicon Structure,” *J. Appl. Phys.* Vol. 100, 114102, pp. 1-5, (2006).

[38] J. G. Simmons, “Conduction in Thin Dielectric Films,” *J. Phys. D: Appl. Phys.* Vol. 4, pp. 613-657, (1971).

[39] W. R. Harrella, and J. Frey, “Observation of Poole-Frenkel Effect Saturation in SiO_2 and other Insulating Films,” *Thin Solid Films*, Vol. 352, pp. 195-204, (1999).

[40] H. Schroeder, “Poole-Frenkel-Effect as Dominating Current Mechanism in Thin Oxide Films—An illusion?!,” J. Appl. Phys. Vol 117, 215103, pp. 1-13, (2015).

[41] G. F. Alapatt, W. R. Harrell, Y. Freeman, and P. Lessner, “Observation of the Poole-Frenkel Effect in Tantalum Polymer Capacitors,” *IEEE Southeast Conf.,* pp. 498-501, (2010).

Chapter 3

Applications of the MIM Diode

3.1 Introduction

In this chapter, the potential applications where the MIM diode can be used are discussed. They include electromagnetic energy harvesting, high-frequency detection, mixers and radio frequency identification (RFID) applications. Other existing electromagnetic energy harvesting technologies are also discussed in order to clearly highlight the viability of the MIM diode technology, and the new possibilities it opens in the advancement of these applications in a world where devices are being miniaturised, are needed to operate at higher frequencies and also be more efficient.

3.2 Energy recovery from waste heat

Electromagnetic energy is radiated from objects in the form of waves that can travel through free space. The waves can be characterised by either the frequency or wavelength at which they oscillate to form the electromagnetic spectrum. As can be seen in Figure 3.1, the electromagnetic spectrum consists, in order of increasing frequency and decreasing wavelength; radio waves, microwaves, infrared radiation, visible light, ultraviolet radiation, X-rays and gamma rays. Infrared radiation, which is commonly emitted by black body radiators in form of heat, is mostly wasted. Recovering such energy

and converting it into a useful form could have a positive impact on global energy problems.

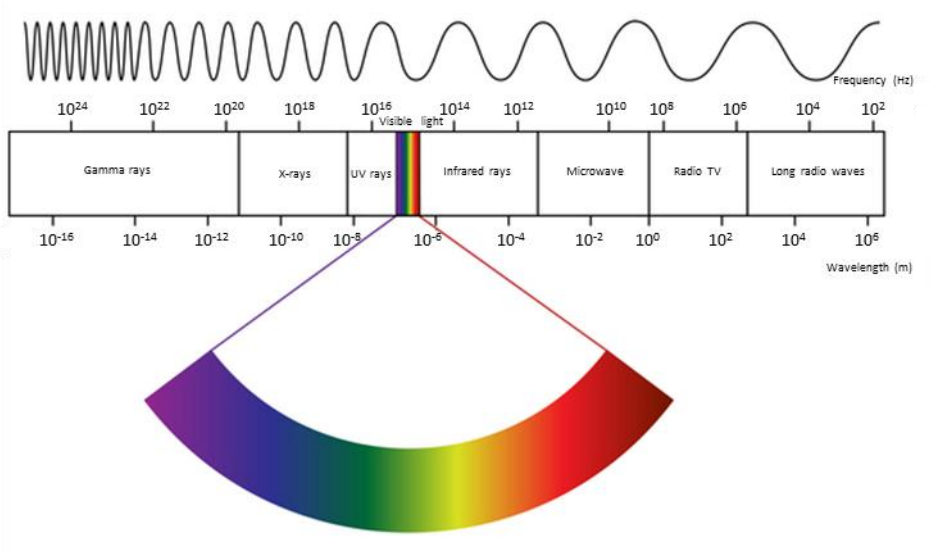

Figure 3.1 – Diagram of the electromagnetic spectrum (taken from [1]).

As can be seen in Figure 3.1, infrared radiation extends from approximately 0.5 to 500 THz. This means that any device exploiting that part of the spectrum has to be capable of operating within that frequency range. The metal-oxide-metal (MOM) diode has been reported to operate at over 200 THz [2-5], but these devices were point-contact MOM diodes which were limited by poor mechanical contact between the fine wire tip and the dielectric layer. This means that a mechanically stable MIM diode is a potentially good candidate for exploiting infrared radiation.

If we consider the automotive industry where manufacturers are becoming more concerned about extracting the maximum useable energy from fuel, then it is here that recovery systems become very important. Around 70% of the energy in petrol is converted into heat [6]. Very little of this heat is useful, particularly once the engine and cabin have warmed up, and most (around 40%) is dissipated to the atmosphere via radiators and the exhaust system [6]. A breakdown of energy consumption in a typical gasoline powered

internal combustion engine can be seen in Figure 3.2. As a typical vehicle is running at approximately 20 kW while cruising, there is the possibility for a significant amount of energy recovery. If this wasted energy could be harvested successfully, it could be used to power electrical appliances within the vehicle, such as the air conditioner, which may result in a significant improvement in the efficiency of the vehicle.

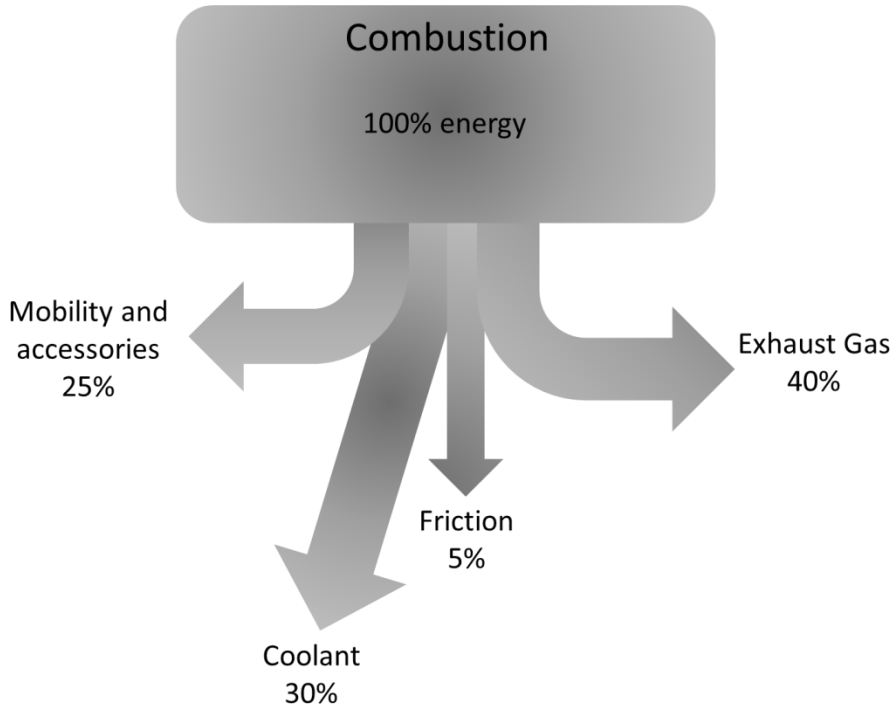

Figure 3.2 – Representation of approximate fuel energy usage (in percentage) within a typical internal combustion engine vehicle (adapted from [6])

There are existing technologies for energy saving being implemented in vehicles, such as "Brake Energy Regeneration" designed by BMW [7-8]. The battery of the vehicle only gets charged when the vehicle is braking, coasting or decelerating. The technique improves fuel efficiency by up to three percent and ensures that the full power of the engine is available for acceleration [8]. The problem with this technology is that it is only effective when the vehicle is decelerating, and only involves saving energy, not harvesting.

A typical internal combustion engine vehicle has an exhaust pipe, which can reach temperatures of up to approximately 1000 K in extreme circumstances [7, 10] and less during standard motion. The exhaust pipe channels the hot exhaust gas to the atmosphere, hence its outer surface act as an emitter of the heat, and provides an excellent opportunity for appropriate devices to harvest some of this heat energy.

Figure 3.3 – A wrapped exhaust pipe (taken from [11])

Suitable devices can for example be designed and constructed with the idea of becoming an exhaust pipe wrap as can be seen in Figure 3.3, and as long as heat is emitted at the surface of the exhaust pipe, it is being collected and converted into electrical power to be channelled back into the vehicle for use.

3.2.1 Thermoelectric generator

An existing method of heat energy recovery is the thermoelectric device which is driven by the principle known as ‘Seebeck-Effect’ where voltage is generated from a temperature gradient [6]. The structure consists of hot and cold side heat exchangers, in between which the thermoelectric module is placed. The module comprises of electron (n-type) and hole conducting (p-type) materials connected in series as shown in Figure 3.4.

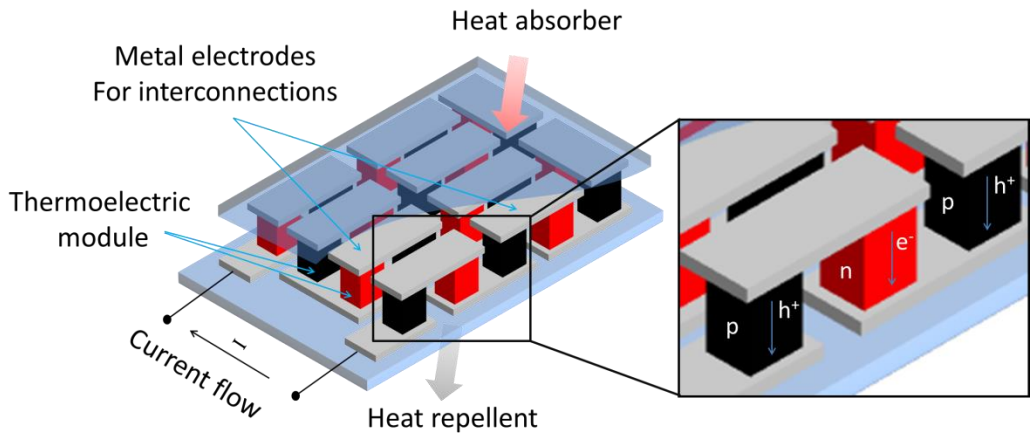

Figure 3.4 – Schematic of thermoelectric modules connected electrically in series using metal electrodes, and thermally in parallel using the heat absorber and repellent.

As heat flows from the hot side (i.e. the heat absorber) to the cold side (heat repellent), free charge carriers (electrons or holes) in the module materials diffuse to the cold side, resulting in a voltage being generated. The generated voltage is proportional to the temperature difference ($\Delta T = T_{hot} - T_{cold}$) through the Seebeck coefficient, α_b, as expressed in Equation 3.1 [6].

$$V = \alpha_b \Delta T \tag{3.1}$$

The efficiency of a typical thermoelectric device relies heavily on the difference in temperature across the device, as expressed in Equation 3.2 [6].

$$\eta_T = \frac{\Delta T}{T_{hot}} \cdot \frac{\sqrt{1+ZT}-1}{\sqrt{1+ZT}+T_{cold}/T_{hot}} \tag{3.2}$$

where

$\frac{\Delta T}{T_{hot}}$ is known as the Carnot efficiency, and ZT is the often quoted Figure of merit for the device. It describes the effectiveness of a specific thermoelectric material in terms of electrical and thermal properties, and is expressed as:

$$ZT = \frac{\alpha_b^2 T}{\rho k_{th}} \tag{3.3}$$

where

T is temperature, ρ is the electrical resistivity and k_{th} is the thermal conductivity of the material.

The advantages of the thermoelectric devices include a long life span, having been tested over time periods of 30 years. The devices have no noise, vibration or moving parts. Although these devices have been proven to work well in space [12, 13], by contrast, it is impossible to match these results on earth as there is much less of a temperature difference. In order to improve temperature difference and create a suitable atmosphere for this device to function well in vehicles, existing prototype vehicles have had to have a separate cooling system, which increases the design complexity, labour, and cost [7]. Furthermore, the world annual production of tellurium, which is the major material used in the production of the device, is too small (approximately 400 tons [14]) to be sufficient for any more than a fraction of global annual car production.

3.2.2 Thermophotovoltaic generator

The Micro-thermophotovoltaic device is also another method of heat energy recovery that has been shown to be capable of converting heat emitted by a microcombustor into usable electrical power [16-17], and has the potential to be utilised in heat energy harvesting from car exhaust pipes. The structure comprises mainly of an emitter (i.e. microcombustor), an array of photovoltaic cells, and a filter which restricts the ranges of wavelength of heat radiation which are incident on the photovoltaic cells. Figure 3.5 shows a schematic of a typical micro-thermophotovoltaic structure.

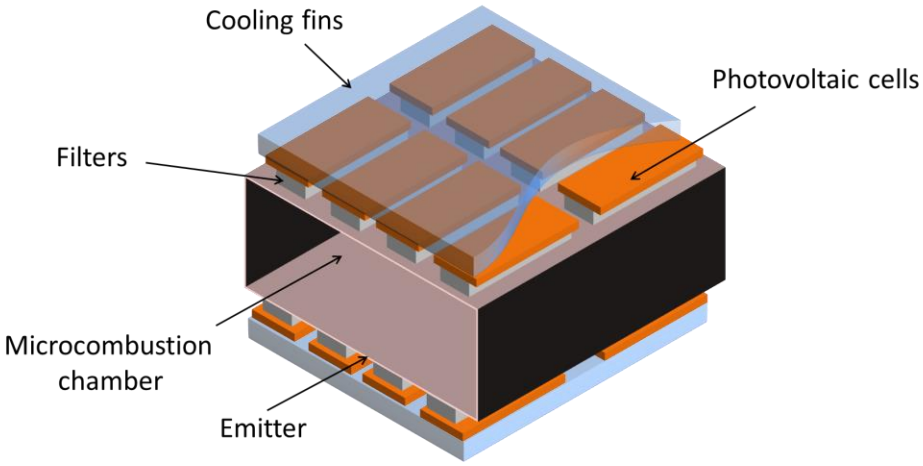

Figure 3.5 – Schematic of a micro-thermophotovoltaic structure

The initial structures produced had emitters separate from the microcombustor chamber, but, in order to simplify the assembly of the system and to maximise the use of materials, they are now designed so that the outer side of the microcombustor chamber function as the emitter as well [17], as can be seen in Figure 3.5. Consequently, the microcombustor wall must have good emissivity and must be able to withstand high temperatures (i.e. to behave as a typical blackbody emitter). Fuel is burned inside the microcombustor chamber, which results in heat being produced. This causes the outer walls of the chamber to emit heat (photons). Once the heat is incident on the surface of the photovoltaic cells, free electrons are created, resulting in electric power being generated. It is worthy of note that if the heat radiated has a bandwidth greater than the band gap of the photovoltaic cell, the cell heats up and could ultimately be damaged. Therefore, a filter is used to select an appropriate energy band. In [17], a silicon carbide (SiC), which is a good blackbody emitter, was used as the emitter, and the photovoltaic cells used were made using GaSb. Various mixtures have been used as fuel in the structure, resulting in different energy densities as can be seen in Figure 3.6. Hydrogen-air fuel is the most commonly used to promote the idea of high energy density, i.e. a lot of energy in a small mass, as shown in Figure 3.6, and it works well with the system.

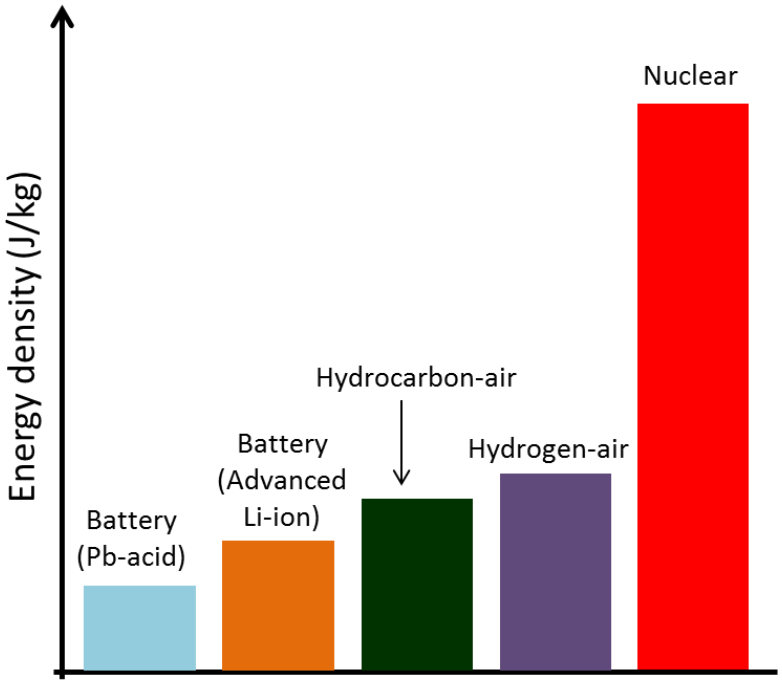

Figure 3.6 – Energy density of different energy systems (adapted from [18])

The micro-thermophotovoltaic devices present numerous advantages, including having no moving parts, which eliminates any possibility of the device failing due to mechanical wear. The production of the device is also cost effective compared to the thermoelectric devices. Furthermore, efficiency of up to 27.3% involving this device, when converting energy from a hydrogen-air source has been reported [19].

The main issue with the micro-thermophotovoltaic structure is heat dissipation. The design has to have large cooling fins (as can be seen in Figure 3.5) to prevent high temperatures from damaging the photovoltaics [17]. This makes it less flexible, bulky and limits its potential applications.

3.2.3 Thermal rectenna

A good alternative technology to consider is the thermal rectenna. The device consists of an antenna coupled to a rectifier, which is used to convert electromagnetic radiation into electrical current. Fast rectifiers, such as the Schottky diode, the metal-insulator-metal

(MIM) diode, and more recently the self-switching nanodiode, are often used in this application [20-22] due to their ability to operate at frequencies well into the terahertz range. The electromagnetic radiation incident on the antenna results in an alternating signal, which is then half-rectified by the diode, and can be used to power a load [21]. One of the major drawbacks, however, is the relatively low conversion efficiency (as expressed in Equation 3.4), caused by the mismatch between the impedance of the antenna (tens to hundreds of Ω) and that of the diode, which is typically as high as several kilo ohms [20-22]. Figure 3.7 shows a basic equivalent circuit diagram of a rectenna with an impedance matching network.

$$\eta_C = \frac{P_{OUT}}{P_{IN}} \tag{3.4}$$

where P_{IN} is the input power transmitted by the antenna, and P_{OUT} is the rectified output power.

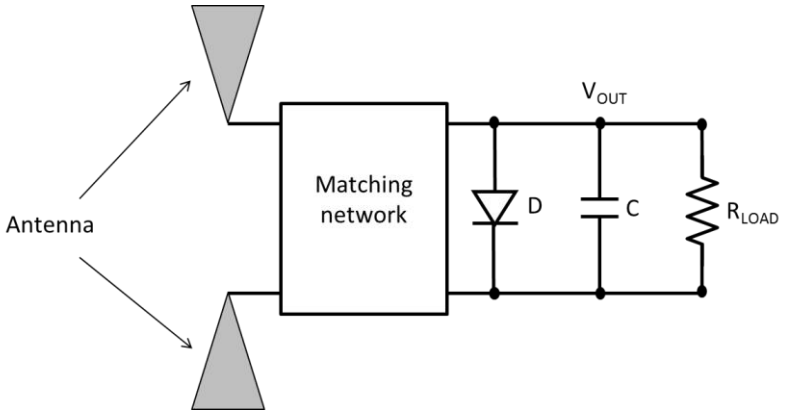

Figure 3.7 – Basic equivalent circuit diagram of a rectenna with impedance matching network.

The matching circuit (placed between the antenna and the diode) is required in order to match the impedances of the antenna and the diode, which will then result in an improved conversion efficiency. Work has been done on the design of the impedance matching network, and this will be discussed in the appropriate section.

The MIM diode theory has already been discussed in Chapter 2, and therefore only the antenna will be discussed here.

3.2.3.1 Antenna

An antenna is used to either transmit or receive electromagnetic waves, and it serves as a transducer that converts guided waves into free-space waves in the transmitting mode, or vice-versa in the receiving mode [23]. The most basic properties of an antenna include its input impedance, radiation pattern, directivity and gain.

The input impedance of an antenna is the impedance presented by an antenna at its terminals, expressed as [23]:

$$Z_A = R_A + jX_A\ \Omega \tag{3.5}$$

where R_A is the antenna resistance, and X_A is the antenna reactance.

The impedance is a function of the geometry of the antenna, the method of excitation, and the frequency [23].

The radiation pattern is defined in [23] as the spatial distribution of a quantity that characterises the electromagnetic field generated by an antenna. The field intensity of the propagating wave decreases by 1/*R* with distance *R* from the source. The radiation pattern of an antenna is commonly described in terms of its principal E-plane and H-plane patterns. For a linearly polarized antenna, the E-plane pattern is defined as the plane containing the electric field vector and the direction of maximum radiation, and the H-plane pattern is the plane containing the magnetic field vector and the direction of the maximum radiation.

The directivity is the ratio of the radiation intensity (i.e. the power radiated per unit solid angle) in a given direction to the average radiation intensity as expressed in Equation 3.6 [23].

$$D = 4\pi \frac{U(\theta,\phi)}{P_{rad}} \tag{3.6}$$

where $U(\theta,\phi)$ is the radiation intensity, and P_{rad} is the average intensity (or radiated power). The directivity is an indication of the directional properties of the antenna, and is usually expressed in decibels [23].

The gain of an antenna is defined as the ratio of the radiation intensity in a given direction to the radiation intensity that would be obtained if the power accepted by the antenna were radiated isotropically. The gain can be expressed as [23]:

$$G = 4\pi \frac{U(\theta,\phi)}{P_o} \tag{3.6}$$

where P_o is the power input to the antenna. The gain is a dimensionless quantity, expressed in decibels. While the directivity is based on radiated power, the gain is based on input power. The gain is related to the directivity through [23]:

$$G = \eta_o D \tag{3.7}$$

where η_o is the antenna efficiency and takes into account losses due to mismatch at the antenna terminals and dielectric and conduction losses. For a perfectly matched lossless antenna, its gain and directivity are equal [23].

There are varieties of antennas, including the dipole antenna, horn antenna, spiral antenna etc. An antenna could be a short or broadband depending on its type and design. Dipole antennas are the most common choice for rectenna devices due to their simplicity and

ease of fabrication. However, broadband antennas such as the self-complementary antennas are more desirable, as this will broaden the operation of the device across a wide range of application related to electromagnetics.

3.2.3.2 Self-complementary antenna

A self-complementary antenna is a broadband antenna, consisting of a conducting-sheet element identical in shapes and angles to any open space around it, so that no difference is noticeable except for a rotation of angles if the conducting-sheet elements and the open spaces are interchanged [24]. For a two-terminal antenna with this type of structure, in an ideal case, the input impedance will be real and constant i.e. independent of the frequency [24-25]. The impedance is typically $Z \equiv 60\pi \equiv 188\ \Omega$ in free space [25]. This value may vary if the antenna is fabricated on a substrate, depending on the dielectric constant of the substrate, but remains constant. Combining the constant impedance and the broadband characteristics of the self-complementary antenna makes it an excellent choice for the rectenna application.

The bow-tie antenna shown in Figure 3.8 is an example of a self-complementary antenna. It is geometrically simple to fabricate, and presents a broadband characteristics.

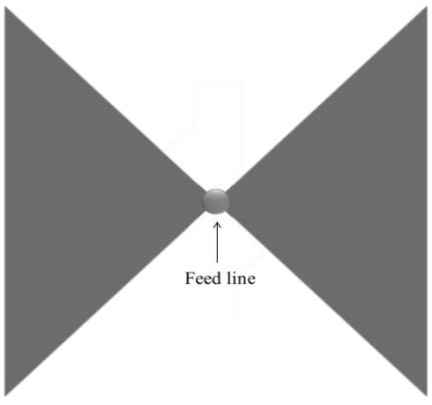

Figure 3.8 – Bow-tie self-complementary antenna (adapted from [24]).

3.2.3.3 Log-periodic antenna

The log-periodic antenna is also a self-complimentary, broadband antenna, with its design involving a geometric pattern that is repeated, but with a changing size [24]. This results in a repetitive behaviour in the electrical characteristics of the antenna. The pattern size changes with each repetition by a constant scale factor so that the structure grows from the feed point toward the other end [24]. Figure 3.9 shows a basic log-periodic antenna.

Figure 3.9 – A typical log-periodic antenna (adapted from [24]).

Unlike the conventional dipole antenna whose bandwidth is defined and so limited by its length, the bandwidth of a log-periodic antenna, like that of the self-complementary antenna, is defined by an angle, so that it is frequency independent (because angles are independent of wavelength for any frequency). Though these types of antennas are frequency independent in theory, this is not however completely true in practice. The actual bandwidth that may be achieved is dependent on how large the structure is (to determine the lower frequency limit) and how small it is (which determines the upper frequency limit). The bow-tie and log-periodic antenna have similar properties. However, the bow-tie antenna was a preferred choice in this project because it is easier to fabricate.

3.2.4 Advantages of MIM diode in a rectenna device

Consider a rectenna being used to harvest heat energy from car exhausts; a diode able to operate at the infrared frequencies is required. Antennas are easier to design; in contrast, fabricating a MIM diode with the dimension required to operate as such high frequencies is extremely difficult. The MIM diode has been reported to operate at a frequency of over 120 THz [4], but this was a point-contact junction, which was mechanically unstable. Therefore, if a mechanically stable and fast enough MIM diode can be successfully produced, it can be a very useful component in this application. Furthermore, in [27], the MIM diode was used in a dual-band sensing application where millimetre-wave and infrared antennas were both coupled to a Ni-NiO-Ni MOM diode. The device as demonstrated in [26], detects millimetre-wave at 94 GHz and infrared signals at 28 THz. This clearly indicates that the MIM diode, coupled with a broadband antenna, can recover energy across a wide range of the length of the car exhaust pipe, considering the fact that the temperature profile (and so the emitted energy density) is never the same across the whole length of the exhaust. As should be expected, the exhaust pipe temperature is higher around the car engine, and decreases further down away from the engine as shown in Figure 3.10, where the temperature profile of a Jaguar exhaust pipe, superimposed on a photograph of the underside of the car, can be seen [7].

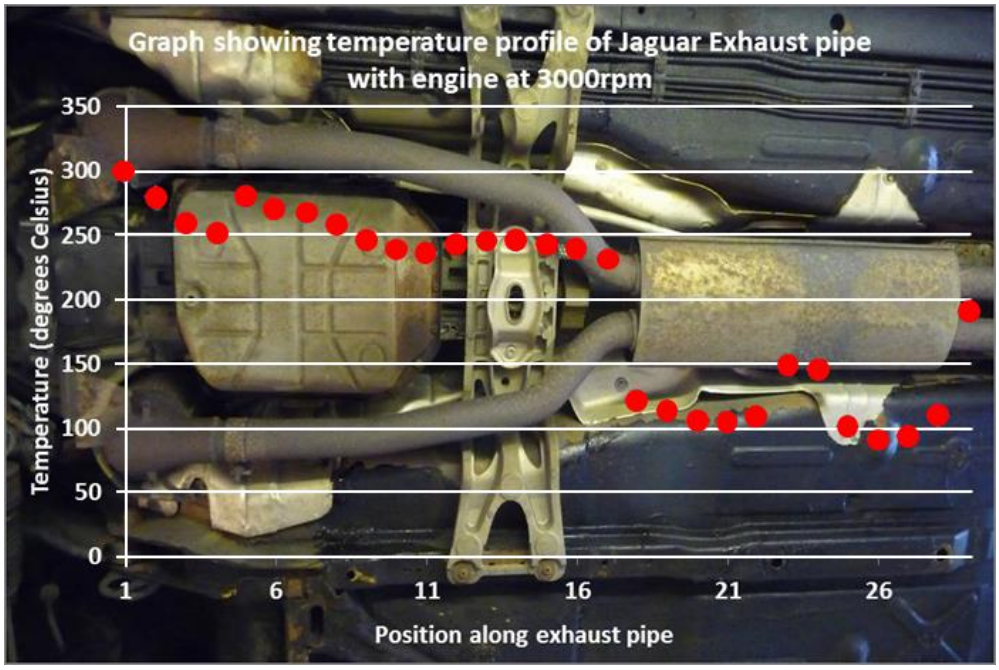

Figure 3.10 – The exhaust pipe and temperature profile of a Jaguar at 3000 rpm (taken from [7])

Other advantages of the MIM diode in a rectenna device include the possibly of fabrication on a flexible substrate, thereby easily allowing the rectenna to be produced in the form of an exhaust wrap, which needs to be flexible, as described in Figure 3.2.

3.2.5 Advantages and disadvantages of a rectenna device

Individual rectenna devices operating at the desired frequencies will be extremely small, meaning each will have a very small (nanometer scale) surface area. This means that it is possible to mount a large array of these devices across the surface area of the exhaust pipe, which will then result in more power being produced. Furthermore, a rectenna device can be fabricated on a flexible substrate, thereby increasing the possibility of millions of the devices being produced in the form of an exhaust wrap.

The problem, however, is that the feature dimension needed for the MIM diodes to be able to operate in the desired frequency range is in the sub-100 nm region, which is impossible to achieve using the photolithographic technique. Furthermore, the diodes are likely to be

damaged by excess heat, considering the fact that they may be exposed to high temperatures emitted by the exhaust pipe. This needs to be considered in the design.

3.3 High-frequency signal detection

Signal detection involves the extraction of specific signal(s) from all of the electromagnetic waves present in an environment with or without synchronisation with the sender of the waves. Devices used in detecting such signals are known as “detectors”, and are characterised by the frequency at which they can operate. A typical detector can also be referred to as a rectenna, with the same operating principle as discussed in Section 3.2.1.3, where an optical input signal is converted to an electrical output power.

Schottky barrier diodes have been used as direct detectors throughout the millimetre-wave, and into the submillimetre-wave bands [27-28]. But with the MIM diode, infrared signals can be detected, as in [29]. In [29], the rectenna was used to detect Infrared signals of up to 28 THz.

In most of the experiments carried out by others where the MIM diode has been used as a component in a detection device, as in [3-5, 29], the diode was biased. However, if the MIM diode zero bias curvature coefficient is maximised using the technique discussed in Section 2.3, the detector can operate without the need for an external bias, as the diode is able to rectify current at zero bias voltage.

3.4 Frequency mixer

A frequency mixer is an electrical circuit with a nonlinear characteristic that can create new signals with new frequencies from two different signals applied to it [30-31]. In its most common application, two signals at frequencies f_1 and f_2 are applied to a mixer, which

produces new signals as the sum $f_1 + f_2$ and difference $f_1 - f_2$ of the original frequencies, as can be seen in Figure 3.11.

Mixers are widely used to shift signals from one frequency range to another, a process known as heterodyning, for convenience in transmission or further signal processing.

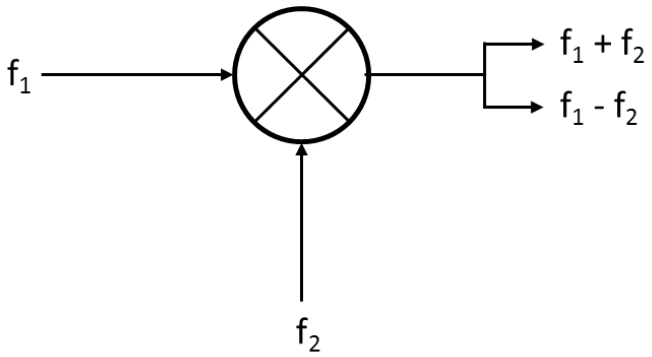

Figure 3.11 – Schematic of a basic frequency mixer.

Nonlinear electronic components that are commonly used in this application include diodes (in which case are known as passive mixers) and transistors (here known as active mixers). The application exploits the non-linear relationship between voltage and current of these components to provide the multiplying element responsible for the new regimes of signals. Focusing on the diode, the diode does not reproduce the frequencies of its driving voltage in the current through it; this therefore allows the desired frequency manipulation as in [30-31].

Since the MIM diode is capable of operating at frequencies of over 120 THz [4-5], frequency mixing at the terahertz range is then possible. The potential of this promise has already been reported in [32].

3.5 Radio Frequency Identification (RFID)

Radio Frequency Identification (RFID) refers to a wireless system of transferring data using radio signals. It comprises of two components: tag and reader. The reader is a device that has one or more antennas that emit radio waves and receive signals back from the RFID tag. The tags, which use radio waves to communicate information to a reader, can be passive or active. Passive RFID tags are powered by the incident RF power generated by an RFID reader while active RFID tags are powered by an on-board power source, usually batteries. However, they are bulky, have a short lifespan and are more expensive. While the passive tags are lighter, have unlimited life span, and are cheaper than their active counterpart, they have a shorter read range and require a high powered reader to supply the energy needed to operate them [33, 34-36]. The passive tag is however the widely used tag due to the advantages (smaller mass, unlimited life span and cheaper) it possesses over the active one, with manufacturers developing more efficient readers [35], and ultra-low power consuming passive tags [33]. The performance of an RFID system is greatly related to the frequency range in which it is used. The higher the operating frequency, the faster the data transfer rate and the longer the read range [36]. However, the frequency range at which the system can operate is limited by the switching speed of the rectifier used. Up to 2.5 GHz operating frequency has been achieved using Schottky diodes as rectifiers [36]. With the MIM diode, an operating frequency of several THz is possible, which will in turn maximise both data transfer and read range.

3.6 Summary

Existing electromagnetic energy harvesting technologies in the automotive industry and elsewhere have been discussed. They include thermoelectric devices which generate a voltage from a temperature gradient, and micro-thermophotovoltaic devices which convert

heat emitted by a microcombustor into useable electrical power. However, these technologies have their disadvantages. Rectenna devices look like a promising alternative if a MIM diode (which is the most delicate component the devices consist of) capable of operating at the required frequency regime (mid to far infrared) with good mechanical stability is successfully produced. The MIM diode has also been discussed as a very useful component in advance applications such as high-frequency detection, mixers, and radio frequency identification (RFID), due to its ultra-high speed switching capability.

References

[1] Livescience “the Electromagnetic spectrum” http://www.livescience.com/38169-electromagnetism.html, Accessed online: 22 January 2016.

[2] E. Sakuma, and K. M. Evenson, “Characteristics of Tungsten-Nickel Point Contact - Diodes Used as Laser Harmonic-Generator Mixers”, *IEEE J. Quant. Electron.* Vol. QE-IO, Issue 8, pp. 600-603, (1974).

[3] K. M. Evenson, J. S. Wells, L. M. Matarrese, and L. B. Elwell, “Absolute Frequency Measurements of The 28 - and 78 - µm cw Water Vapor Laser Lines”, *Appl. Phys. Lett.* Vol. 16, Issue 4, pp. 159-162, (1970).

[4] V. I. Denisov, V. F. Zakhar’yash, V. M. Klement’ev and S. V. Chepurov, “Very-High-Speed Metal-Oxide-Metal Diodes on W-Ni, Ptti, and Pt-W Contacts,” *Instruments and Experimental Techniques*, vol. 50, Issue. 4, pp. 517–523, (2007).

[5] K. M. Evenson, D. A. Jennings, and F. R. Petersen, “Tunable Far-Infrared Spectroscopy”, *Appl. Phys. Lett.* Vol. 44, Issue 6, pp. 576-578, (1984).

[6] P. Ramade, P. Patil, M. Shelar, S. Chaudhary, S. Yadav, and S. Trimbake, “Automobile Exhaust Thermo-Electric Generator Design & Performance Analysis”, *Int. J. Emerging Technol. Adv. Eng.* Vol. 4, Issue 5, pp. 682-691, (2014).

[7] L. E. Dodd, “Fabrication Optimization of Metal-Oxide-Metal Diodes”, *PhD thesis*, pp 127-132, http://etheses.dur.ac.uk/9474/1/Linzi_Dodd_d51hqe_thesis.pdf?, Accessed online: 29 January 2016.

[8] BMW, “BMW Technology Guide: Brake Energy Regeneration,” http://www.bmw.com/com/en/insights/technology/technology_guide/articles/mm_brake_energy_regeneration.html, Accessed online: 22 January 2016.

[9] F. Stabler, “Automotive Thermoelectric Generator Design Issues”, in DOE Thermoelectric applications workshop. San Diego, California, USA, (2009).

[10] F. Stabler, “Automotive Thermoelectric Generators: Design and Manufacturing,” in Symposium N: Material and Devices for Thermal-to-Electric Energy Conversion, Proc. MRS Spring Meeting. San Francisco, California, USA, 13 April 2009, p. 9.

[11] AliExpress “Insulation Pipe Wrap” http://www.aliexpress.com/price/insulation-pipe-wrap_price.html, Accessed online: 22 January 2016.

[12] L. A. Fisk, “Journey into the Unknown Beyond”, *Science,* Vol. 309, pp. 2016-2017, (2005).

[13] Multi-Mission Radioisotope Thermoelectric Generator (MMRTG), *NASA facts,* (2013).

[14] U.S Geological Survey, Mineral Commodity Summary 2016, p. 168-169. http://minerals.usgs.gov/minerals/pubs/mcs/2016/mcs2016.pdf, Accessed online: 01 November, 2016.

[15] F. Stabler, “Benefits of Thermoelectric Technology for the Automobile,” in DOE Thermoelectric applications workshop. San Diego, California, USA, (2011).

[16] W. M. Yang, S. K. Chou, and J. Li, “Microthermophotovoltaic Power Generator with High Power Density”, *Appl. Therm. Eng.* Vol. 29, pp. 3144–3148, (2009).

[17] J. Li, S. K. Choua, Z. W. Lib, and W. M. Yanga, “A Potential Heat Source for the Micro-Thermophotovoltaic (TPV) System”, Chem. Eng. Sci. Vol. 64, pp. 3282-3289, (2009).

[18] S. K. Chou, W. M. Yang, K. J. Chua, J. Li, and K. L. Zhang, “Development of Micro Power Generators – A Review”, *Appl. Energy*, Vol. 88 pp. 1–16, (2011).

[19] W. M. Yang, D. Y. Jiang, S. K. Chou, K. J. Chua, K. Karthikeyan and H. An, "Experimental Study on Micro Modular Combustor for Microthermophotovoltaic System Application," *Int. J. Hydrogen Energy*, Vol. 37, no. 12, pp. 9576-9583, (2012).

[20] S. Harrer, S. Strobel, G. Scarpa, G. Abstreiter, M. Tornow, and P. Lugli, "Room Temperature Nanoimprint Lithography Using Molds Fabricated by Molecular Beam Epitaxy", *IEEE Trans. Nanotechnol*. Vol. 7, Issue 3, pp. 363-365, (2008).

[21] R. M. Osgood, B. R. Kimball, J. Carlson, "Nanoantenna-Coupled MIM Nanodiodes for Efficient vis/nir Energy Conversion", *SPIE Proceedings* Vol. 6652, (2007).

[22] M. Bareiß, B. N. Tiwari, A. Hochmeister, G. Jegert, U Zschieschang, H. Klauk, B. Fabel, G. Scarpa, G. Koblmüller, G. H. Bernstein, W. Porod, and P. Lugli, "Nano Antenna Array for Terahertz Detection", *IEEE Trans. Microwave Theory Tech*. Vol. 59, Issue 10, pp. 2751-2754, (2011).

[23] C. G. Christodoulou, and P. F. Wahid, "Fundamentals of Antennas: Concepts and Applications," published by the SPIE press, Bellingham, Washington, pp. 13-20, (2001).

[24] C. A. Balanis "Antenna Theory, Analysis and Design", 3Rd Edition, published by John Wiley & Sons, Inc., Hoboken, New Jersey, pp. 4-7, (2005).

[25] Y. Mushiake, "Self-Complementary Antennas," *IEEE Antennas Propag. Mag.* Vol. 34, No. 6, pp. 23-29, (1992).

[26] M. Abdel-Rahman, F. J. Gonzalez, G. Zummo, C. Middleton and G. D. Boreman, "Antenna-Coupled MOM Diodes for Dual-Band Detection in MMW and LWIR", *Proc. SPIE - The Int. Society For Opt. Eng·* pp. 238-243, (2004).

[27] J. L. Hesler and T. W. Crowe, “Responsivity and Noise Measurements of Zero-Bias Schottky Diode Detectors”, *18th Int. Symp. on Space Terahertz Technol.* pp. 89-92, (2007).

[28] J. L. Hesler and T. W. Crowe, “NEP and Responsivity of THz Zero-Bias Schottky Diode Detectors”, *32nd Int. Conf. on Infrared and Millimeter Waves (IRMMW)*, pp. 844 – 845, (2007).

[29] M. R. Abdel-Rahman, B. Monacelli, A. R. Weeks, G. Zummo, and G. D. Boreman, “Design, Fabrication, and Characterization of Antenna-Coupled Metal-Oxide-Metal Diodes for Dual-Band Detection”, *Opt. Eng.* Vol. 44(6), pp. 066401, (2005).

[30] H. Odashima, K. Yamamoto, F. Matsushima, S. Tsunekawa, and K. Takagi, “Characteristics of Metal-Insulator-Metal Diodes as Generators of Far-Infrared Radiaton”, *IEEE J. Quantum Electron*. Vol 32, Issue 2, pp. 350-356, (1996).

[31] R. E. Drullinger, K. M. Evenson, D. A. Jennings, F. R. Petersen, J. C. Bergquist, Lee Burkins, and H. U. Daniel, “2.5 – THz Frequency Difference Measurements in the Visible Using Metal-Insulator-Metal Diodes”, *Appl. Phys. Lett.* Vol. 42, Issue 2, pp. 137-138, (1983).

[32] M. P. Sassi, A. Godone, and F. Bertinetto, “Mixing Properties of MIM Diodes in the Infrared”, *Int. J. Infrared and Millimeter Waves,* Vol. 8, Issue. 3, pp. 291-297, (1987).

[33] S. Jinpeng, W. Xin’an, L. Shan, Z. Hongqiang, H. Jinfeng, Y. Xin, F. Xiaoxing, and G. Binjie, “Design and Implementation of an Ultra-Low Power Passive UHF RFID Tag”, *J. Semicond*. Vol. 33, Issue 11, pp. 115011, (2012).

[34] N. Tran, B. Lee, and J. W. Lee, “Development of Long-Range UHF-band RFID Tag chip Using Schottky Diodes in Standard CMOS Technology”, *IEEE Radio Freq. Integr. Circuits Symp.* Pp 281-284, (2007).

[35] R. E. Barnett, J. Liu, and S. Lazar, “A RF to DC Voltage Conversion Model for Multi-Stage Rectifiers in UHF RFID Transponders”, *IEEE J. Solid-State Circuits,* Vol. 44, Issue 2, pp. 345-370, (2009).

[36] R. R. Buted, “Zero Bias Detector Diodes for the RF/ID Market”, *Hewlett-Packard Journal,* pp. 94-98, (1995).

Chapter 4

Fabrication and Analysis Techniques

4.1 Introduction

In this chapter, the techniques employed in fabricating and characterising the MIM diodes, both electrically and physically, are discussed in detail, which will be referred to in subsequent chapters. The diode fabrication involved depositing a patterned base layer of metal on a 2 inch borosilicate glass wafer, followed by an insulating layer, which was either deposited or grown on top of the surface of the base metal depending on the material or deposition technique used, followed by a patterned metal layer being deposited on top of the insulating layer to complete the structure. Specific information regarding the fabrication process route relating to the different insulating materials used is discussed in the appropriate chapters; however, a general discussion of the main techniques and equipment used in the various processes are described here in this chapter. The electrical analysis includes the diodes' *J-V* characteristics where associated common figures of merits are discussed.

4.2 Photolithography

The main photolithographic technique used in this work is a bi-layer resist lift-off process which involves spin coating polymethylglutarimide (PMGI SF9) and Microposit (SPR 350 1.2) on a 2 inch borosilicate glass substrate, followed by patterning and metal deposition. Once metals have been deposited, the photoresists were removed in Microposit Remover 1165. 1165 remover dissolves both the SPR 350 and the PMGI layers, causing the metal to "lift-off" from the substrate, leaving metal only in the areas that were patterned (i.e. the areas not covered by photoresists).

The bi-layer resist technique was used with the aim of creating an undercut, which forms a T-step profile after development has occurred, as shown in Figure 4.1(a). The T-step profile is required to prevent the deposited metal from having rough edges after lift-off has taken place. A rough edge can cause problems later on when depositing other layers of dielectric and metal during the fabrication process. Issues such as a discontinuous (open circuited) top metal layer can occur, making it difficult to perform electrical measurement on the diode. The T-step profile prevents the deposited metals from having a contact with the photoresists at the patterned-photoresist interface (Figure 4.1(b)). In which case, when the photoresist stack and unwanted metal is stripped off, the remaining metal left on the substrate has a clean profile devoid of rough edges (Figure 4.1(c)).

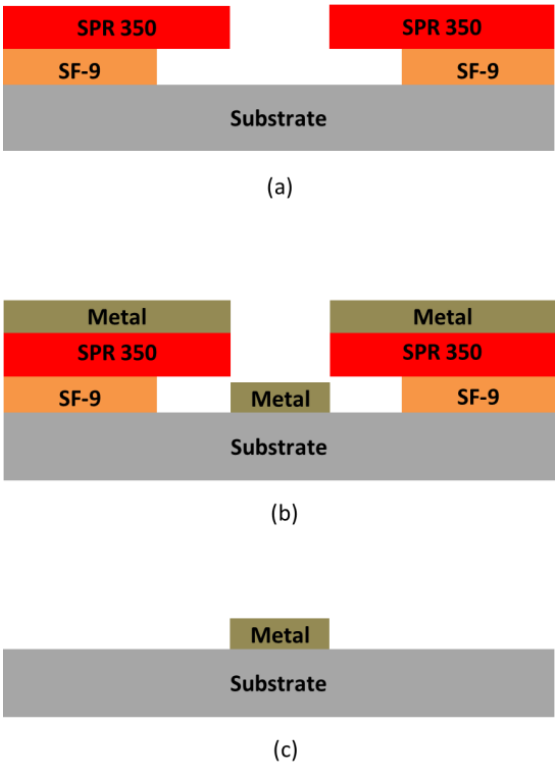

Figure 4.1 – Photoresist T-step profile allowing a discontinuous film to be deposited (a), such that when the photoresist and hence unwanted metal is removed (b), the remaining metal left has a neat profile (c).

Two factors are particularly important in controlling the size of the undercut (i.e. T-profile) created: the exposure time and the development time. For the same development time, the PGMI SF9 will dissolve more rapidly than the Microposit SPR 350, which results in the undercut being created. Therefore, care is required, as over development may result in the collapse of the top photoresist layer. This will then mean that the bi-layer resist technique is not achieved.

The two photoresists (i.e. PMGI SF9 and Microposit SPR 350) used were coated on the substrate surface through spinning, using Laurell spinners. Spin coating ensures control over the resists' thickness, and repeatability. Desired thicknesses as a function of spin speed were obtained from supplied thickness vs spin speed graphs [1-2]. A thickness of 0.5 µm was achieved for PMGI SF9 when spun at 6000 rpm [1], and 1.2 µm for SPR 350 1.2

when spun at 3700 rpm [2]. After each spinning run the photoresists where cured by placing the substrates on a hotplate.

Substrates were patterned using dark field masks. Because the Microposit SPR 350 is a positive resist, any regions which were transparent on the mask would be removed after exposure to UV light and development, meaning the transparent regions relate to where metal would be deposited. An EVG 620 mask aligner was used to expose the substrates to UV light, changing the chemical property of the photoresist in the regions that have been exposed, such that the resist is removed in the subsequent development process carried out using MF-319 developer. A summary of the bi-layer lift-off process can be seen in Table 4.1 (as noted earlier).

Table 4.1 – The process parameters used for creating the bi-layer lift-off.

Process	**Condition**	**Time**
Wafer dehydration bake	200 ^{o}C	3 mins
Spin PMGI SF9	500 rpm	10 sec
Spin PMGI SF9	6000 rpm	50 sec
Bake	200 ^{o}C	5 mins
Spin Microposit SPR 350	700 rpm	10 sec
Spin Microposit SPR 350	3700 rpm	40 sec
Bake	110 ^{o}C	3 mins
Expose		4 sec
Develop		2 mins

4.3 Metal deposition

Once the patterning was complete, metal was deposited on the substrates using the electron beam evaporator. E-beam deposition occurs in a vacuum chamber and involves a process in which an accelerated beam of electrons is magnetically deflected within a vacuum to collide with and heat a small volume of metal contained within a crucible. The metal subsequently sublimes/evaporates and recondenses on a substrate mounted above the crucible within the chamber. Because the E-beam deposition occurs in a vacuum, the metal atoms are unlikely to collide with any gas particles before reaching the substrate, leading to a very pure metal being deposited on the surface of the substrate with good directionality.

The E-beam deposition technique is very directional; therefore, the substrates are placed perpendicularly to the crucibles so that as the metal evaporates and deposits on the substrate, a discontinuous film at the photoresist-clear region interface is achieved. In which case, the desired metal left in the patterned area on the substrate after lift-off has taken place has a clean profile as discussed in Section 4.2 above.

4.4 Insulating film deposition

4.4.1 Thermally grown oxide

The initial insulating film produced on top of a base metal (titanium) was TiO_x. The oxide was grown on the metal thermally using a furnace as in [3], by placing the sample in a temperature controlled humid environment at 100 ^{o}C for different times resulting in different oxide thicknesses. For instance, oxide grown on samples placed in the furnace for 2 hours was, on average, 6 nm thick; whereas samples placed for 4 hours have an oxide which is thicker at 7.6 nm on average [3]. It is worth noting that by using this oxide formation technique, the base metal that may be utilised needs to have the ability to

oxidise readily. Here, titanium was used due to its ability to do just this, among other reasons which are discussed in more detail in appropriate chapters. The problem with this technique was that the oxide formed was too rough, too thick and not uniform, which results in a significant variation in electrical results between diodes [4].

4.4.2 Oxide formed using PE/RIE

Another technique employed in forming the TiO_x was the use of an Oxford Instruments combined plasma etch/reactive ion etch (PE/RIE) system, which provides a more controllable process by changing modes without removing samples in the transition as in [5]. The RIE mode was used to etch any native oxide that may have formed on the titanium prior to placing the sample in the equipment chamber. A plasma oxidation then took place in PE mode, which resulted in an oxide forming in a controlled manner on the surface of the exposed titanium [5]. Tables 4.2 and 4.3 show the RIE/PE parameters used in etching away any native oxide on the base metal, and forming an oxide with a thickness of 4.1 nm on average [5]. Variation in the oxide thickness that can be formed using this process is determined by the plasma power rather than the time [5-6].

Table 4.2 – The process parameters in RIE mode used for etching away any native oxide

Parameter	Value
Oxygen pressure	100 mT
Oxygen flow rate	2 sccm
Power	100 W
CF_4	20 sccm
Time	15 sec

Table 4.3 – The process parameters in PE mode used for forming the desired oxide

Parameter	Value
Oxygen pressure	500 mT
Oxygen flow rate	100 sccm
Power	150 W
Time	5 mins

4.4.3 ALD deposited metal-oxide

Atomic Layer Deposition (ALD) is a technique used in depositing high quality thin films of a range of materials, including metals [7-11], metal-oxides [12-14] and more recently organics [15], with accurate thicknesses, on the surface of a sample. The deposition process consists of sequential alternating pulses of gaseous chemical precursors that react with the surface of the sample. These individual gas-surface reactions are called half-reactions [16] and appropriately make up only part of the materials synthesis. During each half-reaction, the precursor is pulsed into a chamber (reactor) under vacuum for a designated amount of time to allow the precursor to fully react with the sample surface through a self-limiting process that leaves no more than one monolayer at the surface. Subsequently, the chamber is purged with an inert carrier gas (typically N_2 or Ar) to remove any residual precursor molecules. This is then followed by the counter-reactant precursor pulse and purge, creating up to one layer of the desired material. This process is then cycled until the desired film thickness is achieved. Therefore, by a careful selection of the number of cycles, materials with high uniformity and precise thicknesses can be formed on the surfaces of samples. The major advantage the ALD technique presents over other deposition techniques is the excellent control of the thickness of a very thin film (1 to 10 nm).

An Ultratech Savannah G2 ALD was used in this project to grow an Al_2O_3 dielectric layer by using trimethylaluminum (TMA) and water (H_20) vapour precursors.

4.4.4 Self-assembled organic insulator

The most common material used as the insulating layer in MIM diodes is the metal oxide [3, 5-6, 17-19], with some of the deposition techniques utilised described above. In this project, a novel low-cost technique has been proposed. The proposed insulating layer consist of octadecyltrichlorosilane (OTS) sandwiched between two metals as shown in Figure 4.2. The OTS is a self-assembled monolayer (SAM) [20-25] commonly used to functionalise the surface of silicon dioxide (SiO_2) [21-22, 25], and in thin film form has a typically thickness of approximately 2 nm [26-27].

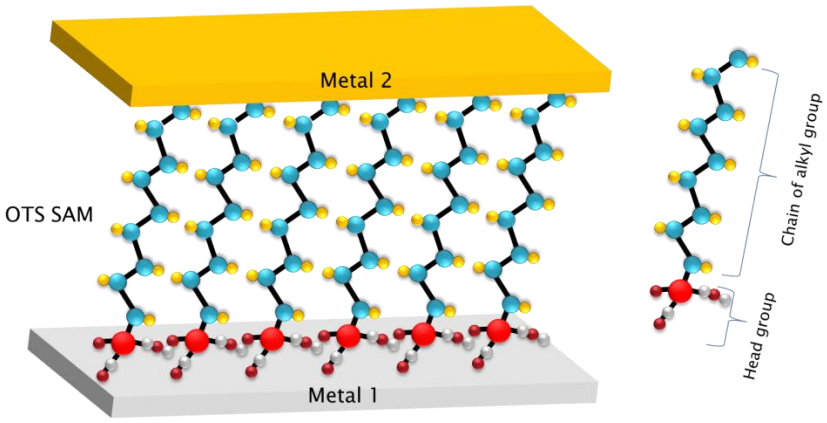

Figure 4.2 – Basic MIM diode structure showing OTS (formed in between two metals) used as an insulating layer.

The OTS is an amphiphilic molecule consisting of a long-chain alkyl group ($C_{18}H_{37}$–) and a head group ($SiCl_3$–), which forms Self Assembled Monolayers (SAMs) on various substrates, with silicon dioxide (SiO_2) being the most common. The surface of the substrate, on top of which the OTS is to be deposited, needs to be tailored to have a good affinity with the head group of the OTS molecule.

The OTS solution preparation and deposition took place with an OTS/hexane solution (1 part of OTS in 2000 part of hexane by volume) prepared in a beaker and sonicated for 25 minutes to aid uniformity. A base metal layer (titanium) with a nominal thickness of 25 nm, deposited onto a borosilicate glass substrate by e-beam evaporation, was immersed in the OTS/hexane solution and left for an hour without stirring, after which it was removed and immediately submerged in hexane and sonicated for a further 15 minutes in order to remove any unwanted polymerised OTS particles that may have adhered to the titanium surface. The substrate was then baked for 30 minutes at 90 °C to complete the OTS polymerisation and to remove any residual solvent.

(a)

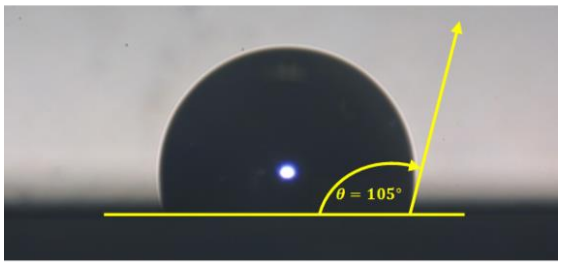

(b)

Figure 4.3 – Contact angle of titanium (a) before, and (b) after OTS deposition, showing increased hydrophobicity.

As can be seen in Figure 4.3(a) prior to OTS deposition, the surface of the titanium film as deposited is hydrophilic, indicating the presence of OH groups, with a contact angle ϑ = 10°. After OTS deposition, a SAM formed on the titanium surface, making it highly hydrophobic with a contact angle ϑ = 105°, as shown in Figure 4.3(b), which is typical for an OTS covered surface [26-27].

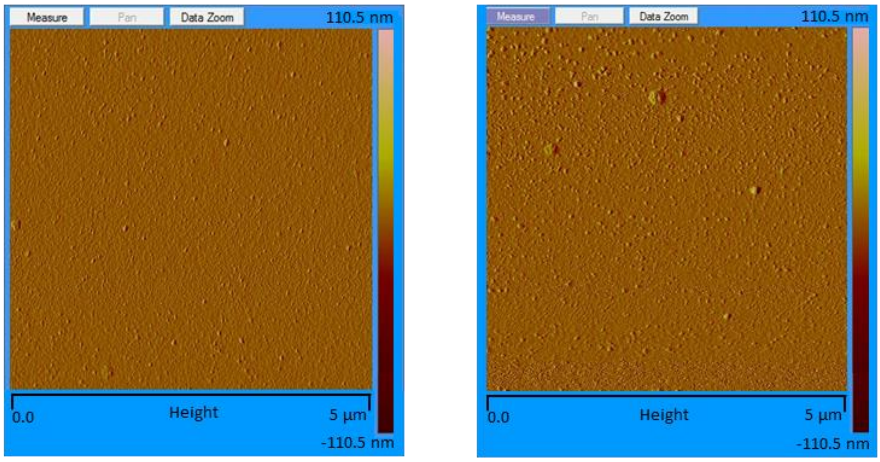

Figure 4.4 – AFM pictures showing the surface roughness of titanium film before (a) and after OTS deposition (b).

As can be seen in Figure 4.4, atomic-force microscopy (AFM) showed no significant difference in the surface roughness of the titanium surface before and after OTS deposition. This is to be expected due to the nanometer scale thickness of the OTS SAM.

The advantage the SAM insulator presents over the metal oxides is that the OTS molecules assemble with a very tight bond, hence significantly minimising the presence of pin holes which is predominant in oxides. Also, uniformity across the entire diode junction area is significantly improved, as the monolayer cannot grow higher than the height of the molecule it is made of. This means that the thickness of the OTS film is the same throughout the surface of the base metal. If there is any roughness at the surface of the metal, it is more likely to be as a result of the metal roughness and not due to any variations in the thickness of the OTS film. Also, the OTS deposition process is carried out at low temperature compared to the aggressive oxidation process. This means that with the OTS as insulating layer, the possibility of fabricating the diodes on a flexible substrate is high.

4.5 Flexible substrate

With the OTS deposition process being carried out entirely at low temperature (as stated in Section 4.4.4), a possibility is presented for MIM diodes to be fabricated on a flexible substrate with roll-to-roll manufacturing. While there are existing films such as acetate and polyethylene terephthalate (PET), which can easily be used as a flexible substrate, these materials have issues with metal adhesion, and do not have the thermal properties suitable for the temperatures involved in the process of the diode fabrication. For example, the PET film, which possesses a higher thermal capability than the acetate film, starts to lose its original physical shape due to thermal expansion when subjected to temperatures from 130 ^{o}C. These materials are therefore not suitable, as the diode fabrication process involves temperatures of up to 200 ^{o}C. The polyimide solves this issue, as it has a curing temperature of between 350 to 400 ^{o}C [28], which is comfortably above the maximum temperature (200 ^{o}C) involved in the device production process.

The polyimide used to form a substrate was PI-2610 (HD Microsystems). PI-2610 is a high molecular weight and fully aromatic polyimide which is formed from polyamic acid precursors dissolved in an N-methyl-2-pyrrolidone based solvent carrier [28]. This means that the polyimide can be spin coated on a carrier wafer and cured by baking, creating a thin, flexible and robust polymer strong enough to act as a self-supporting substrate which can be patterned upon and then peeled from the carrier wafer. The thickness is controlled by the spin speed, and several layers can be applied to produce a thicker flexible substrate [28].

Once the polyimide substrate had been created on a 2 inch silicon “carrier wafer”, the diode fabrication stages were the same as in Section 4.2. However, in addition, to improve adhesion of the metal to the substrate, the substrate was subjected to a reactive ion etch (RIE) with the parameters given in Table 4.4.

Table 4.4 – The process parameters used to improve the adhesion of metal to the polyimide substrate.

Parameter	Value
Oxygen pressure	150 mT
Oxygen flow rate	50 sccm
Power	75 W
Time	1 min

4.6 Electrical characterisation

4.6.1 DC analysis

The diodes were characterised electrically using a Cascade RF/DC manual probe station with two probes connected to an Agilent B2902A (SMU) parameter analyser. The voltage range was kept within ±0.3 V for the metal oxide diodes, and ±0.2 V for the OTS diodes in order to avoid damaging the diode junctions, as the OTS diodes were found to have an irreversible breakdown voltage of ±0.35 V.

The diodes' electrical parameters, such as the curvature coefficients and resistances, were obtained from the results of a 9^{th} order polynomial fitted to the diodes' raw *J-V* data.

4.6.2 Automated testing

In order to investigate the life span of the diodes with respect to time and current stressing, an ARM Cortex M3 (MBed LPC1768), which has a digital to analogue converter (DAC) as well as multiple analogue to digital converters (ADC) was used to bias the diode remotely. The multiple ADCs allow for multiple devices to be tested at the same time. A C programming language programme was compiled in the microcontroller, which allows

the mbed to generate a sinusoidal voltage, which is then used as the diodes' input voltage. A series resistor (10 to 15 times larger than the resistance of the diodes) was connected between the diode and the generated sinusoidal voltage from the mbed in order to reduce the voltage to values that the diodes are able to safely operate in. Buffers were then connected at all the outputs to prevent loading. The mbed is powered using the computer USB port, and generates the sinusoidal waveform automatically based on the program, biasing the diodes (hence current stressing the diodes) periodically and storing the *J-V* characteristics data for further analysis.

4.6.3 Temperature dependence measurements

In order to gain an understanding of the nature of the conduction mechanisms occurring in the diodes, the diodes were placed in an environment cooled down to 2.5 K using a closed cycle JANIS SHI-4 Optical cryostat, and *J-V* measurements performed on them at various temperature ranging from 2.5 K to 296 K. The cryostat was connected to a LakeShore 340 Temperature Controller and an Agilent B2902A (SMU) parameter analyser, and controlled via a Matlab-based software.

The closed cycle cryostat is comprised mainly of a cold-head, compressor, vacuum shroud, and radiation shield as shown in Figure 4.5. The cold-head is where the refrigeration cycle takes pace. It is connected to a compressor by two gas lines and an electrical power cable. One of the gas lines supplies high pressure helium gas to the cold-head, the other gas line returns low pressure helium gas from the cold-head. The compressor provides the necessary helium gas flow rate at the high and low pressure for the cold-head to convert into the desired refrigeration capacity. The vacuum shroud surrounds the cold end of the cold-head in vacuum, where the sample is mounted, limiting the heat load on the cold-head caused by conduction and convection. The radiation shield insulates the sample from the room temperature thermal radiation being emitted from the vacuum shroud.

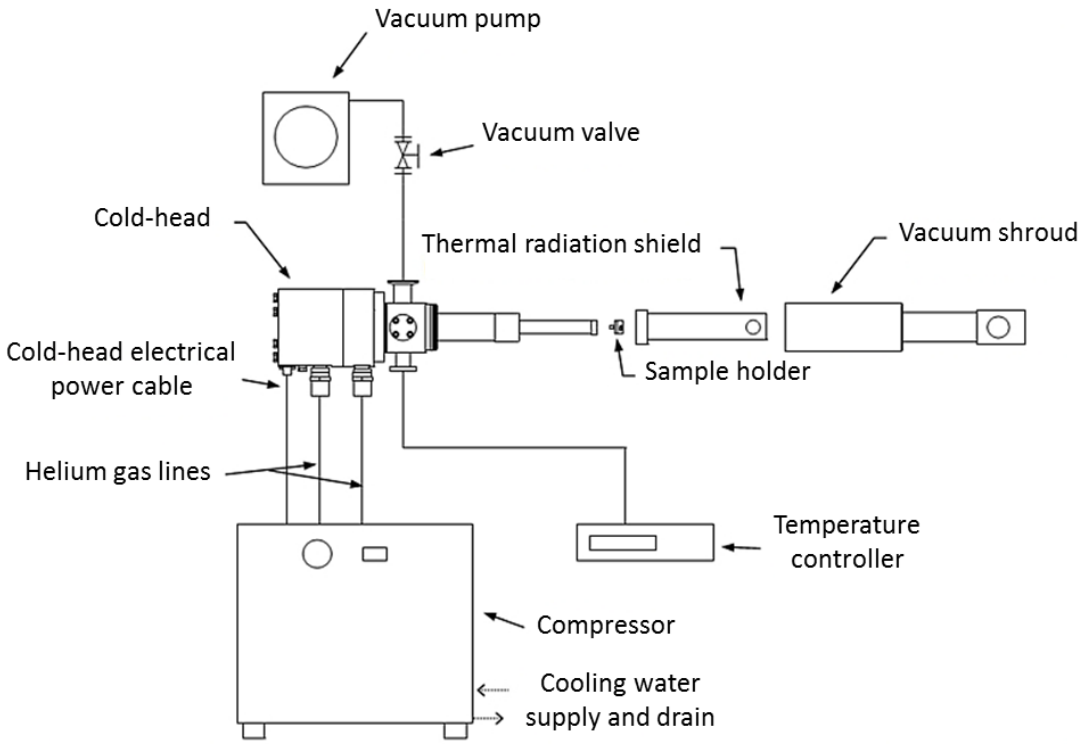

Figure 4.5 – Schematic diagram of closed cycle cryostat configuration including connections to a compressor, pump and temperature controller (adapted from [29]).

The temperature controller connected to the cryostat measures and adjusts the sample temperature. *J-V* measurements are then performed on the sample at the set desired temperatures using the network analyser.

4.6.4 Microwave analysis

4.6.4.1 Vector Network Analyser (VNA)

The Vector Network Analyser (VNA) is an instrument widely used for RF/Microwave design applications. VNAs are used mostly at high frequencies ranging from 5 Hz to 1.05 THz [30-31]. The instrument can be used to feed RF signal into an electrical network, and to characterise the network, in terms of network scattering parameters (i.e. S parameters). S-parameters are complex vector quantities that represent the ratio of two RF signals. S-parameters have a magnitude and phase, or in Cartesian form, real and imaginary terms.

The parameters are expressed as S_{xy} where X represents the device under test (DUT) output port being measured and Y denotes the DUT input port stimulated by the incident RF signal [32]. Figure 4.6 shows a simple two-port device with each port denoted with RF wave complex amplitudes (a and b), which can be used to work out the S-parameters.

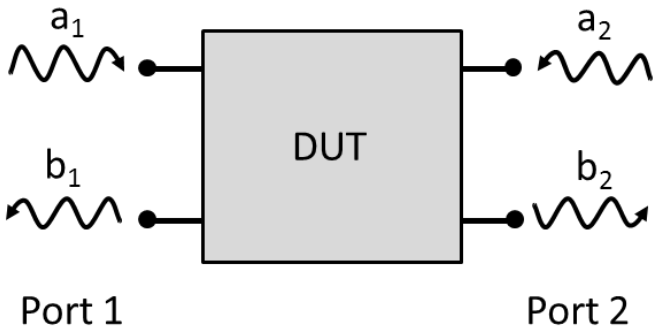

Figure 4.6 – Block diagram of a simple two-port device denoted with RF wave complex amplitudes a and b (adapted from [31]).

As expressed in Equation 4.1, S_{11} is defined as the ratio of the energy reflected at port one to the incident signal placed on port one. S_{21} is defined as the ratio of the energy transmitted through the DUT present at port two to the incident signal placed on port one (see Equation 4.2). Both of these quantities, S_{11} and S_{21} are referred to as forward S-parameters because the incident signal originates from the RF source on port one [31].

$$S_{11} = \frac{b_1}{a_1} \tag{4.1}$$

$$S_{21} = \frac{b_2}{a_1} \tag{4.2}$$

S_{12} is the ratio of the energy transmitted through the DUT present at port one to the incident signal placed on port two (see Equation 4.3), and with the incident source on port two, S_{22} becomes the ratio of the energy reflected by port two, divided by the incident source energy at port two (see Equation 4.4).

$$S_{12} = \frac{b_1}{a_2} \tag{4.3}$$

$$S_{22} = \frac{b_2}{a_2} \tag{4.4}$$

S-parameters that describe transmission, such as S_{21}, are analogous to other familiar terms including gain, insertion loss, or attenuation. S-parameters that describe reflection, such as S_{11}, correspond to voltage standing wave ratio (VSWR), return loss, or reflection coefficient [32]. An Agilent HP 208753C and Agilent N5224 VNAs were used to perform RF characterisation on the MIM diodes and rectennas respectively.

4.6.4.2 Diode RF characterisation

Characterisation at high frequencies, ranging from 1 MHz to 3 GHz, was carried out on the diodes using a VNA (which injects power into the diode) and a Cascade RF/DC manual probe station (where the diodes are placed for testing), with two three point coplanar probes as leads connecting the VNA to the diodes. The diode rectified output voltage was measured for HF powers in the range -47 to -37 dBm. To enable HF testing, ten diodes were embedded within coplanar waveguides with a characteristic impedance of 50 Ω as seen in Figure 4.8, matched to the characteristic impedance of the coplanar probes, thus minimising unwanted reflections from the layout as well as reducing radiation losses. The diode structures can be seen as the small crossover lines, in between the three rectangular contact pads as shown in Figure 4.7. In order not to waste time carrying out AC measurements on a non-functional structure, DC measurements first of all took place through the method described in Section 4.6.1, and diode functionality was confirmed before AC measurements are performed. Because ten diodes are involved, there is a possibility of one or a few of them not functioning (either short circuited or open circuited). In the case of a short circuit, the entire structure will also be short circuited and will not

work, but In the case of an open circuit, the structure will work since the diodes are connected in parallel. In order to ensure that all the diodes were functional in the measurement, the structure parameters obtained from experimental results were compared with simulated results (using ADS) with ten diodes incorporated. There was a good agreement between the experimental and simulated in data used for analysis.

The data recovered from each AC measurement was used to calculate the voltage responsivity (which is a measure of the amount of output voltage per watt of input power, and is a common Figure of merit), capacitance and cut-off frequency of each device.

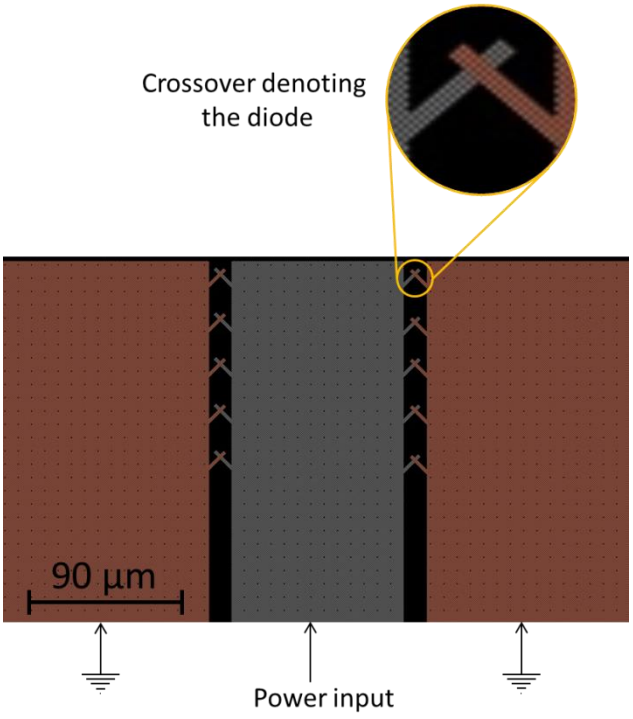

Figure 4.7 – Mask layout of diode AC tested using the VNA, showing the diode crossovers between the coplanar waveguide.

Apart from using the VNA as input power source for the diode, it was also used to measure and retrieve the structure's reflection coefficient S_{11} at each frequency, which can then be used in obtaining other parameters of the structure, including capacitance, resistance and input impedance Z_{IN}, in order to determine the parameters which influence its response.

The calculated input impedance was then used for comparison with that obtained from experimental results, retrieved by the VNA, for analysis. The ADS was also used in modelling the impedance matching network for the antenna utilised for the rectenna structures.

4.7 Rapid thermal annealer (RTA)

Rapid thermal anneal (RTA) is a process commonly used in the semiconductor industry to fabricate semiconductor devices through a process that heats up a sample using high intensity lamps. Unlike other annealing techniques, such as furnace annealing where processing a run may last for several minutes or hours, the rapid thermal annealing process last for a much lower time duration (in seconds). A custom designed vacuum RTA was used in this project to measure diodes' high temperature reliability. The devices were exposed to various different temperatures inside the RTA chamber in vacuum (in order to prevent any form of oxidation taking place) and *J-V* tested after each run to determine how the dielectric layers are being affected by increasing temperature. This is a valid test for the device, since it is a candidate for applications such as thermal energy harvesting, where it may be exposed to high temperatures.

4.8 Physical analysis

4.8.1 Atomic force microscopy (AFM)

Atomic Force Microscopy (AFM) is a very high resolution scanning equipment that is capable of measuring and generating an accurate topographic map of the surface of features with resolution as high as on the order of fractions of a nanometre [4, 33].

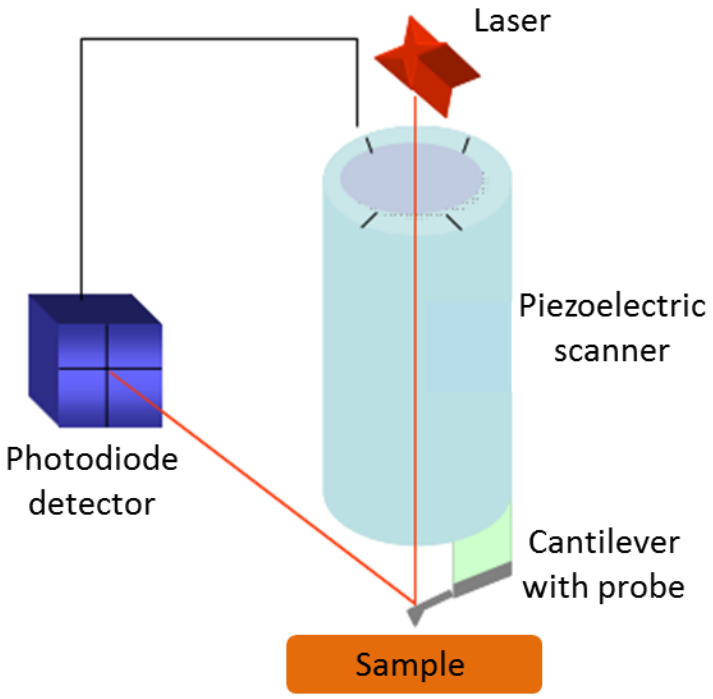

Figure 4.8 – Schematic of AFM instrument showing laser beam source method of detection and position sensitive photodiode detector (adapted from [34]).

The equipment uses a cantilever with a very sharp tip to scan over a sample surface as shown in Figure 4.8. As the tip approaches the surface, the close-range, attractive force between the surface and the tip causes the cantilever to deflect towards the surface. However, as the cantilever is brought even closer to the surface, such that the tip makes contact with it, increasingly repulsive force takes over and causes the cantilever to deflect away from the surface [33]. A laser beam is used to detect cantilever deflections towards or away from the surface. By reflecting an incident beam off the flat top of the cantilever, any cantilever deflection will cause slight changes in the direction of the reflected beam. A position-sensitive photo diode (PSPD) can be used to track these changes [33]. Thus, if an AFM tip passes over a raised surface feature, the resulting cantilever deflection (and the subsequent change in direction of reflected beam) is recorded by the PSPD. By using a feedback loop to control the height of the tip above the surface, thus maintaining constant

laser position, the AFM can generate an accurate topographic map of the surface features [33]. The Veeco Dimension 3100 AFM has been used for numerous tasks in this project, including measurements of metal and dielectric film uniformity, thicknesses, roughness calculations, diode crossover dimensions etc.

4.8.2 Scanning Electron Microscopy (SEM)

A Scanning Electron Microscopy (or SEM) is an instrument used in generating highly magnified images of a sample for analysis [35]. As shown in Figure 4.9, it uses a high energy electron beam generated by an electron gun, and processed by magnetic (condenser) lenses, to rapidly scan (raster) the surface of a sample using scanning (raster) coils. This results in the release of a shower of secondary electrons from the sample surface [35-36].

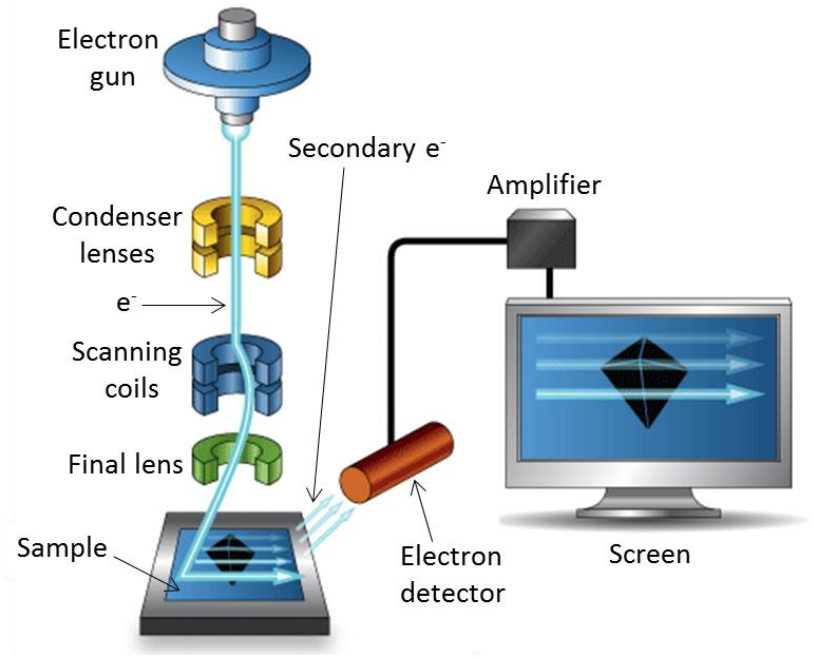

Figure 4.9 – Basic schematic of a SEM instrument (adapted from [36]).

These released secondary electrons are then collected by an electron detector located in the instrument's chamber, converted to photons via a scintillator, amplified in

a photomultiplier, and converted to electrical signals and used to modulate the intensity of the image on the viewing screen [36]. As the sample is being bombarded by electrons, it starts to conduct; therefore samples surfaces are commonly coated with gold before the process commences, to prevent localised charging [4]. A Hitachi S-2400 SEM has been used to provide topographical images of various samples in this project.

4.9 Summary

Various fabrication processes have been discussed, including the polyimide flexible substrate, bi-layer lift-off technique, metal deposition, and various dielectric deposition techniques which were used as the basis for the processes. The various characterisation techniques for both electrical and physical analysis were also discussed, including the *I-V* characteristics analysis, responsivity, lifetime measurements, temperature reliability test, measurement of rectenna detection, simulations and the various scanning electron techniques, which, when combined together, were used to determine the suitability of the various dielectrics for the MIM diode structure, and subsequently as a viable component in a rectenna. The application of these processes is discussed in the subsequent chapters of the thesis.

References

[1] Microchem, “LOR and PMGI Resists”, http://www.nfc.umn.edu/assets/pdf/pds/lor.pdf, Accessed online: 12 December 2015.

[2] Rohm and Haas Electronic Materials, “Megaposit SPR350 Series Photoresist Datasheet” http://docs.capitolscientific.com/manufacturer/dow_electronic_materials/datasheets/SPR350_Photoresist.pdf, Accessed online: 12 December 2015.

[3] L. E. Dodd, A. J. Gallant, and D. Wood, “Ti-TiOx-Pt Metal-Oxide-Metal Diodes Fabricated via a Simple Oxidation Technique”, *MRS Proceedings*, Vol. 1415, pp 1-4, (2012).

[4] L. E. Dodd, “Fabrication Optimization of Metal-Oxide-Metal Diodes”, *PhD thesis*, pp 127-132, http://etheses.dur.ac.uk/9474/1/Linzi_Dodd_d51hqe_thesis.pdf?, Accessed online: 12 December 2015.

[5] L. E. Dodd, A. J. Gallant, and D. Wood, “Controlled Reactive Ion Etching and Plasma Regrowth of Titanium Oxides of Known Thickness For Production of Metal-Oxide-Metal Diodes”, *IET Micro and Nano Lett.* Vol. 8, Issue 8, pp. 476-478 (2013).

[6] B. Tiwari, J. A. Bean, G. Szakmany, G. H. Bernstein, P. Fay, and W. Porod, “Controlled Etching And Regrowth of Tunnel Oxide For Antenna Coupled Metal-Oxide-Metal Diodes”, *J. Vacuum Sci. Technol. B,* Vol. 27, Issue 5, pp. 2153–2160, (2009).

[7] M. B. E. Griffiths, P. J. Pallister, D. J. Mandia, and S. T. Barry, “Atomic Layer Deposition of Gold Metal”, *Chem. Mater.,* Vol. 28, pp 44−46, (2016).

[8] P. G. Gordon, A. Kurek, and S. T. Barry, “Trends in Copper Precursor Development for CVD and ALD Applications”, *ECS J. Solid State Sci. Technol.,* vol. 4, Issue 1, pp 3188-3197, (2015).

[9] A. Niskanen, T. Hatanpaä, K. Arstila, M. Leskelä¨, and M. Ritala, “Radical-Enhanced Atomic Layer Deposition of Silver Thin Films Using Phosphine-Adducted Silver Carboxylates”. *Chem. Vap. Deposition,* Vol. 13, pp. 408−413, (2007).

[10] P. R. Chalker, S. Romani, P. A. Marshall, M. J. Rosseinsky, S. Rushworth, and P. A. Williams, “Liquid Injection Atomic Layer Deposition of Silver Nanoparticles”, *Nanotechnol.* Vol. 21, 405602, pp 1-7, (2010).

[11] M. Kariniemi, J. Niinisto, T. Hatanpaa, M. Kemell, T. Sajavaara, M. Ritala, and M. Leskela, “Plasma-Enhanced Atomic Layer Deposition of Silver Thin Films”, *Chem. Mater.* Vol. 23, pp 2901–2907, (2011).

[12] X. Wang, S. M. Tabakman, and H. Dai, “Atomic Layer Deposition of Metal Oxides on Pristine and Functionalized Graphene”, *J. Am. Chem. Soc.* Vol. 130, pp 8152–8153, (2008).

[13] D. M. Hausmann, E. Kim, J. Becker, and R. G. Gordon, “Atomic Layer Deposition of Hafnium and Zirconium Oxides Using Metal Amide Precursors”, *Chem. Mater.* Vol 14, pp 4350-4358, (2002).

[14] K. Kukli, M. Ritala, M. Schuisky, M. Leskelä, T. Sajavaara, J.i Keinonen, T. Uustare, and A. Hårsta, “Atomic Layer Deposition of Titanium Oxide from TiI_4 and H_2O_2”, *Chem. Vap. Deposition*, Vol. 6, Issue 6, pp 303-310, (2000).

[15] Ultratech, “Savannah G2 ALD system”, http://www.annealsys.com/docs/Savannah_G2_Datasheet-22-04-14-06.pdf Accessed online: 15 January 2016.

[16] R. W. Johnson, A. Hultqvist, and S. F. Bent, “A Brief Review of Atomic Layer Deposition: From Fundamentals to Applications”, *Mater. Today*, Vol. 17, Issue 5, pp. 236-245, (2014).

[17] A. B. Hoofring, V. J. Kapoor, and W. Krawczonek, “Submicron Nickel-Oxide-Gold Tunnel Diode Detectors for Rectennas”, *Journal of Appl. Phys.* Vol. 66, Issue 1, pp. 430-437, (1989).

[18] E. Wiesendanger and F. Kneubfuhl, “Thin-Film MOM-Diodes for Infrared Detection”, *Appl. Phys.* Vol. 13, pp. 343-349, (1977).

[19] M. R. Abdel-Rahman, B. Monacelli, A. R. Weeks, G. Zummo, And G. D. Boreman, “Design, Fabrication, and Characterization of Antenna-Coupled Metal-Oxide-Metal Diodes for Dual-Band Detection”, *Optical Engineering,* Vol. 44(6), pp. 1-6, (2005).

[20] H. Klauk, U. Zschieschang, J. Pflaum, and M. Halik, “Ultralow-Power Organic Com-Plementary Circuits” *Nature* 445, 745-748, (2007).

[21] S. Rena, S. Yanga, Y. Zhaob, J. Zhoua, T. Xua and W. Liu, “Friction and Wear Studies of Octadecyltrichlorosilane SAM on Silicon”, *Tribology Letters*, Vol. 13, Issue 4, pp 233-239, (2002).

[22] K. H. Cha, and D. E. Kim, “Investigation of the Tribological Behavior of Octadecyltrichlorosilane Deposited on Silicon” *Wear*, Vol. 251, Issues 1–12, pp 1169–1176, (2001).

[23] Y. Liu, L. K. Wolf, and M. C. Messmer, “A Study of Alkyl Chain Conformational Changes in Self-Assembled n-Octadecyltrichlorosilane Monolayers on Fused Silica Surfaces”, *Langmuir,* Vol. 17 Issue 14, pp 4329–4335, (2001).

[24] P. Fontaine, D. Goguenheim, D. Deresmes, and D. Vuillaume, “Octadecyltrichloro-Silane Monolayers as Ultrathin Gate Insulating Films in Metal-Insulator-Semiconductor Devices”, *Appl. Phys. Lett***.** 62, 2256 (1993).

[25] Y. Wang and M. Lieberman, “Growth of Ultrasmooth Octadecyltrichlorosilane Self-Assembled Monolayers on SiO_2”, *Langmuir*, Vol. 19 (4), pp 1159–1167, (2003).

[26] J. Dong, A. Wang, K.Y. S. Ng, and G. Mao, “Self-Assembly of Octadecyltrichlorosilane Monolayers on Silicon-Based Substrates by Chemical Vapor Deposition”, *Thin Solid Films* Vol. 515, pp 2116–2122, (2006).

[27] M. H. Jung and H. S. Choi, “Characterization of Octadecyltrichlorosilane Self-Assembled Monolayers on Silicon (100) Surface”, *Korean J. Chem. Eng.,* Vol. 26(6), pp 1778-1784, (2009).

[28] HD MicroSystems. Product Bulletin: PI-2600 Series–Low Stress Polyimides, *(*2009).

[29] Advanced Research Systems, “Closed Cycle Cryocooler Principles of Operation,” http://www.arscryo.com/tech-notes/cryocooler-principle-of-operation.html, Accessed online: 27 May, 2016.

[30] Agilent, “HP 208753C product manual”, http://exodus.poly.edu/~kurt/manuals/manuals/HP%20Agilent/HP%208753C%20User.pdf, Accessed online: 25 February, 2016.

[31] Agilent, “N5224 product manual”, http://cp.literature.agilent.com/litweb/pdf/N5224-90001.pdf, Accessed online: 25 February, 2016.

[32] National Instruments, “Fundamentals of Network Analysis,” file:///C:/Users/ckts17/Downloads/NI-Tutorial-11640-en.pdf, Accessed online: 25 February, 2016.

[33] Park Systems, “Atomic Force Microscopy,” http://www.parkafm.com/index.php/medias/nano-academy/how-afm-works, Accessed online: 27 May, 2016.

[34] Basic Theory, “Atomic Force Microscopy” http://asdlib.org/onlineArticles/ecourseware/Bullen/SPMModule_BasicTheoryAFM.pdf, Accessed online: 01 November, 2016.

[35] Working Principle of Electron Microscopes, http://www.yourarticlelibrary.com/micro economics/working-principle-of-a-electron-microscopes-with-diagram/26479/, Accessed online: 02 November, 2016.

[36] My Scope “Scanning Electron Microscopes Layout,”http://www.ammrf.org.au/my scope/sem/practice/principles/layout.php, Accessed online: 02 November, 2016

Chapter 5

Metal-Insulator-Metal (MIM) Diode Production Using Octadecyltrichlorosilane (OTS) as the Insulator

5.1 Introduction

This chapter discusses the fabrication and testing of metal-insulator-metal (MIM) diodes using an insulator, which self-assembles as a monolayer on a metal surface. The diode fabrication processes and electrical analysis, which include *J-V* characteristics, curvature coefficient, and resistance, are discussed. An encapsulation method to prevent the degradation of rectified current associated with the MIM diodes has also been developed and is discussed in detail.

5.2 Motivation for the production of OTS diodes

The main challenge in the fabrication of a MIM diode is with the dielectric deposition; a very thin dielectric has to be used, usually 1-4 nm thick, corresponding only to a few atomic layers. This often results in a defective layer, which gives rise to non-uniform electric field across the device junction area, reducing the device rectified current [1]. In some instances,

the defects in the dielectric results in a large number of pin holes, short-circuiting the diode terminals and drastically reducing yield.

Initial MIM diodes were fabricated using TiO_x as the dielectric [2-3]. The TiO_x dielectric layer was deposited in between platinum and titanium electrodes (which have a work-function difference of 1.4 eV) using the furnace oxidation technique. Electrical characterisation of the devices showed that they have a non-linear *J-V* characteristic, and zero bias curvature coefficient ($\gamma_{\_ZB}$) of up to 5.5 V^{-1} [2-4]. However, the devices were found to have a significant variation in electrical results between diodes [4]. The dielectric layer was rough and had a non-uniform thickness across the diodes' junction area; this is a problem associated with the dielectric deposition techniques available [4]. Figure 5.1(a) shows TEM cross-section image of the fabricated Pt-TiO_x-Ti diode, with the roughness at the metal-oxide layers interface visible. Improvements were made on the device with the TiO_x layer deposited using plasma etch and deposition (PE). Figure 5.1(b) shows the image of a plasma diode, and as can be seen, the interfacial roughness between the metal-oxide layers was significantly reduced. The plasma diodes also had less variation in electrical results.

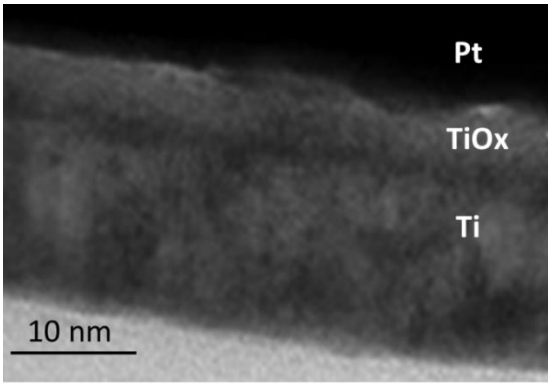

(a)

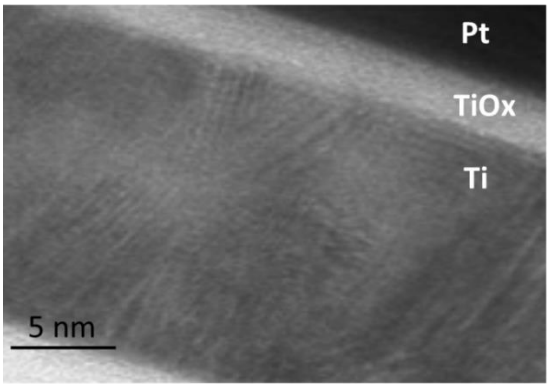

(b)

Figure 5.1 – TEM images showing the cross-section of fabricated Pt-TiO_x-Ti diodes with the oxide layers formed using furnace oxidation (a) and plasma etch (b) techniques (taken from [3]).

Furthermore, the dielectric (TiO_x) layer of the devices [2-3] had a very complex stoichiometry as investigated in [4], and can be seen in Figure 5.2. That was another major issue associated with the devices, as it is extremely difficult to understand and accurately characterise the nature of current flowing through the dielectric.

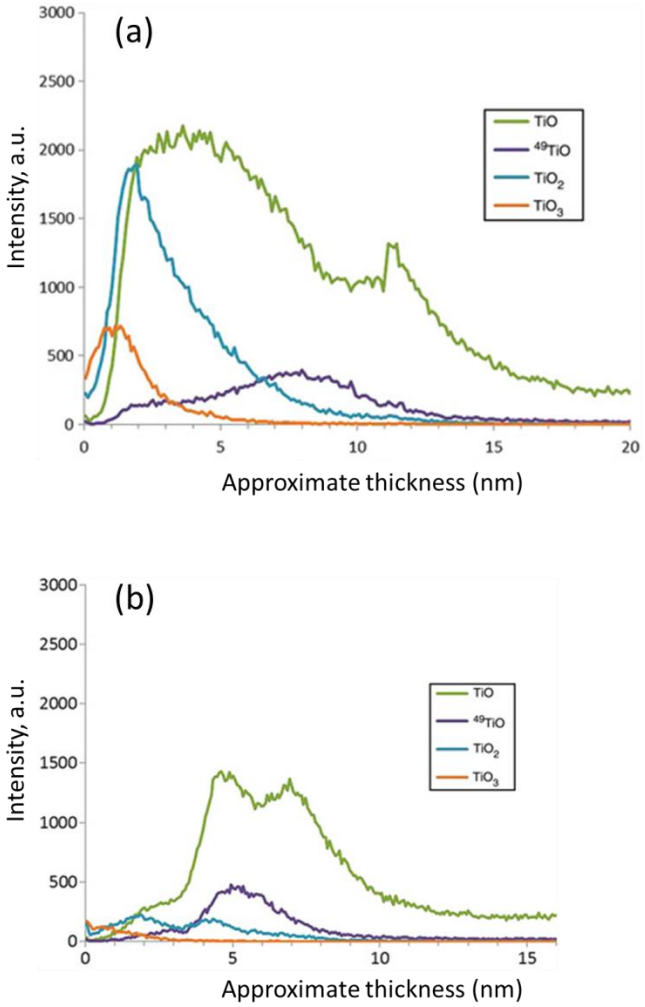

Figure 5.2 – Plot of the stoichiometric analysis of formed furnace (a) and (b) plasma oxides (taken from [3]).

The stoichiometric analysis showed (in Figure 5.2) that the oxide layer is comprised of different oxides of titanium, which caused uncertainties in the electrical behaviour of the devices. It was thought that this issue could also result in alternate transport mechanisms in the device [1].

Overcoming these problems was the motivation for developing a novel technique for manufacturing the MIM diode, using an insulator, which self-assembles in a monolayer onto a metal surface. The developed method used an octadecyltrichlorosilane (OTS) self-assembled monolayer (SAM) [5-10], which consists of carbon chains strongly packed together (pin-hole free) with an overall thickness of approximately 2 nm [11-12]. Due to the

nature of self-assembly, a second layer cannot grow on top of the first one, resulting in an extremely uniform thickness over large areas determined by the SAM chemistry. The manufacturing processes and materials involved are more environmentally friendly, highly repeatable and are also compatible with large-area roll-to-roll processes.

5.3 Diode fabrication

The formulation of the OTS solution was performed using the process detailed in Section 4.4.4. However, Figure 5.3 (not drawn to scale) shows the basic fabrication process of the structure (as in [2] with the major difference being the use of OTS rather than TiO_x). A bilayer of approximately 25 nm of titanium coated with 100 nm of gold was deposited by e-beam evaporation and lift-off (a). After a further photolithographic step, gold was removed by an iodine/potassium-iodide (4:1:8 $KI:I_2:H_2O$) wet etch, leaving small regions of titanium exposed (b-c). After removing the photoresist (d) the exposed titanium was coated with OTS, which has a typically thickness of ~2 nm [11-12] (e) using the technique as described in Section 4.4.4. After a further photolithographic step, a thin layer of platinum with a thickness of 40 nm was evaporated on the sample and patterned via lift-off in the unexposed regions, resulting in the definition of small Ti/OTS/Pt junctions (g-h). The addition of leads and bonding pads concludes the MIM diodes fabrication.

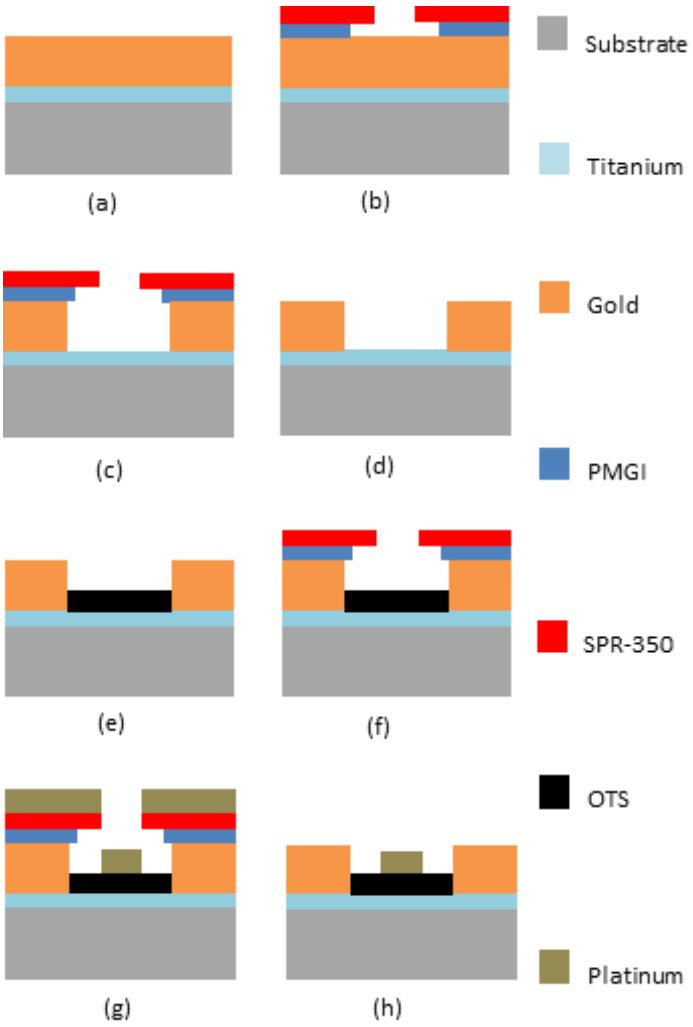

Figure 5.3 – The Ti/OTS/Pt MIM diode fabrication process. (a) Ti/Au bilayer on borosilicate glass. Photolithographic patterning (b) followed by Au wet etching (c). Photoresist stripping (d) and OTS deposition (e). Photolithographic patterning (f), Pt deposition (g) and lift-off (h).

A sketch of the device cross-section and a scanning electron microscopy (SEM) image of a fabricated structure can be seen in Figure 5.4, where the OTS layer is sandwiched between the two metal layers at the crossover of the two arms which defines the MIM junction. The feature size of the fabricated diode junction is 2 µm x 2 µm. This process can also be used in the fabrication of MIM diodes on a flexible plastic substrate [13], since only low-temperatures are required.

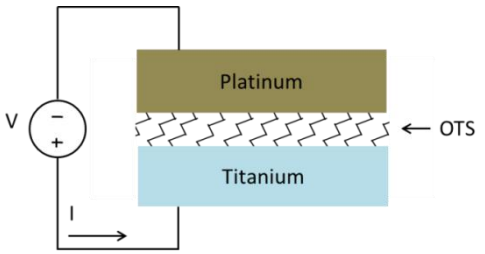

(a)

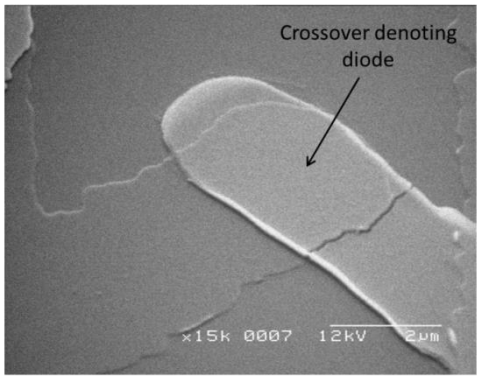

(b)

Figure 5.4 – A sketch of the device cross-section (a) and a SEM image of a fabricated Ti/OTS/Pt MIM structure (b). The titanium and platinum layers act as the anode and the cathode, respectively.

5.4 Results and discussions

5.4.1 DC characterisation

The diodes were electrically characterised using a parameter analyser. The diodes were tested over a voltage range of ±0.2 V in order to avoid damaging their junctions, as they were found to have an irreversible breakdown voltage of approximately ±0.35 V. The breakdown mechanism is a short circuit. A typical *J-V* characteristic of the diode is plotted in Figure 5.5, showing a strong non-linearity at zero bias (i.e. $V = 0$ V). The zero bias curvature coefficient (γ_{ZB}) shown in Figure 5.6, defined by Equation (5.1), was consistently found to be approximately 5.4 V^{-1}, which is a highly competitive value when compared with those available in the literature [14].

$$\gamma_{\_ZB} = \left. \frac{d^2I}{dV^2} \middle/ \frac{dI}{dV} \right|_{V=0} \tag{5.1}$$

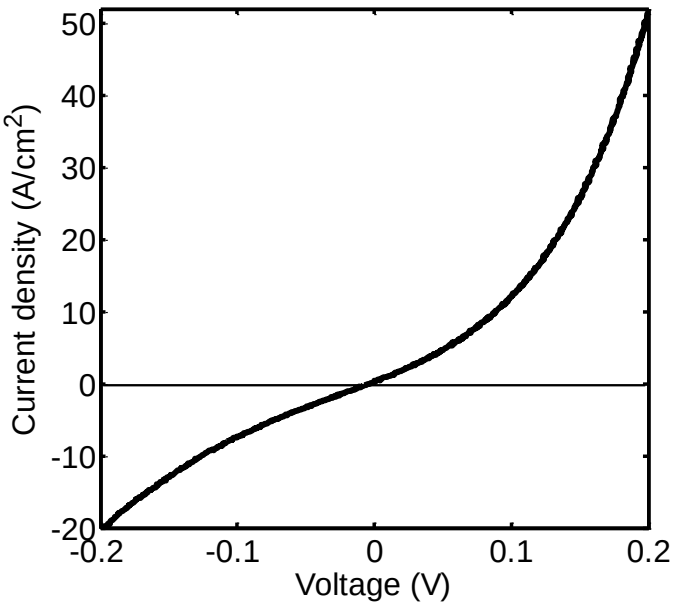

Figure 5.5 – Typical J-V characteristics of a fabricated Ti/OTS/Pt MIM diode.

Also, the device typical variation in resistance with voltage can be seen in Figure 5.7, with the zero bias resistance (R_0) being approximately 80 kΩ, a value much smaller than those available in the literature (typically in the MΩ regime [15]).

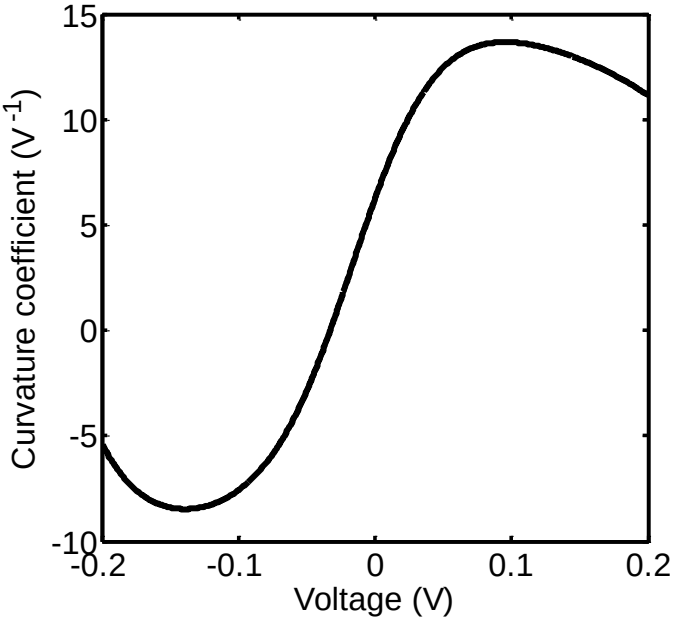

Figure 5.6 – Typical curvature coefficient vs voltage of a fabricated Ti/OTS/Pt MIM diode.

The relatively small resistance associated with the diode is attributed to the very thin OTS layer (~2 nm). The resistance can be used in predicting the nature of the conduction mechanism of the diode [16].

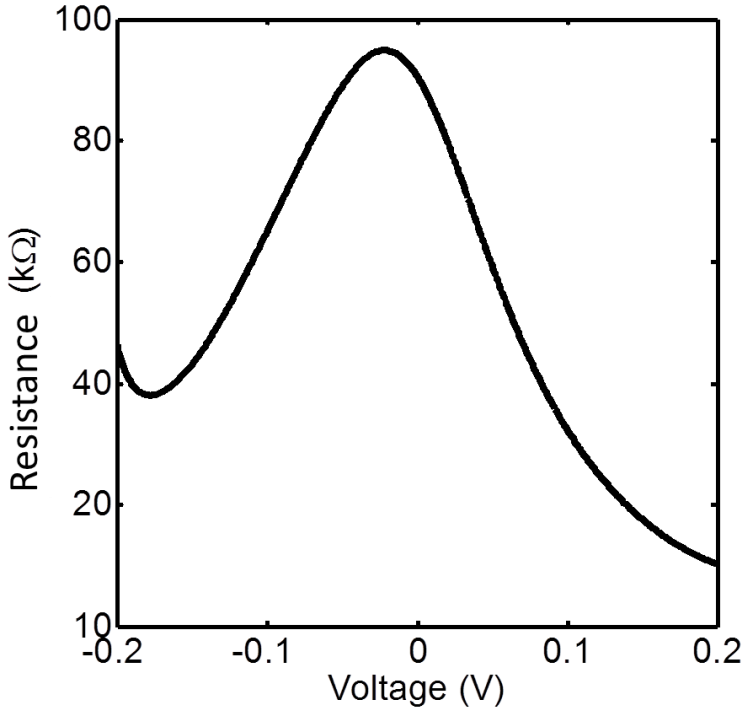

Figure 5.7 – Typical resistance vs voltage of the fabricated Ti/OTS/Pt MIM diode.

The curvature coefficient and resistance (Figures 5.6 and 5.7) have a complex shape. This might be related to the effect of series resistance but we are not certain that is the cause. This is, however, not an issue within the scope of this project, as we are more interested in the diode's zero-bias behaviours.

5.4.2 RF characterisation

RF characterisation, from 1 MHz to 3 GHz, was carried out on the diodes using a Vector Network Analyser (VNA). The rectified output voltage was measured for RF powers in the range 20 to 200 nW (-47 to -37 dBm). To enable the RF testing, ten diodes were embedded within coplanar waveguides (shown in Figure 4.8) with a characteristic impedance of 50 Ω, matched to the characteristic impedance of the VNA coplanar probes, thus minimising unwanted reflections from the layout as well as reducing radiation losses.

Figure 5.8 shows a typical rectified output voltage of the diode as a function of RF power injected into the coplanar waveguide at a frequency of 1 GHz. Figure 5.9 shows how the voltage rectified by the diode changes as a function of the operating frequency with a constant input RF power of approximately 100 nW (-40 dBm).

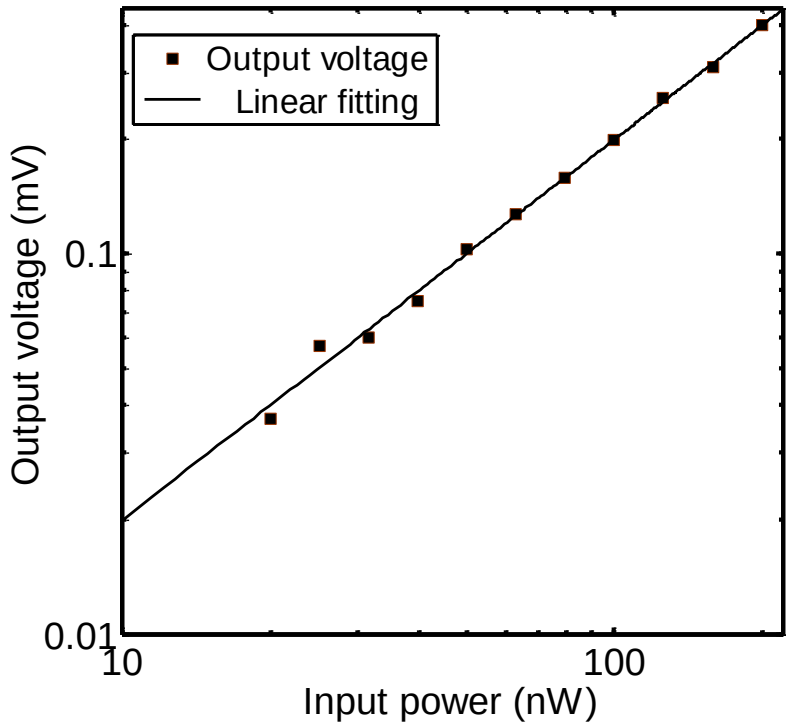

Figure 5.8 – Rectified voltage as a function of input RF power at a frequency of 1 GHz.

All measurements were carried out at room temperature, and the input RF power compensated at different frequencies to account for the measured losses in the cables, probes and coplanar waveguides. The diode voltage responsivity (R_v) is defined as;

$$R_v = \frac{V_{OUT}}{P_{RF}} = \frac{d^2V}{dI^2} \Big/ \frac{dV}{dI} \tag{5.2}$$

Where V_{OUT} = rectified voltage and P_{RF} = RF power fed into the coplanar waveguide by the VNA. Its value was determined by a linear fitting of the rectified output voltage as a function of the input RF power, shown in Figure 5.8, and had an absolute value of

approximately 1.9 kV/W at a frequency of 1 GHz, comparable to state-of-art Schottky diode detectors [17].

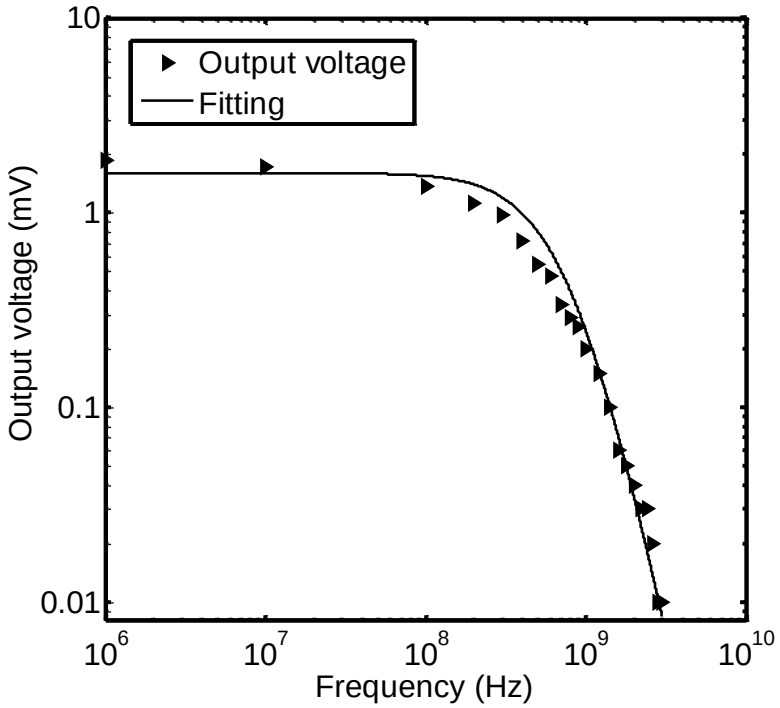

Figure 5.9 – Rectified voltage as a function of the frequency. The input power was kept constant at approximately 100 nW (-40 dBm).

The frequency response of the diode, measured up to 3 GHz, is shown in Figure 5.9; it exhibits a typical first-order dependence for frequencies above 0.5 GHz, which can be fit by Equation 5.3:

$$|V_{DO}| = \left|\frac{{V_o}^2}{1+(f/f_c)^2}\right| \tag{5.3}$$

where V_{DO} is the magnitude of the voltage rectified by the diode, V_o is the amplitude of the RF input voltage, f the frequency, and f_c the -3dB cut-off frequency typical of a first-order system.

In order to determine which parameters influence the diode response, it was assumed that the diode embedded in the coplanar waveguide could be described by the simple detection circuit shown in Figure 5.10. The values of the components, capacitors and resistors, were determined by measuring the reflection coefficient $S_{11,}$ of the whole structure, as a function of the frequency using the VNA, and converting it to the input impedance Z_{IN} using Equation 5.4:

$$Z_{IN} = Z_o \left(\frac{1+s_{11}}{1-s_{11}}\right) \tag{5.4}$$

where Z_o= 50 Ω is the characteristic impedance of the microwave probes and VNA ports. The real and imaginary parts of Z_{IN} as a function of the frequency are plotted in Figure 5.11. The numerical fitting of both curves resulted in a series resistance $R_s = 32$ Ω and a parallel capacitance $C_P = 3.1$ pF. The series resistance is as a result of the thin metal layer used for the coplanar waveguide (approximately 100 nm of gold) and of the platinum and titanium diode terminals.

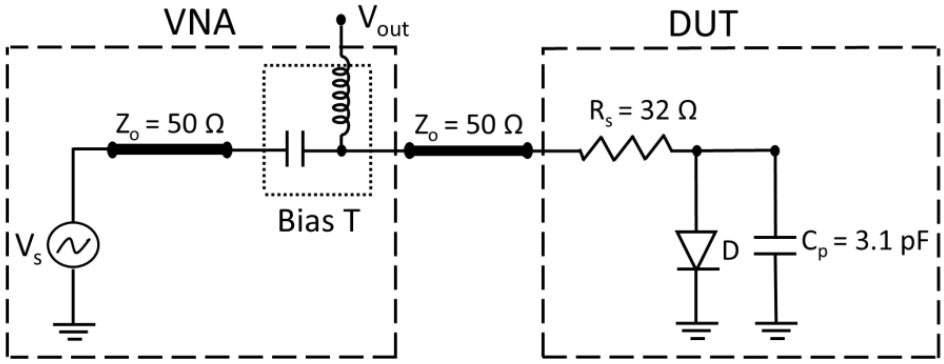

Figure 5.10 – Equivalent high-frequency circuit diagram for the diode characterisation. The series resistance R_s and parallel capacitance C_P were extracted by measuring and fitting the reflection coefficient S_{11} as a function of the frequency.

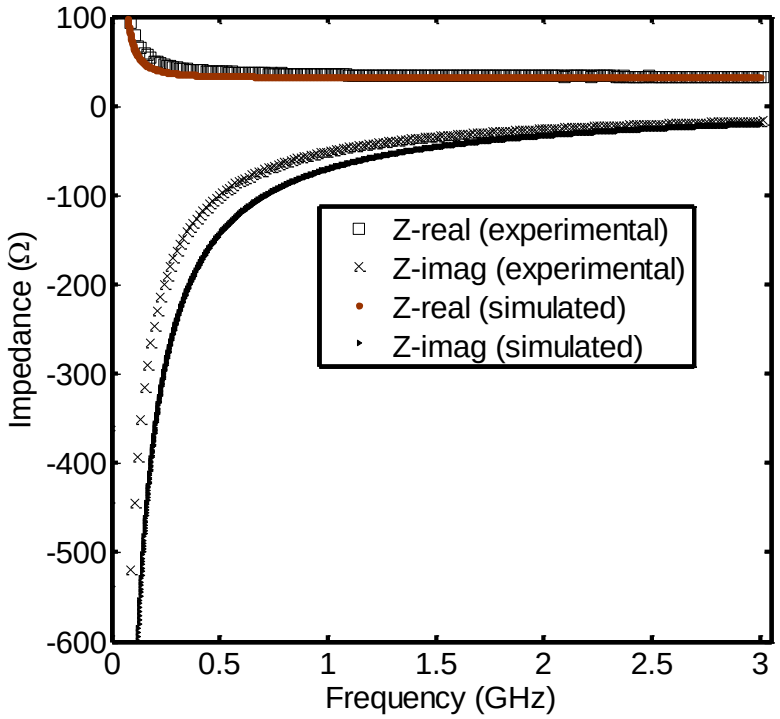

Figure 5.11 – Measured and simulated diode impedance as a function of the frequency.

The 3.1 pF parallel capacitance was much higher than expected from the parallel-plate capacitors associated to the diode junction, which was 0.2 pF. The additional capacitance is ascribed to a fringe effect of the diode leads. This was confirmed by performing electromagnetic simulations of the whole structure (using Agilent Advance Design System (ADS)), which is in good agreement with the measured data. A comparison between the simulated input impedance and Z_{IN} is shown in Figure 5.11. The accuracy of the simulated impedance suffered from some uncertainty in the OTS dielectric constant ε_i; a value of ε_i = 3 was assumed throughout the investigation [18].

5.5 Transport mechanism

In order to determine what transport mechanism is occurring in the Ti/OTS/Pt device, temperature dependence measurement from 2.5 K to 296 K was performed on the structure using the optical cryostat described in Section 4.6.3. Figure 5.12 shows the typical device *I-V* characteristics for a selection of temperatures.

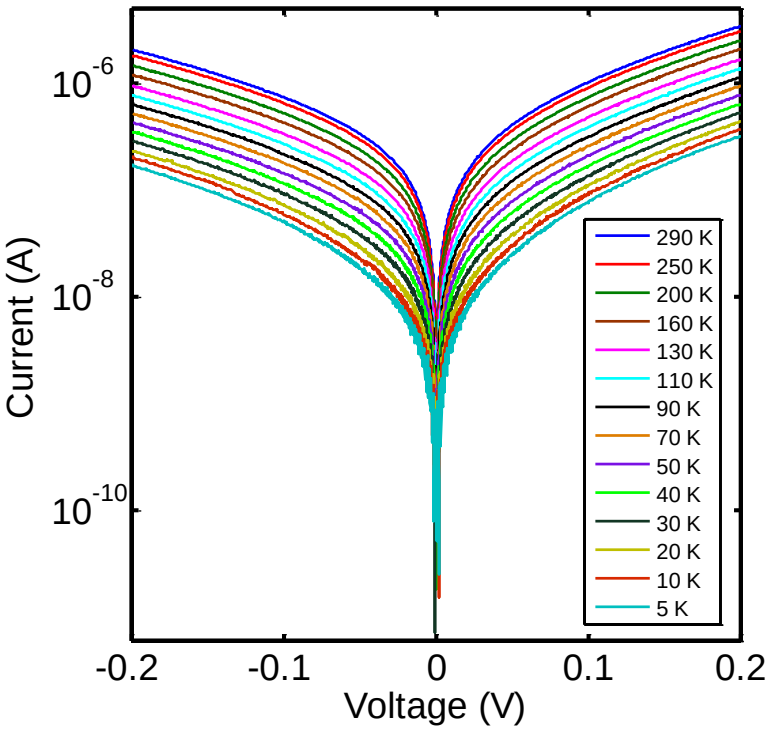

Figure 5.12 – *I-V* characteristics (in log scale) of the Ti/OTS/Pt device for a selection of temperatures.

Figure 5.13 shows the plot of the device current as a function of temperature at a voltage of 0.2V.

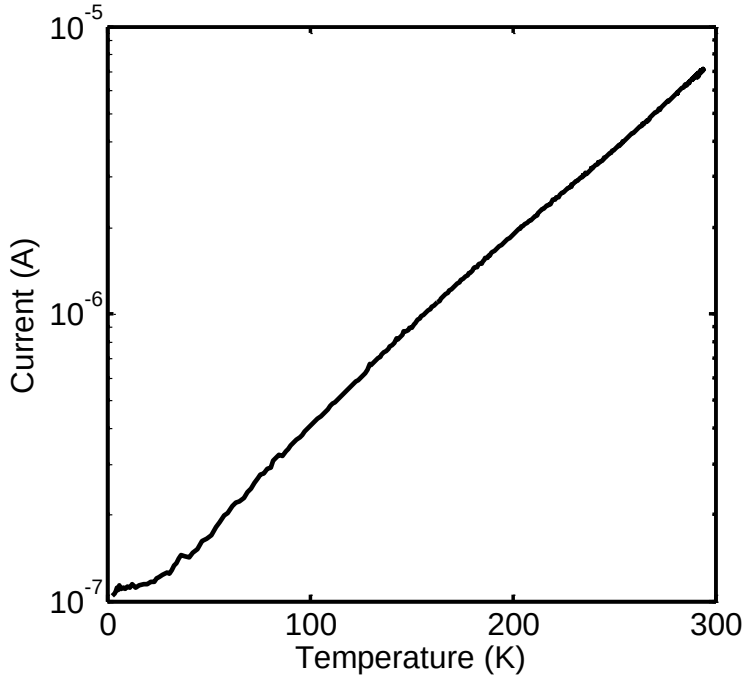

Figure 5.13 – Current vs temperature plot for the Ti/OTS/Pt structure.

It can be seen that the current is almost flat from temperature of 2.5 K to approximately 25 K. This suggests that electron tunneling was the dominant transport mechanism occurring in the diode while operating at these temperatures.

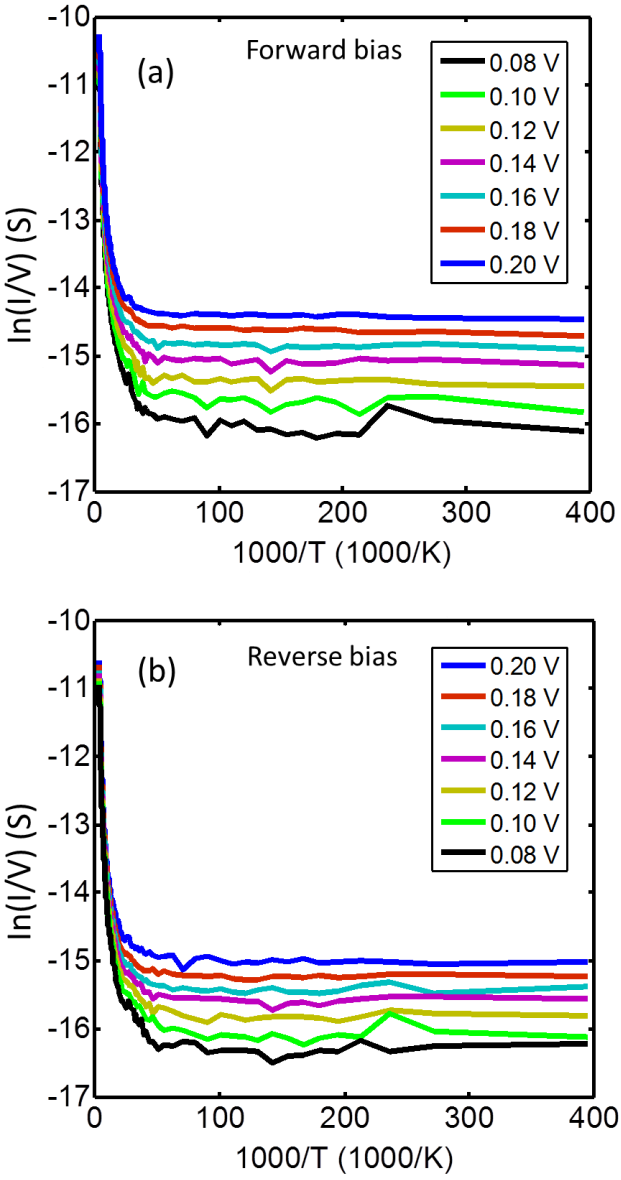

Figure 5.14 – *I-V* characteristics (conductance) vs temperature (2.5 K to 20 K) plot for the Ti/OTS/Pt structure for a selection of voltages. (a) is the forward bias plots, and (b) the reverse bias plots.

Figure 5.14 further suggested that there were no emission transport mechanisms occurring in the device at these low temperatures, as the *I-V* characteristics can be seen (Figure 5.14) to be temperature independent from 2.5 K up to approximately 20 K. However, as can be

seen in Figure 5.15, at higher temperatures (250 K and above), the *I-V* characteristics were strongly temperature dependent, which suggested that emission transport mechanisms were taking place in the device and dominated the transport of electrons at these high temperatures.

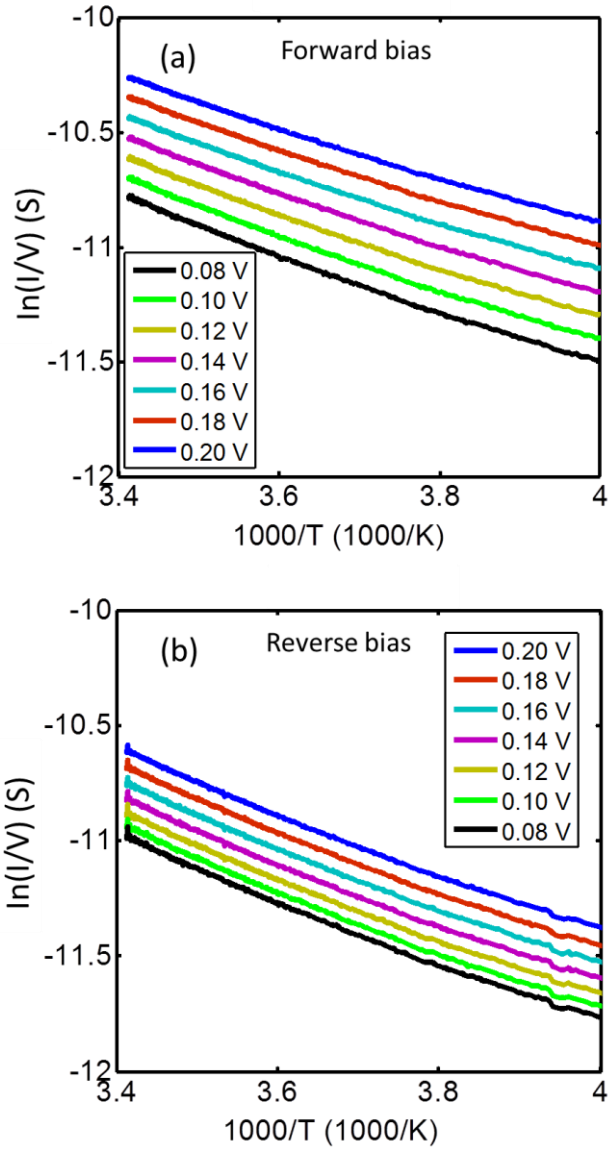

Figure 5.15 – *I-V* characteristics (conductance) vs temperature (250 K to 295 K) plot for the Ti/OTS/Pt structure for a selection of voltages. (a) is the forward bias plots, and (b) the reverse bias plots.

It is speculated that the emission transport mechanisms occurring in the device at higher temperatures was a combination of Schottky emission and Poole-Frenkel emission. As can

be seen in Figure 5.16(a) in the plot of the experimental and theoretical Poole-Frenkel emission expressions, the experimental data shows that there is more than one regime of transport mechanisms occurring in the diode, as the theoretical expression only agrees with certain section of the experimental data.

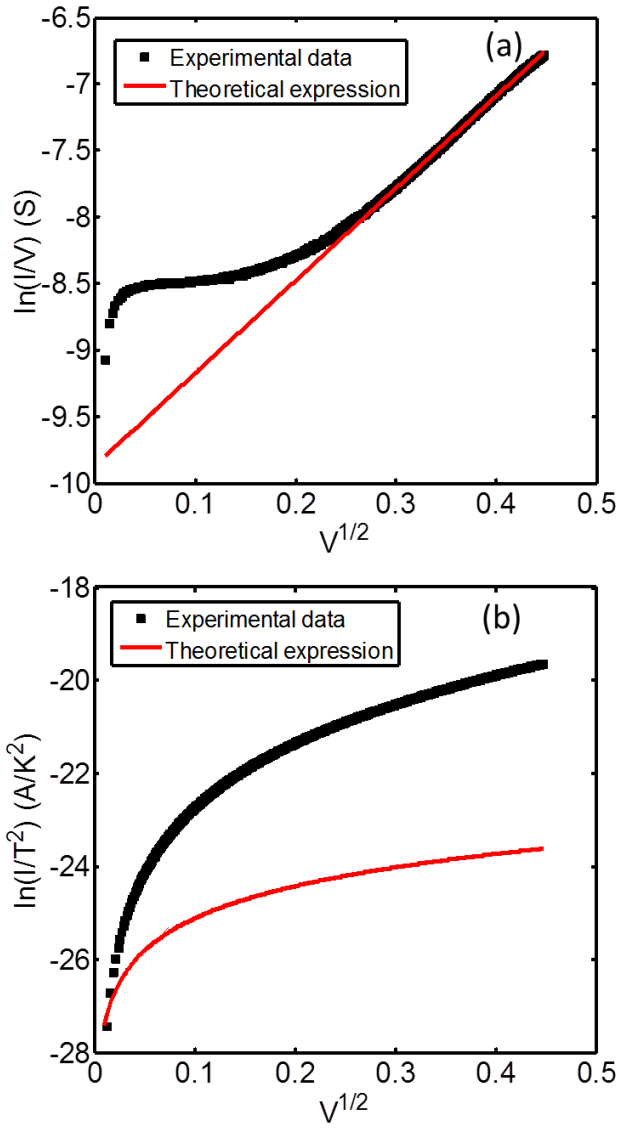

Figure 5.16 – Plot of the experimental data and theoretical expressions for (a) Poole-Frenkel emission, and (b) Schottky emission at a temperature of 295 K.

The plot of the Schottky emission expressions (see 5.16(b)) on the other hand shows a considerable disagreement between the experimental and theoretical data. This means that even though there are more than one transport mechanisms occurring in the diode at

temperatures above 25 K, it is clear that the process is being dominated by Poole-Frenkel emission. The accuracy of the theoretical expressions suffered from an uncertainty in the value of the OTS barrier height, as we don't know the value and it is not available in the available literature; a value of 1.33 eV (which resulted in the closest agreement between the experimental and theoretical expressions) was assumed throughout the investigation. It is speculated that the Poole-Frenkel behaviour arises from trap centres located in the SAM layer. This implies that the transport mechanism that would be occurring in the device for the applications it could be used for (see Chapter 3) will be predominantly emission transport mechanisms, as these applications operates at room temperature or higher.

5.6 Lifetime reliability tests

The diodes' resistance were found to increase with time after fabrication, causing the rectified current to degrade, which is a typical problem associated with MIM junctions [19]. A typical MIM diode current degradation pattern is shown in Figure 5.16 for (both OTS and TiO_x) diodes tested over a period of two weeks.

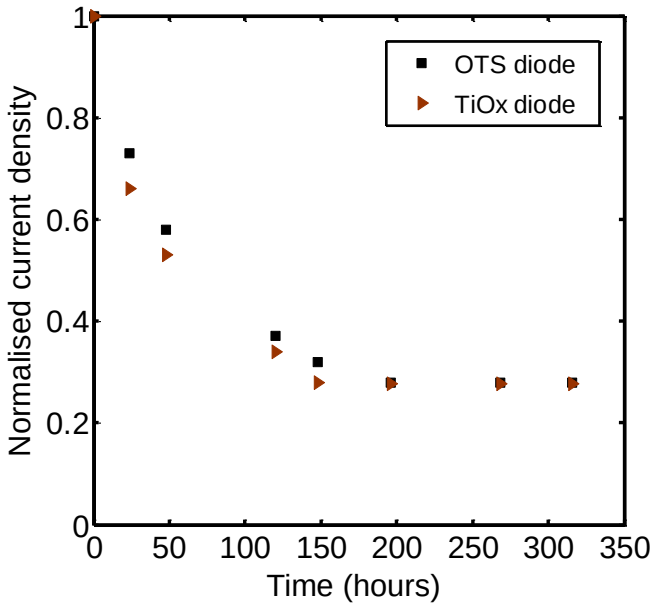

Figure 5.16 – The typical degradation pattern of the rectified normalised current density of $Ti/TiO_x/Pt$ and Ti/OTS/Pt diodes as a function of time after fabrication.

The issue was thought to be caused by the atmosphere (water vapour and oxygen) penetrating through the junction and oxidising the Ti layer. The Ti continues to be oxidised until after the first 150 hours where it self-limits does not get oxidised any further. In order to investigate this hypothesis, the diodes were fabricated on two separate wafers simultaneously under the same conditions. Immediately, after the first round of *J-V* measurements were carried out, one sample was kept in an environment with normal atmospheric conditions, whilst the other was kept in vacuum. *J-V* measurements were then repeated on the two sets of diodes on a daily basis for ten weeks. Figure 5.17 shows the typical current degradation pattern of the diodes kept in normal atmosphere. As can be seen, the rectified current degrades by approximately 75% within the first 180 hours of fabrication, and then stabilises afterwards. But the devices kept in vacuum degraded only by approximately 2% within the first 24 hours and then stabilised thereafter.

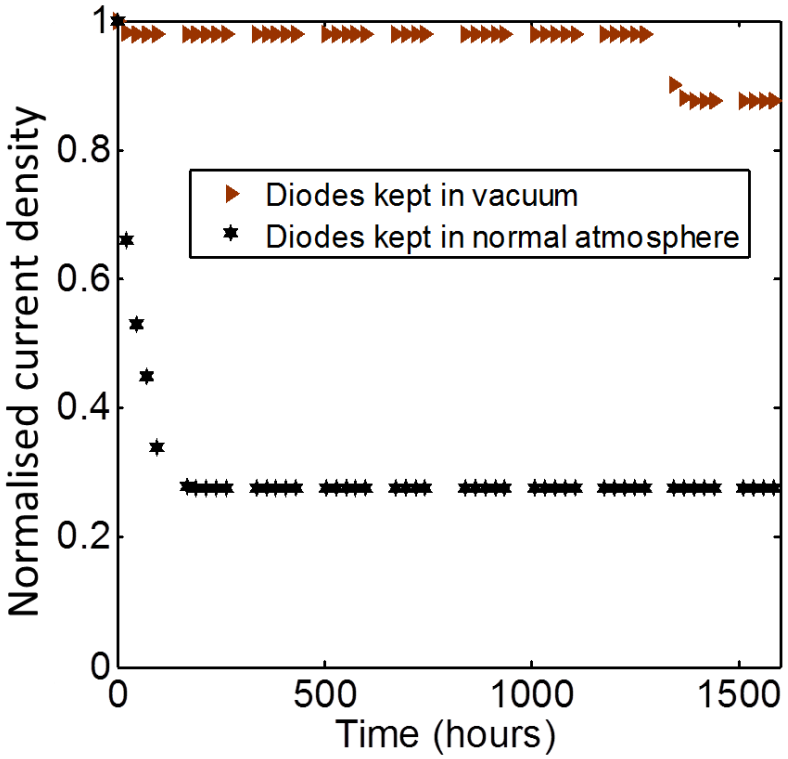

Figure 5.17 – Graph showing the typical degradation of the rectified normalised current density of diodes kept in vacuum and normal atmosphere.

The devices kept in vacuum were then removed from vacuum and kept in an environment with normal atmospheric conditions (temperature of 20 °C and humidity of 48%) for 72 hours and closely monitored. They were found to degrade by approximately 8% within this time period, as can be seen between 1200 and 1400 hours in Figure 5.17. The devices were then placed back in vacuum, and as can be seen (in Figure 5.17) the current stopped degrading and stabilised thereafter again.

A good approach is to develop an encapsulation method, which will insulate the devices from being exposed to the atmosphere.

5.6.1 Encapsulation

An epoxy resin, DELO, often used in the encapsulation of micro electro-mechanical systems (MEMS) was used to encapsulate subsequent freshly fabricated devices. The resin is highly stress-relieving and is flexible [20-21]. As can be seen in Figure 5.18, the diode leads and junctions were completely covered by the resin, exposing only the contact pads to allow electrical measurements to be performed.

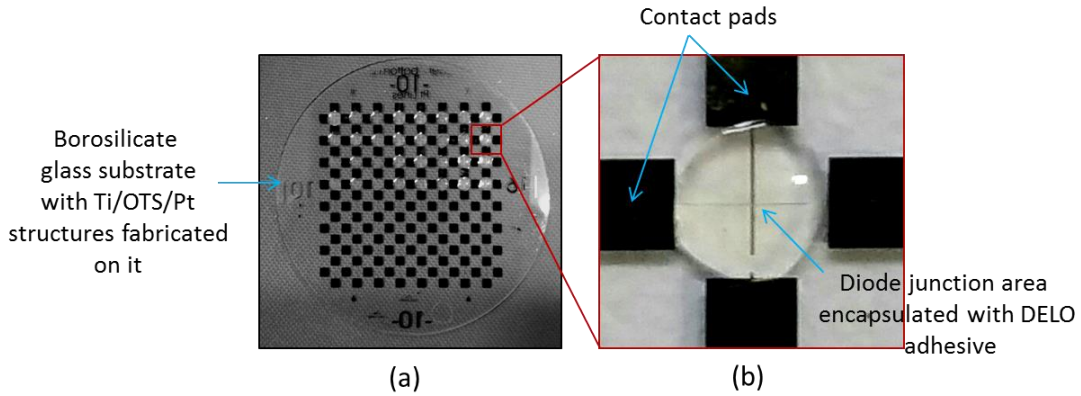

Figure 5.18 – An image of fabricated diodes on a substrate (a). The diodes on the top half of the substrate are encapsulated with DELO resin. (b) A magnified image of an encapsulated MIM junction, with the diode tracks completely covered, exposing just the contact pads to allow electrical measurements to be performed.

In order to be able to perform *J-V* measurements on the diodes (i.e. both the encapsulated devices and those without encapsulation) simultaneously over a long period of time (weeks) in a more controlled manner, a device, which can bias the diodes automatically within specific time intervals, was developed using an mbed microcontroller and a custom designed probe station, which consisted of pogo pins.

As described in Section 4.62, an mbed microcontroller consists of a digital to analogue converter (DAC) as well as multiple analogue to digital converters (ADC). The multiple ADCs allow for multiple diodes to be tested at the same time. A C programming language programme was compiled in the microcontroller, which allows the mbed to generate a sinusoidal voltage, which is then used as the diodes' bias voltage. A series resistor 10 to 15 times larger than the resistance of the diodes was connected between the diode and the generated sinusoidal voltage by the mbed in order to reduce the voltage to approximately ±0.25 V, values that the diodes are able to safely operate in without becoming irreversibly damaged. Buffers were then connected at all the mbed outputs to prevent loading. The mbed is powered using the computer USB port, and generates the sinusoidal waveform automatically based on the program, biasing the diodes (hence current stressing the diodes) periodically and storing the *I-V* characteristics data for further analysis. Figure 5.19 shows the schematic diagram of the developed mbed based biasing device.

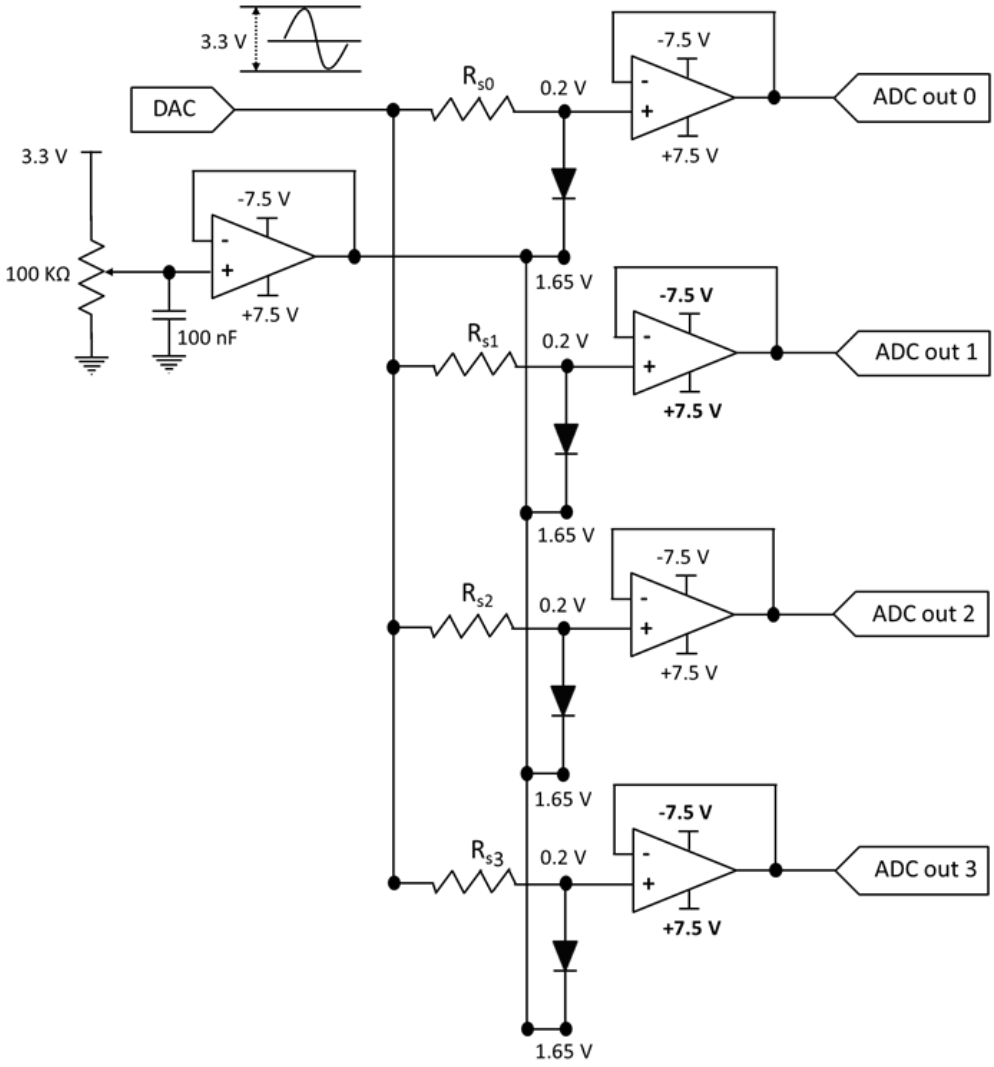

Figure 5.19 – Schematic diagram of the developed mbed based device for automatically biasing and measuring the *I-V* characteristics of multiple diodes simultaneously.

The biasing device was used to measure the *I-V* characteristics of the diodes once hourly, continuously for three weeks, and stores the raw data for every measurement. The retrieved raw *I-V* characteristics data for the diodes without encapsulation and the encapsulated diodes were plotted in Figure 5.20(a) and 20(b) respectively, with each graph containing 504 *I-V* curves (a curve per hour for 21 days). As can be seen on Figure 5.20(a), between the first and last *I-V* measurements the diodes without encapsulation degraded by approximately 80%.

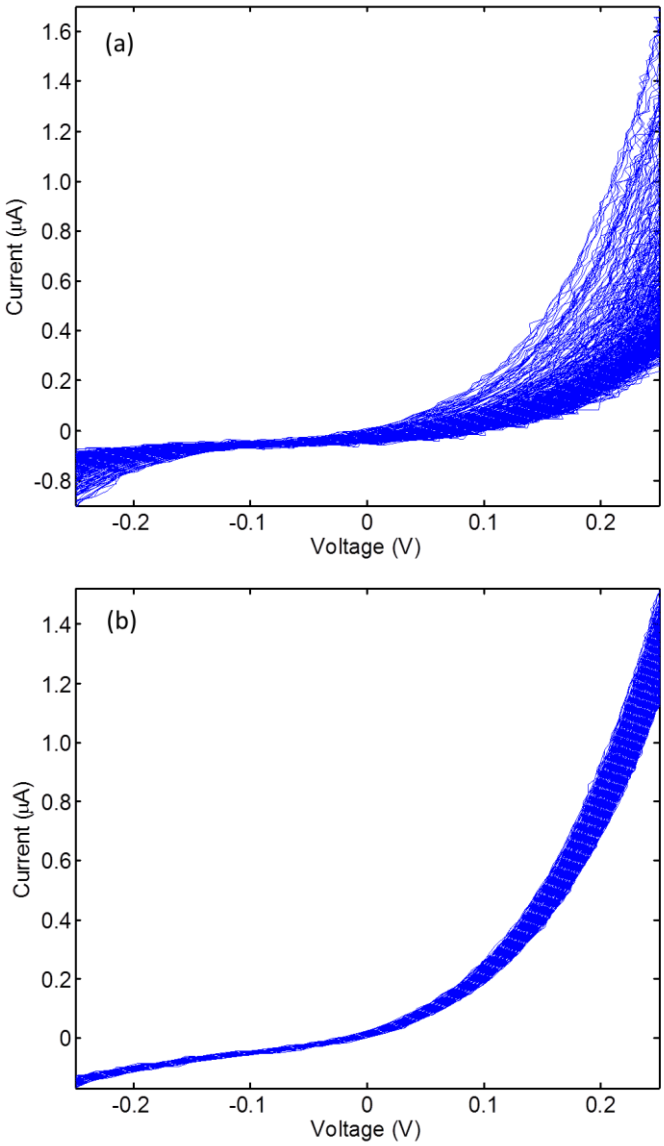

Figure 5.20 – Plot of the *I-V* characteristics of the diodes without encapsulation (a), and (b) encapsulated diodes, with each graph containing 504 *I-V* curves.

The gaps seen in between the *I-V* curves for the diode without encapsulation in Figure 5.20(a) early on in the measurements confirmed that the diode's current degrades rapidly in the first few days and then stabilises thereafter, which was consistent with the initial tests performed to determine the nature of the current degradation with time (shown in Figure 5.17). Conversely, the current of the encapsulated diode (as can be seen in Figure 5.20(b)) degraded only by approximately 25% within the entire period of time the

measurements lasted. The approximately 25% degradation in the encapsulated diode is largely attributed to the diode being current stressed during the measurements.

From the results obtained, just like the devices kept in vacuum (Figure 5.17), only an insignificant amount of current degradation has occurred in the encapsulated devices (Figure 5.20(b)), showing that the encapsulation method was effective.

5.6.2 Summary of lifetime measurement and encapsulation

It has been established that the MIM diode is affected by the atmosphere, resulting in degraded rectified current. The effect of the atmosphere on the diodes was significantly reduced by encapsulating the diode with an epoxy resin. Also, using an automated measurement setup demonstrates a new experimental and electrical measurement procedure on MIM diodes.

5.7 High temperature reliability measurement

5.7.1 Reliability test for OTS layer

Temperature reliability test was performed on the fabricated OTS diodes using a Rapid Thermal Annealer (RTA). The devices were exposed to various different temperatures inside the RTA chamber in vacuum (in order to prevent any form of oxidation taking place) and *J-V* tested after each run to determine how the OTS insulating layers are being affected by increasing temperature. The experiment showed that the OTS layer remained unaffected by temperature up to approximately 450 °C. As the temperature increases higher than 450 °C, the OTS layer started to degrade significantly. This was confirmed by the diode's typical zero bias curvature coefficient, which reduces correspondingly as the temperature increases, as shown in Figure 5.21. The OTS diodes are more robust at high temperature compared to a typical Ti/TiOx/Pt diode which starts to degrade at

approximately 200 °C [22]. This is significant in thermal energy harvesting applications, where the diode may be exposed to high temperature environments.

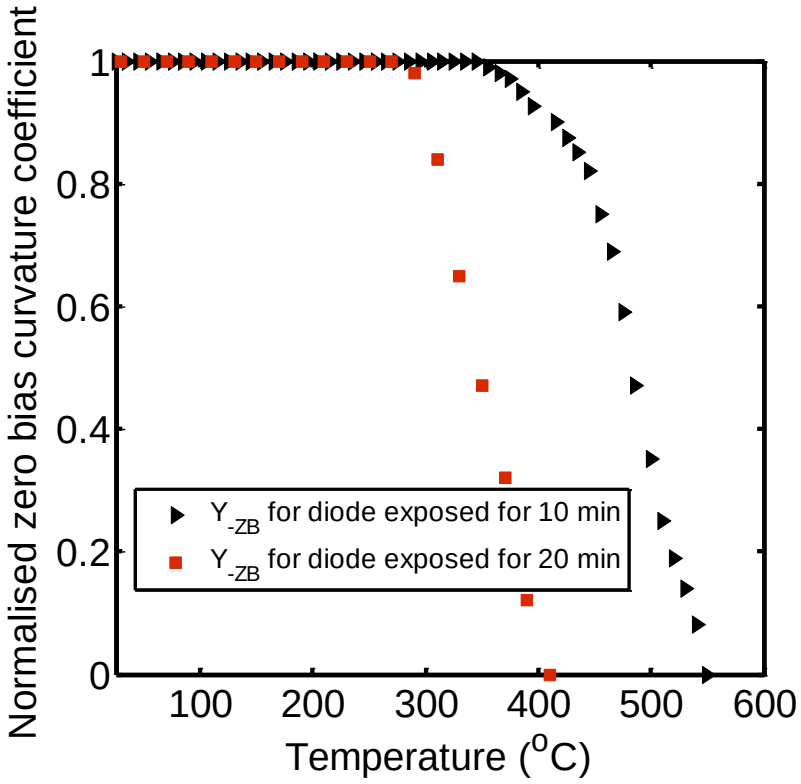

Figure 5.21 – Plot of normalised zero bias curvature coefficient as a function of temperature, from a Ti/OTS/Pt diode exposed to the various different temperatures for 10 and 20 minutes before taking measurements.

The diodes were subjected to a range of temperatures for 10 minutes each run before measurements were performed. Further investigation revealed that the OTS layers, as expected, start to degrade at a faster rate as the diodes were exposed to the heat for a longer period of time compared to when exposed for shorter period of time as shown in Figure 5.21.

Table 5.1 shows a summary of the results for the high temperature reliability tests performed on the OTS diode.

Table 5.1 – Summary of values obtained from high temperature reliability tests on OTS diode

Diode insulating layer	Period of time diode was exposed to various temperatures (Minutes)	Temperature at which insulating layer starts to degrade (^{o}C)	Temperature at which diode is completely irreversibly damaged (^{o}C)
OTS	10	~450	~550
OTS	20	~300	~400

5.8 Summary

Low-cost MIM diodes with an OTS layer as an ultrathin insulator have been produced successfully. DC and RF analysis showed that the diodes have strong nonlinear *J-V* characteristics with a typical zero-bias curvature coefficient of approximately 5.4 V^{-1} and voltage responsivity of 1.9 kV/W at a frequency of 1 GHz. The electrical results were found to be uniform and consistent between different diodes, as well as repeatable. It was found that electron tunneling was the dominant transport mechanism occurring in the diode for temperature of 2.5 K up to approximately 25 K, while emission transport mechanisms dominated the transport of electron from a temperature of approximately 25 K up to room temperature. The Ti/OTS/Pt diodes were found to be unaffected by temperature up to approximately 450 °C, compared to a typical Ti/TiOx/Pt diode, which starts to degrade at approximately 200 °C. This is significant in thermal energy harvesting applications, where the diodes may be exposed to high temperature environments. An encapsulation method to prevent MIM diodes current degradation due to the atmosphere has also been developed. The process developed for fabricating these diodes is very cost effective, and can potentially be employed in the roll-to-roll commercial production of MIM diodes on flexible substrates.

References

[1] E. W. Cowell III, N. Alimardani, C. C. Knutson, J. F. Conley Jr., D. A. Keszler, B. J. Gibbons, and J. F. Wager*, "Advancing MIM Electronics: Amorphous Metal Electrodes", *Adv. Mater*. Vol. 23, pp. 74–78, (2011).

[2] L. E. Dodd, A. J. Gallant, and D. Wood, "Ti-TiO_x-Pt Metal-Oxide-Metal Diodes Fabricated via a Simple Oxidation Technique", *MRS Proceedings*, Vol. 1415, pp. 1-4, (2012).

[3] L. E. Dodd, A. J. Gallant, and D. Wood, "Controlled Reactive Ion Etching and Plasma Regrowth of Titanium Oxides of Known Thickness for Production of Metal-Oxide-Metal Diodes", *IET Micro and Nano Letters*, Vol. 8, No. 8, pp. 476-478, (2013).

[4] L. E. Dodd, "Fabrication Optimization of Metal-Oxide-Metal Diodes", *PhD thesis*, pp 127-132, http://etheses.dur.ac.uk/9474/1/Linzi_Dodd_d51hqe_thesis.pdf?, Accessed online: 12 December 2015.

[5] H. Klauk, U. Zschieschang, J. Pflaum, and M. Halik, "Ultralow-Power Organic Complementary Circuits" *Nature* 445, 745-748, (2007).

[6] S. Rena, S. Yanga, Y. Zhaob, J. Zhoua, T. Xua and W. Liu, "Friction and Wear Studies of Octadecyltrichlorosilane SAM on Silicon", *Tribology Letters*, Vol. 13, Issue 4, pp 233-239, (2002).

[7] K. H. Cha, and D. E. Kim, "Investigation of the Tribological Behavior of Octadecyltrichlorosilane Deposited on Silicon" *Wear*, Vol. 251, Issues 1–12, pp 1169–1176, (2001).

[8] Y. Liu, L. K. Wolf, and M. C. Messmer, "A Study of Alkyl Chain Conformational Changes in Self-Assembled n-Octadecyltrichlorosilane Monolayers on Fused Silica Surfaces", *Langmuir,* Vol. 17 Issue 14, pp 4329–4335, (2001).

[9] P. Fontaine, D. Goguenheim, D. Deresmes, and D. Vuillaume, "Octadecyltrichloro-Silane Monolayers as Ultrathin Gate Insulating Films in Metal-Insulator-Semiconductor Devices", *Appl. Phys. Lett*. 62, 2256 (1993).

[10] Y. Wang and M. Lieberman, "Growth of Ultrasmooth Octadecyltrichlorosilane Self-Assembled Monolayers on SiO_2", *Langmuir*, Vol. 19 (4), pp 1159–1167, (2003).

[11] M. H. Jung and H. S. Choi, "Characterization of Octadecyltrichlorosilane Self Assembled Monolayers on Silicon (100) Surface", *Korean J. Chem. Eng*., 26(6), pp. 1778-1784, (2009).

[12] S. Kim, H. Sohn, J. H. Boo and J Lee, "Significantly Improved Stability of N-Octadecyltrichlorosilane Self-Assembled Monolayer by Plasma Pretreatment on Mica", *Thin Solid Films* Vol. 516, pp. 940–947, (2008).

[13] A. Kaur, X. Yang, and P. Chahal, "Study of Microwave Circuits Based on Metal-Insulator-Metal (MIM) Diodes on Flex Substrates", *Electron. Comp. Technol. Conf.* pp. 2168-2174, (2014).

[14] B. Tiwari, J. A. Bean, G. Szakmany, G. H. Bernstein, P. Fay and W. Porod, "Controlled Etching and Regrowth of Tunnel Oxide for Antenna-Coupled Metal-Oxide-Metal Diodes", *J. Vac. Sci. Technol.* Vol. 27, pp. 2153-2160, (2009).

[15] K. Choi, F. Yesilkoy, G. Ryu, S. H. Cho, N.l Goldsman, M. Dagenais, and M. Peckerar, "A Focused Asymmetric Metal–Insulator–Metal Tunneling Diode: Fabrication, DC Characteristics and RF Rectification Analysis," *IEEE Trans. Electron Devices*, Vol. 58, No. 10, pp. 3519-3528, (2011).

[16] W.F. Brinkman, R. C. Dynes and J.M. Rowell, "Tunneling Conductance of Asymmetrical Barriers," *Journal of Applied Physics*, vol. 41, no. 5, pp. 1915– 1921, (1970).

[17] J. L. Hesler and T. W. Crowe, “NEP and Responsivity of THz Zero-Bias Schottky Diode Detectors”, *32nd Int. Conf. Infrared Millimeter Waves (IRMMW),* pp. 844 – 845pp, (2007).

[18] D. Vuillaume, P. Fontaine, J. Collet, D. Deresmes, M. Garet, and F. Rondelez, “Alkyl-Trichlorosilane Monolayer as Ultra-Thin Insulating Film for Silicon MIS Devices”, *Microelectro. Eng.* Vol. 22, No. 1-4, pp. 101-104, (1993).

[19] K. Choi, F. Yesilkoy, G. Ryu, S. H. Cho, N.l Goldsman, M. Dagenais, and M. Peckerar, “A Focused Asymmetric Metal–Insulator–Metal Tunneling Diode: Fabrication, DC Characteristics and RF Rectification Analysis,” *IEEE Trans. Electron Devices*, Vol. 58, No. 10, pp. 3519-3528, (2011).

[20] R. Zoberbier, M. Hennemeyer, D. Toennies, A. Kraft, M. Eisner, and R. Volkel, “Technology Trends in the Manufacturing and Packaging of Wafer Level Cameras” *Electron. Syst-Integr. Technol. Conf.* pp. 1-5, (2010).

[21] T. Königer, “New MEMS Die Attach Adhesives Combining Maximum Flexibility and Outstanding Dispensability Including Screen Printing” *Eur. Microelectron. Packag. Conf.* pp. 1-6, (2015).

[22] L. E. Dodd, S. A. Shenton, A. J. Gallant, and D. Wood, “Improving Metal-Oxide-Metal (MOM) Diode Performance Via the Optimization of the Oxide Layer”, *J. Electron. Mater.* , Vol. 44, No. 5, pp. 1361-1366, (2015).

Chapter 6

MIM Diodes Fabricated on a Flexible Substrate

6.1 Introduction

In this chapter, the manufacture of Ti/OTS/Pt MIM diodes on a flexible substrate formed using polyimide (PI) is discussed. The PI substrate formation, electrical analysis of the fabricated diodes, which includes asymmetry, *J-V* characteristics, yield and lifetime reliability are all discussed.

6.2 Motivation for OTS producing MIM diodes on a flexible substrate

Since the MIM diodes' insulating layer consisted of OTS, with the deposition process being at low temperature, a roll-to-roll manufacturing process for MIM diodes is highly possible. The MIM structures, if successfully fabricated on flexible substrates, are suitable for applications where a large area and low-cost manufacturing process is of paramount importance, such as radio frequency identification devices (RFID) operating up to 980 MHz [1-4], due to their potential to operate at these high frequencies. While flexible devices such as organic diodes already exist, they are limited by a poor frequency response [5]. The

devices are also suitable for energy recovery based rectennas (if the structure dimensions are optimised) [6-8] that need a flexible substrate, if the operating frequency can be made higher still.

6.3 Polyimide (PI) flexible substrate formation

Polyimide is a high molecular weight and fully aromatic material, which is formed from polyamic acid precursors dissolved in an N-methyl-2-pyrrolidone based solvent carrier. The material is mechanically robust, enabling thin layers to be formed, and can be spin coated in a large area [9].

A 2 inch silicon wafer was used as a carrier for the polyimide substrate. Prior to the polyimide deposition, the silicon wafer was cleaned using a piranha solution (H_2SO_4:H_2O_2), and dried using N_2, followed by a bake at 200 °C for 3 minutes to dehydrate the surface. The polyimide was spin coated on the silicon wafer at 500 rpm for 10 seconds, and then 2000 rpm for 30 seconds, resulting in a 2.5 µm thick substrate. In order to be able to peel the substrate off the silicon carrier wafer without damage, the spin coating process was repeated two further times with a 5 minutes bake at 85 °C between each run, resulting in a total substrate thickness of 7.5 µm. After the final coating, the polyimide was part-cured by baking at 150 °C for 15 minutes, and fully cured in a convection oven at 350 °C with a ramp rate of 2 °C per minute. Higher ramp rates were found to cause bubbles within the polyimide, reducing yield. Figure 6.1 shows a completed flexible PI substrate peeled off the silicon carrier wafer prior to patterning.

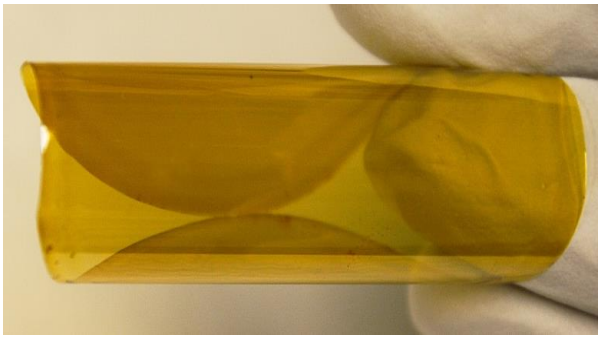

Figure 6.1 – An optical picture of a completed PI flexible substrate prior to patterning.

6.4 Diode fabrication

After spin-coating the PI on the carrier wafer, the MIM structures were produced by depositing approximately 25 nm of titanium by e-beam evaporation. The titanium was then coated with OTS followed by the deposition of a layer of platinum with a thickness of approximately 40 nm by e-beam evaporation, resulting in the Ti/OTS/Pt junctions. The detail fabrication process and OTS deposition can be found in Section 5.3. In order to improve the Ti film adhesion, the PI surface was activated in an O_2 plasma for 1 minute, with a pressure of 150 mT, an O_2 flow rate of 50 sccm, and an RF power of 75 W.

Following the completion of the MIM structures, the PI substrate was peeled off the carrier wafer. Current-voltage (*J*-*V*) characteristics were measured on the devices before (with over 90% device yield) and after peeling off the PI substrate. There was no loss of yield after the peeling process. Figure 6.2 shows a picture of the completed devices and an AFM image of one of structures, where the MIM junction is defined at the cross-over.

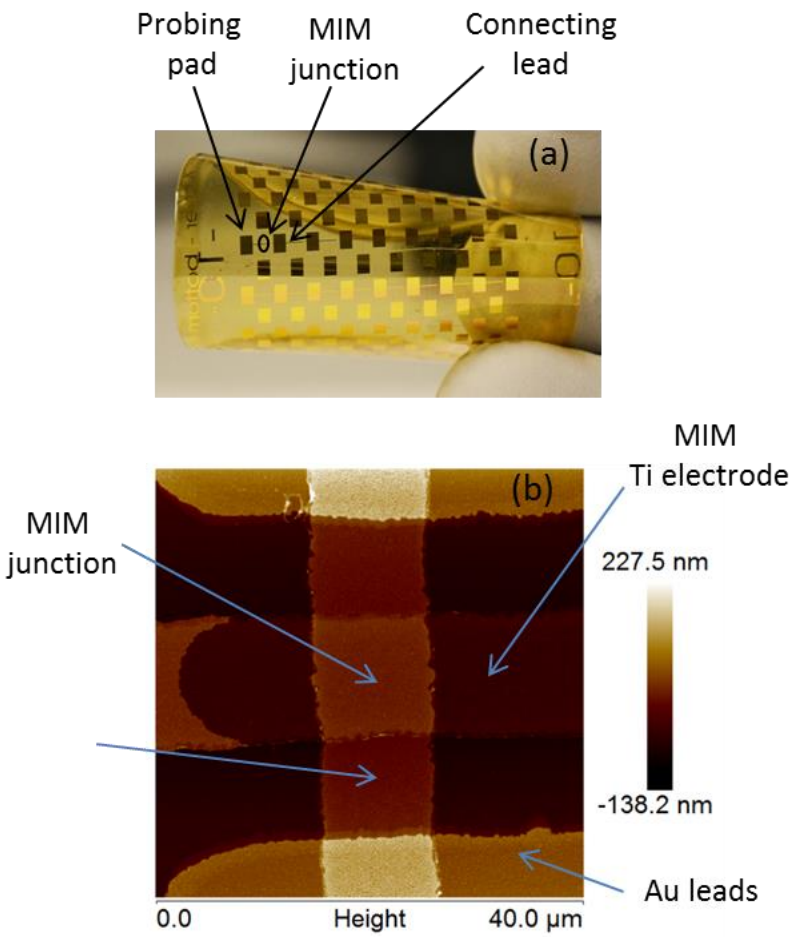

Figure 6.2 – Picture of fabricated Ti/OTS/Pt devices on PI substrate (a), with the devices' connecting leads and probing pads visible, and (b) an AFM image of one of the devices with the crossover at the middle denoting the diode junction.

6.5 Electrical measurements

6.5.1 DC measurements

DC electrical characterisation was carried out on the diodes using a parameter analyser. The diodes were tested over a voltage range of ±0.2 V in order to avoid damaging their junctions, as the devices were found to have an irreversible breakdown voltage of approximately ±0.35 V. A typical *J*-*V* characteristic is plotted in Figure 6.3, showing a strong asymmetry and non-linearity at zero bias.

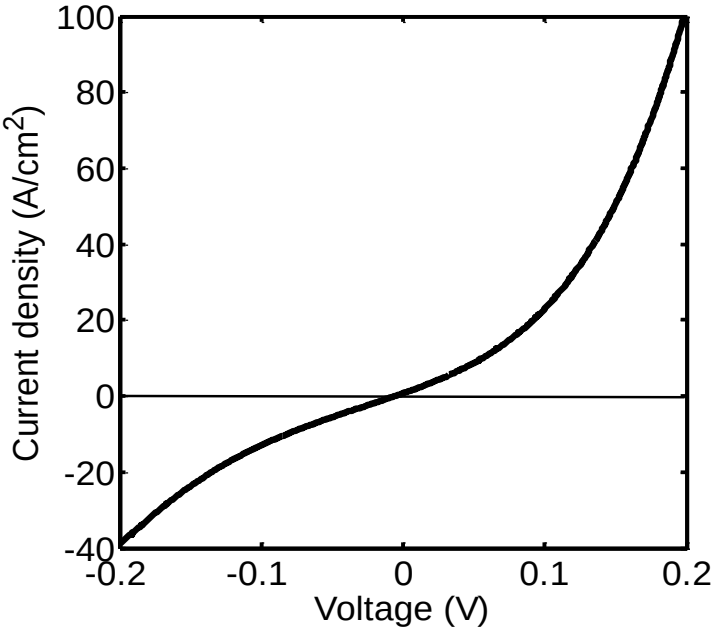

Figure 6.3 – Typical *J-V* characteristics of a fabricated Ti/OTS/Pt MIM diode on a PI flexible substrate.

The zero bias curvature coefficient ($\gamma_{\_ZB}$), as defined by Equation (5.1), was found to be approximately 5.5 V^{-1} (shown in Figure 6.4), which was consistent with the value given in Section 5.4 for these devices fabricated on a rigid borosilicate glass substrate.

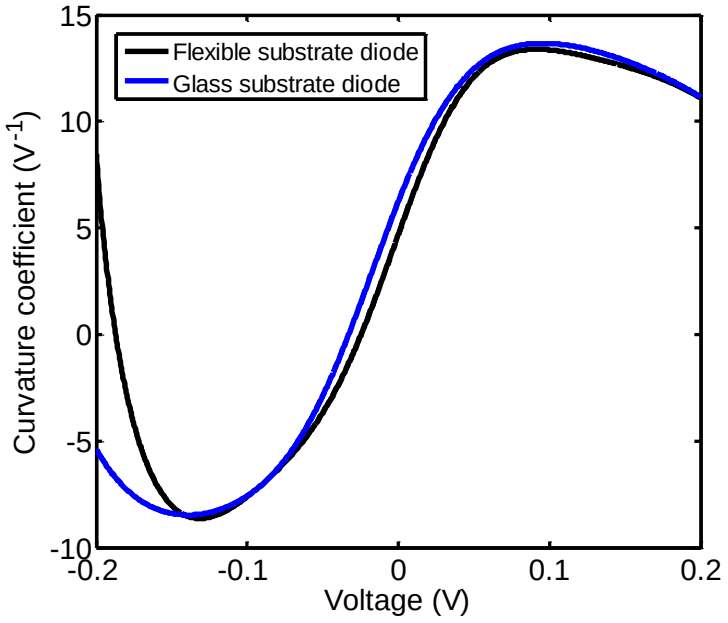

Figure 6.4 – Typical curvature coefficient plot of a fabricated Ti/OTS/Pt MIM diode on glass and PI flexible substrates.

The diode zero bias resistance, calculated by Equation (2.5), was approximately 80 kΩ as shown in Figure 6.5 (a value which was also close to the previous results of these devices fabricated on a glass substrate in Section 5.4), a value much smaller than those available in the literature (typically in the MΩ regime [10]). The relatively small resistance associated with the diode is attributed to the very thin OTS layer (~2 nm), as the resistance of MIM structures is significantly influenced by the thickness of the dielectric layer [11].

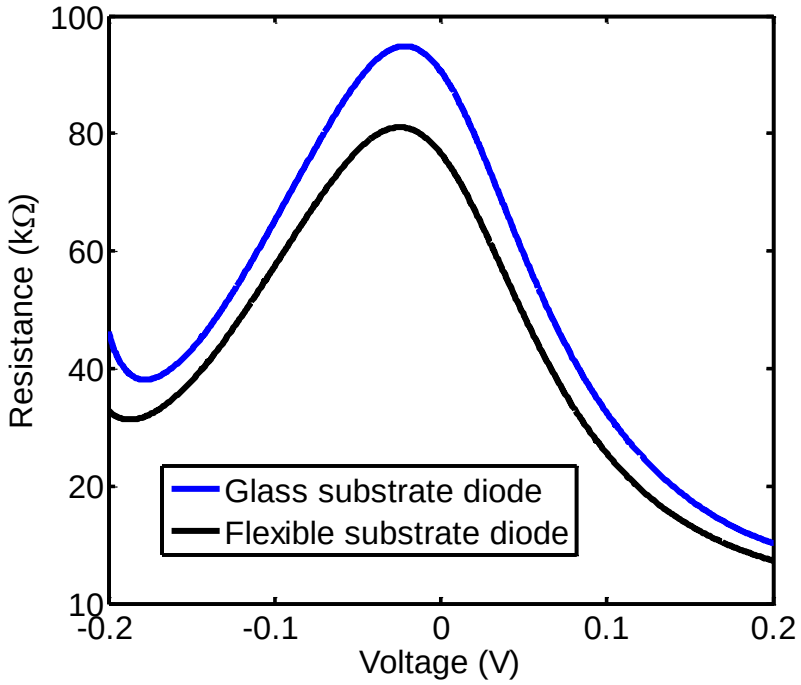

Figure 6.5 – Typical resistance plot of a fabricated Ti/OTS/Pt MIM diode on glass and PI flexible substrates.

The lower resistance also improves the match of an antenna (with impedance typically of the order of 100 Ω) to the diodes, thus improving the overall efficiency where the diode is used as rectifier in rectenna devices.

6.5.2 RF measurements

To enable RF testing, ten diodes were embedded within a coplanar waveguide as in Section 5.4.2, with a characteristic impedance of 50 Ω, to minimise unwanted reflections

from the layout as well as to reduce radiation losses. RF measurements on the diodes were carried out from 1 MHz to 3 GHz. The input RF power was compensated at different frequencies to account for the measured losses in the cables, probes and coplanar waveguides. The rectified output voltage was measured for RF input powers in the range 20 to 500 nW (-47 to -33 dBm). There was no light dependency observed on the device during the measurements, which were carried out at room temperature.

Figure 6.6 shows a typical rectified output voltage of the diode as a function of RF power fed into the coplanar waveguide at a frequency of 1 GHz. Figure 6.7 shows the frequency response of the diode, measured up to 3 GHz with a constant input RF power of approximately 100 nW (-40 dBm).

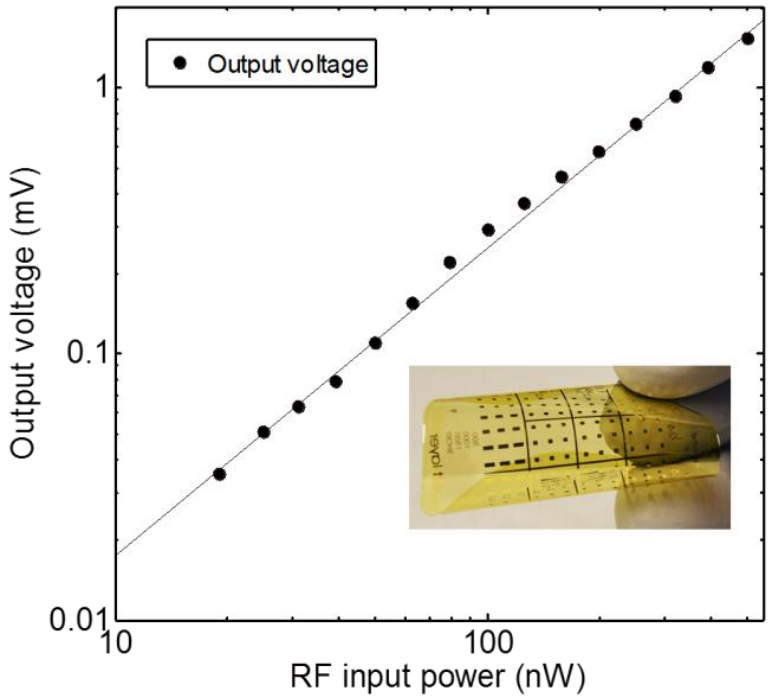

Figure 6.6 – A plot of the device rectified voltage as a function of input RF power at a frequency of 1 GHz. In the inset is a picture of the devices fabricated on a PI substrate. The devices were embedded within coplanar waveguides to enable RF tests without significant radiation losses.

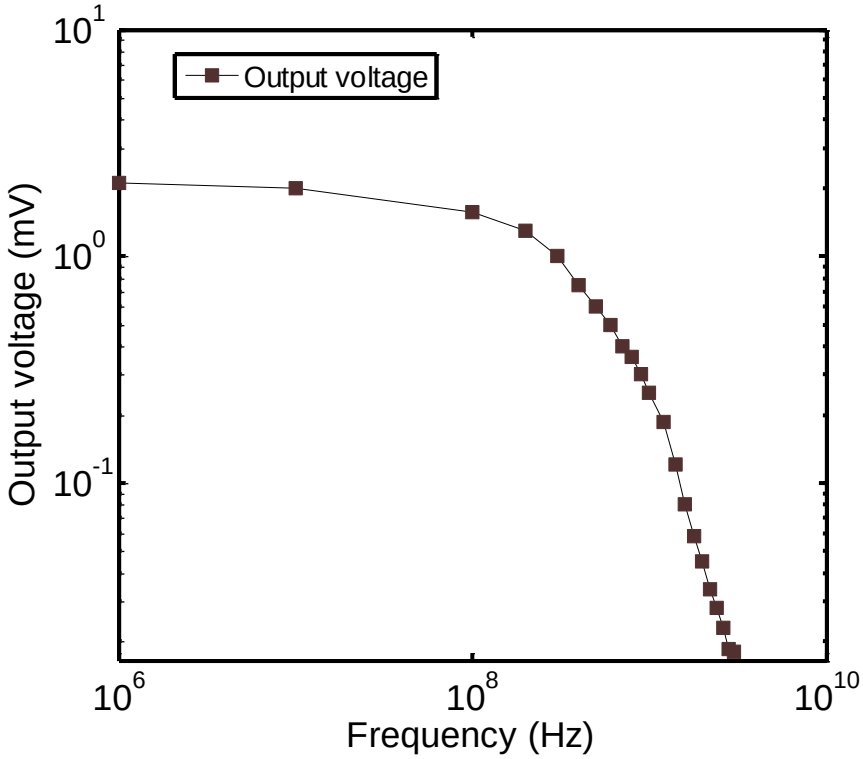

Figure 6.7 – A plot of the device rectified voltage as a function of the frequency. The input power was kept constant at approximately 100 nW (-40 dBm).

The value of the diode voltage responsivity R_V was determined by a linear fitting of the rectified output voltage as a function of the input RF power, shown in Figure 6.6, and had an absolute value of approximately 3 kV/W at a frequency of 1 GHz.

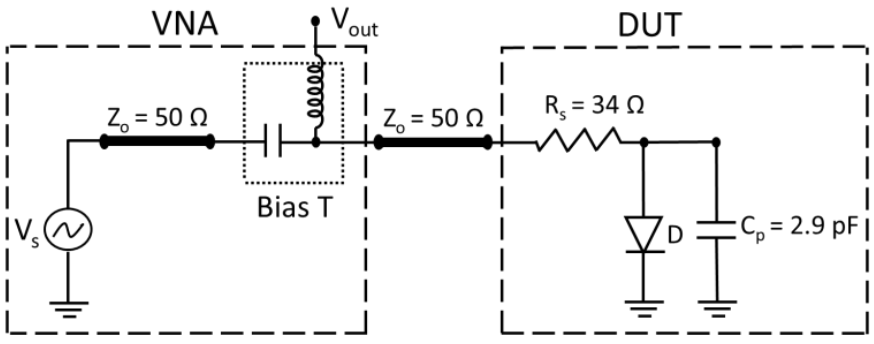

Figure 6.8 – Equivalent high-frequency circuit diagram for the diode characterisation. The series resistance R_s and parallel capacitance C_p were extracted by measuring and fitting the reflection coefficient (S_{11}) as a function of the frequency.

The parameters which influenced the diode response were determined by measuring the reflection coefficient of the whole structure, $s_{11,}$ as a function of the operating frequency using a vector network analyzer (VNA) and converting it into the input impedance Z_{IN}, defined by Equation (5.4). Z_{IN} was then fitted numerically as in Section 5.4.2, resulting in a series resistance R_S = 34 Ω and a parallel capacitance C_P = 2.9 pF as shown in Figure 6.8. The parallel capacitance here was also much higher than expected from the capacitor associated with the diode junction. This was attributed to a fringe effect of the diode leads. An electromagnetic simulation (using Agilent Advance Design System) of the whole structure confirmed this, which is in good agreement with the measured data. A comparison between the simulated input impedance of the device layout and measured device impedance is shown in Figure 6.9.

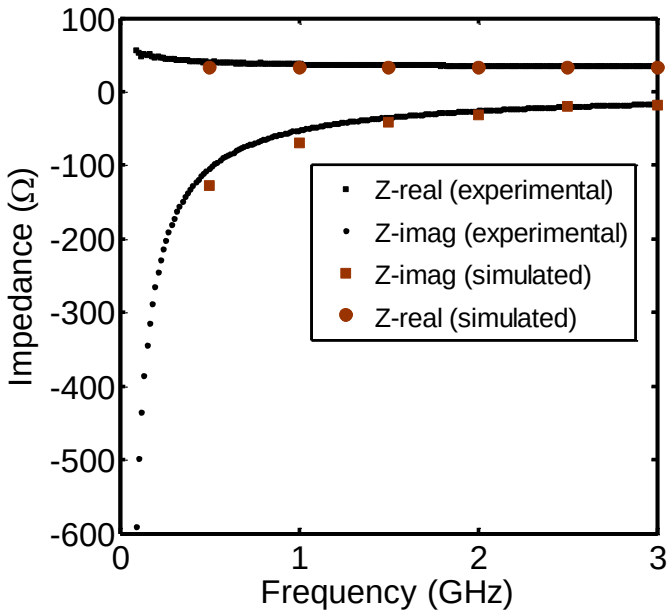

Figure 6.9 – Measured and simulated diode impedance as a function of the frequency.

6.6 Lifetime reliability tests

Similar to Section 5.6 where the diodes were fabricated on a borosilicate glass substrate, the diodes' zero-bias resistance was found to increase with time after fabrication, causing

the rectified current to degrade. This confirmed that this issue of the MIM diodes' rectified current degrading with time after fabrication is not associated with the substrate used. The same encapsulation method used in Section 5.6 was used here. MIM diodes were fabricated on two separate wafers simultaneously under the same process conditions. Immediately after carrying out the first set of *J-V* measurements, one wafer was kept in an environment with normal atmospheric conditions (temperature of 20 °C and humidity of 48%), whilst the other was kept in vacuum. *J-V* measurements were then repeated on the two sets of diodes daily for 3 weeks. Figure 6.10 shows the typical current degradation pattern of the diodes kept in normal atmosphere. As can be seen, the rectified current degrades by approximately 75% within the first 150 hours following fabrication, and then stabilises afterwards. The devices kept in vacuum degraded only by approximately 2% within the first 24 hours and remained stable thereafter.

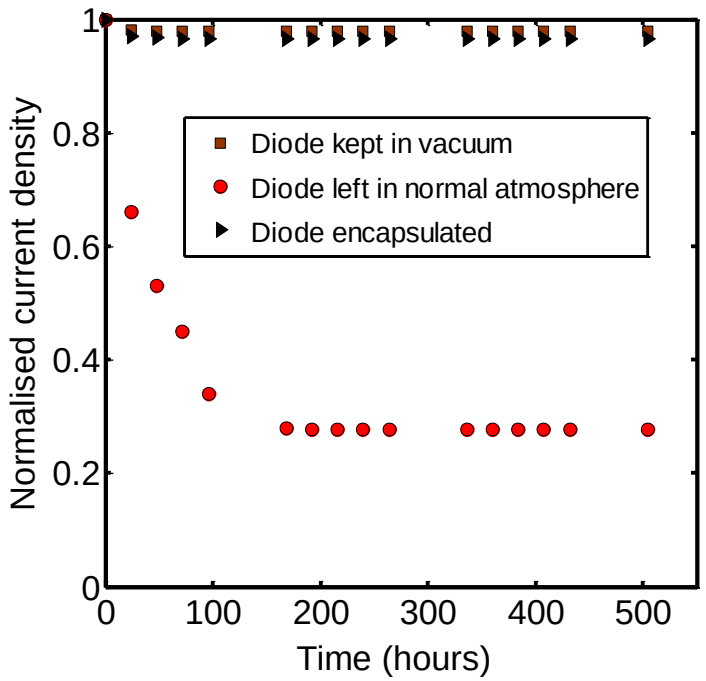

Figure 6.10 – Graph showing the typical normalised current density of Ti/OTS/Pt diode kept in vacuum, in normal atmosphere, and encapsulated.

The results for the encapsulated devices are plotted in Figure 6.10. Similar to the devices kept in vacuum, only a negligible amount of current degradation (approximately 2%) was observed, showing that the encapsulation method was very effective.

The device was tested while the substrate was wrapped on a disc shape metal rod as shown in Figure 6.11(a). The device curvature coefficient was unaffected with a curvature (bend) radius of 4 cm, but started to degrade as the curvature radius decreased, as can be seen in Figure 6.11(b). Although the device electrical parameters degrade while curved at these radii, the amount of degradation was insignificant.

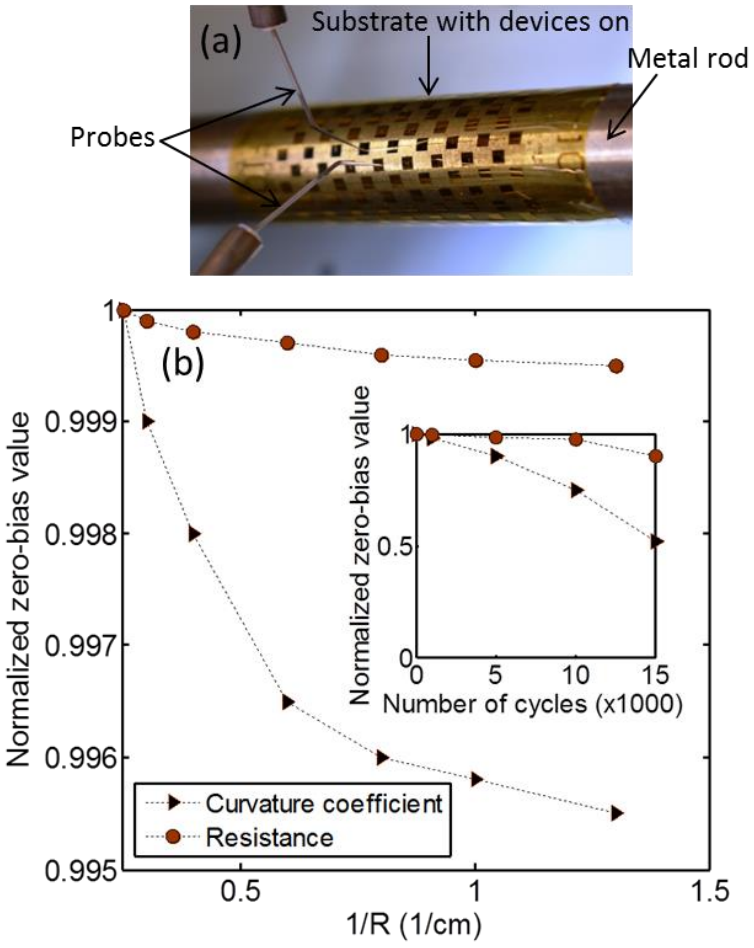

Figure 6.11 – Picture of fabricated Ti/OTS/Pt devices on a flexible substrate wrapped on a disc shape metal rod (a), and (b) plot of zero-bias resistance and curvature coefficient of the device as a function of substrate curvature. In the inset of (b) is the plot of zero-bias resistance and curvature coefficient as a function of bend cycles.

To further stress the device, the substrate was bent repeatedly using a cam shaft with a 1.5 cm stroke, driven by a motor with a constant speed of 60 rpm. The bend cycle was repeated 15000 times, with tests performed in between. In the inset of Figure 6.11(b) is the plot of the device curvature coefficient and resistance as a function of the number of bend cycles. As can be seen, the device curvature coefficient had degraded by approximately 50% on completion of the test. This means that the device in its current form is more suitable for applications where constant and heavy vibration is not present.

6.7 Summary

The fabrication and tests of MIM diodes on flexible substrate has been discussed, with over 90% device yield consistently achieved. DC and AC analysis showed that the diodes have strong non-linear *J-V* characteristics with consistent typical zero-bias curvature coefficient ($\gamma_{\_ZB}$) of ~5.5 V^{-1} and a voltage responsivity of 3.1 kV/W at a 1 GHz operating frequency. The devices were encapsulated with an epoxy resin; a process which effectively prevented the diodes' rectified current from degrading. The diodes' insulating layer consisted of OTS, with the deposition process being at low temperature. The diodes show no significant degradation in performance when the substrate is stressed in a one-off bending experiment, although extensive testing does produce some loss in quality. The fabrication details presented here show that a roll-to-roll manufacturing process for MIM diodes is highly possible. The MIM structures are suitable for applications such as 13.6 MHz and 980 MHz RFID tags. Also, as the devices have been successfully fabricated on 7.5 μm thick polyimide, the possibility for energy recovery based rectennas that need a flexible substrate has been demonstrated.

References

[1] V. Subramanian, P. C. Chang, J. B. Lee, S. E. Molesa, and S. K. Volkman, "Printed Organic Transistors for Ultra-Low-Cost RFID Applications," *IEEE Trans. Compon. Packag. Technol,* Vol. 28, No. 4, pp. 1318–1330, (2005).

[2] R. A. Potyrailo, W. G. Morris, T. Sivavec, H. W. Tomlinson, S. Klensmeden, and K. Lindh, "RFID Sensors based on Ubiquitous Passive 13.56-MHz RFID Tags and Complex Impedance Detection," *Wireless Commun. Mob. Comput.* Vol. 9, Issue 10, pp. 1318–1330, (2009).

[3] H. T. Hsu, and T. J. Huang, "A Koch-Shaped Log-Periodic Dipole Array (LPDA) Antenna for Universal Ultra-High-Frequency (UHF) Radio Frequency Identification (RFID) Handheld Reader," *IEEE Trans. Antennas Propag.* , Vol. 61, No. 9, pp. 4852- 4856, (2013).

[4] K. Myny, S. Steudel, P. Vicca, J. Genoe, and P. Heremans, "An Integrated Double Half-Wave Organic Schottky Diode Rectifier on Foil Operating at 13.56 MHz," *Appl. Phys. Lett.* Vol. 93, 093305 (2008).

[5] S. Steudel, S. D. Vusser, K. Myny, M. Lenes, J. Genoe, and P. Heremans, "Comparison of Organic Diode Structures Regarding High-Frequency Rectification Behavior in Radio-Frequency Identification Tags," *J. Applied Phys*. Vol. 99, 114519, pp. 1-7, (2006).

[6] Y. Pan, C. V. Powell, A. M. Song, and C. Balocco, "Micro Rectennas: Brownian Ratchets for Thermal-Energy Harvesting", *Appl. Phys. Lett*. Vol. 105, 253901, (2014).

[7] M. N. Gadalla, M. Abdel-Rahman, and A. Shamim, “Design, Optimization and Fabrication of a 28.3 THz Nano-Rectenna for Infrared Detection and Rectification,” *Sci. Rep.* Vol. 4, No. 4270, pp. 1-8, (2014).

[8] M. R. Abdel-Rahman, B. Monacelli, A. R. Weeks, G. Zummo, and G. D. Boreman, “Design, Fabrication, and Characterization of Antenna-Coupled Metal-Oxide-Metal Diodes for Dual-Band Detection”, *Opt. Eng.* Vol. 44(6), pp. 066401, (2005).

[9] HD MicroSystems. Product Bulletin: PI-2600 Series—Low Stress Polyimides, (2009).

[10] K. Choi, F. Yesilkoy, G. Ryu, S. H. Cho, N.l Goldsman, M. Dagenais, and M. Peckerar, “A Focused Asymmetric Metal–Insulator–Metal Tunneling Diode: Fabrication, DC Characteristics and RF Rectification Analysis,” *IEEE Trans. Electron Devices*, Vol. 58, No. 10, pp. 3519-3528, (2011).

[11] M. N. Gadalla, M. Abdel-Rahman, and A. Shamim, “Design, Optimization and Fabrication of a 28.3 THz Nano-Rectenna for Infrared Detection and Rectification,” *Sci. Rep.* Vol. 4, No. 4270, pp. 1-8, (2014).

Chapter 7

Diodes Fabricated Using Atomic Layer Deposition

7.1 Introduction

Atomic Layer Deposition (ALD) is a method used in the deposition of conformal thin films (up to a few nm) of a range of materials, including metals [1-5] and metal-oxides [6-9], with an accurate number of atomic layers. This deposition technique has been explored in this project in order to determine a method that presents the best options in terms of electrical results, cost of production, and production process.

This chapter discusses the fabrication and DC electrical characterisation (including current density, curvature coefficient, current ratio, and yield) of MIM diodes with an Al_2O_3 insulator layer, deposited using ALD. The diodes' DC electrical results are compared with those of the OTS insulator diodes, fabricated previously.

7.2 Al_2O_3 deposition process

As mentioned in Section 4.4.3, the ALD deposition process involves sequential alternating pulses of gaseous chemical precursors reacting with the surface of a sample to synthesise a material. The individual gas-surface reactions (also known as half-reactions [10]) make up only a part of the material's synthesis. The detail of a typical ALD deposition process is

discussed in Section 4.4.3; with Figure 7.1 (not drawn to scale) illustrating the basic process.

In this project, Al_2O_3 was deposited onto titanium by exposing it to alternate pulses of trimethylaluminium (TMA) and H_2O vapour precursors. Firstly, nitrogen gas (N_2) was used to purge the ALD chamber of any residual precursor molecules which might have remained from previous depositions. During the TMA exposure (the first half-reaction), the TMA chemisorbed on the titanium surface, leaving the surface covered with a layer of $AlCH_3$ after the reaction had completed. Any remnant of the TMA was purged out of the chamber. The other precursor (H_2O vapour) was then pulsed. The H_2O vapour reacted with the surface $–CH_3$ forming CH_4 as a reaction byproduct and resulted in a thin Al_2O_3 film being formed. The cycle was then further repeated 22 times, with a synthesis of 2 nm thick Al_2O_3 being deposited. Table 7.1 shows a summary of the parameters and their values, used for the process.

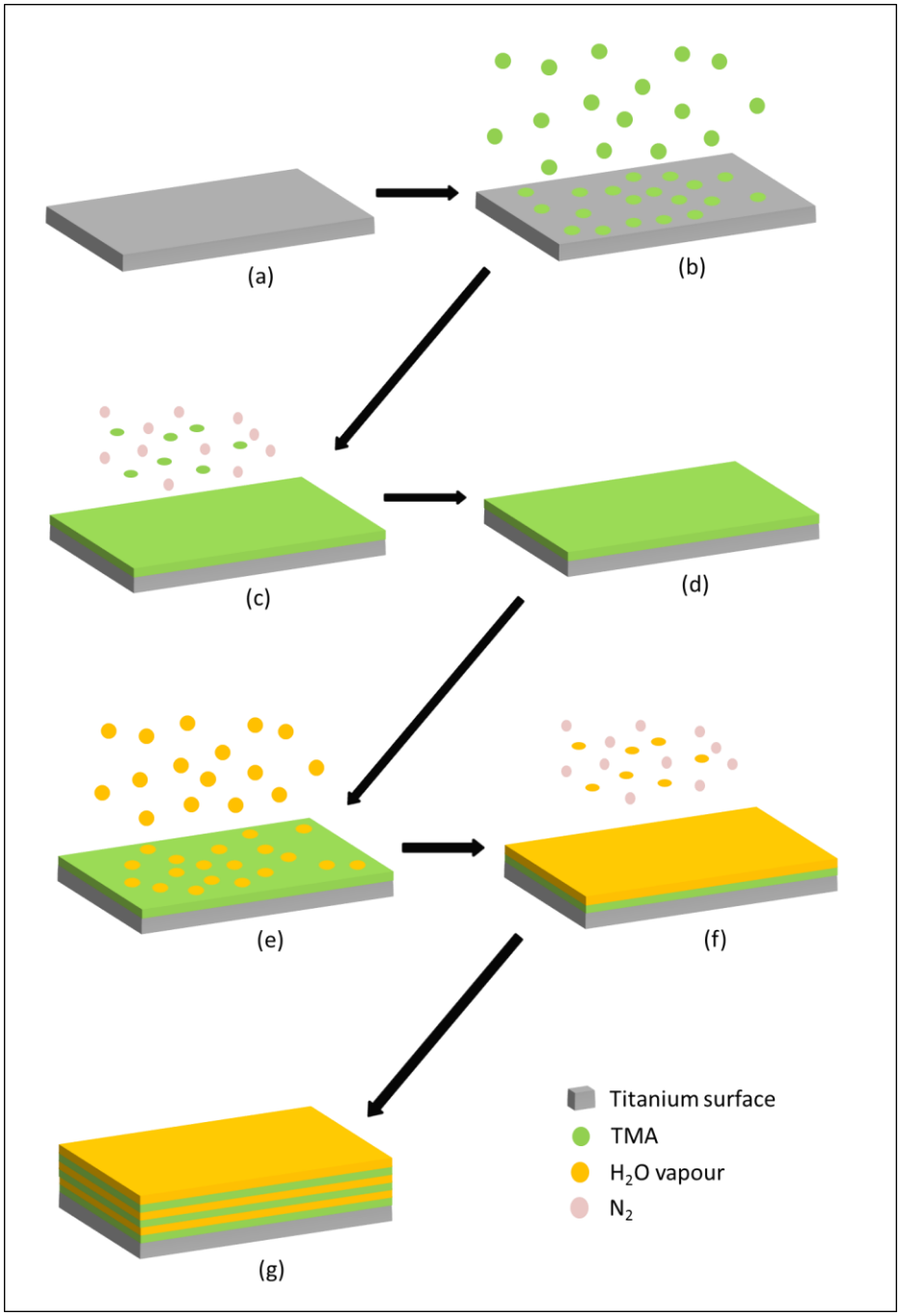

Figure 7.1 – Schematic diagram of the ALD deposition process for an Al_2O_3 film on a titanium surface. Substrate coated with titanium was placed in the ALD chamber (a), and (b) the first precursor (TMA) was pulsed, with the first half-reaction taking place. After the reaction had completed, residues of the TMA were purged out of the chamber using N_2 (c). (d) Is the titanium surface covered with ($AlCH_3$) the product of the first half-reaction. The second precursor (H_2O vapour) was pulsed, with the second half-reaction taking place (e). Residues of the H_2O vapour were purged using N_2 (f), and (g) a thin Al_2O_3 film is formed. The cycle was further repeated 22 times, with a 2 nm thick Al_2O_3 layer being achieved.

Table 7.1 – The process parameters used for depositing 2 nm of an Al_2O_3 layer

Parameter	Value
N_2 flow rate	20 sccm
Stabilise	5400 sec
Pulse 1 (TMA)	0.015 sec
Wait	5 sec
Pulse 2 (H_2O vapour)	0.015 sec
Wait	5 sec
Repeat cycle	22 cycles

7.3 Ti/ Al_2O_3/Pt diode fabrication

Figure 7.2 (not drawn to scale) shows the basic fabrication process of the diode (as in Section 5.3 with the major difference being the use of Al_2O_3 rather than OTS). A bilayer of approximately 25 nm of titanium coated with 100 nm of gold was deposited by e-beam evaporation and lift-off (a). After a further photolithographic step, gold was removed by an iodine/potassium-iodide (4:1:8 KI:I_2:H_2O) wet etch, leaving small regions of titanium exposed (b-c). After removing the photoresist (d) the exposed titanium was coated with a 2 nm thick Al_2O_3 (e) using the technique described in Section 7.2 above. After a further photolithographic step, a thin layer of platinum with a thickness of 40 nm was evaporated on the sample and patterned via lift-off in the unexposed regions, resulting in the definition of small Ti/Al_2O_3/Pt junctions (g-h). The addition of leads and bonding pads concluded the MIM diodes fabrication.

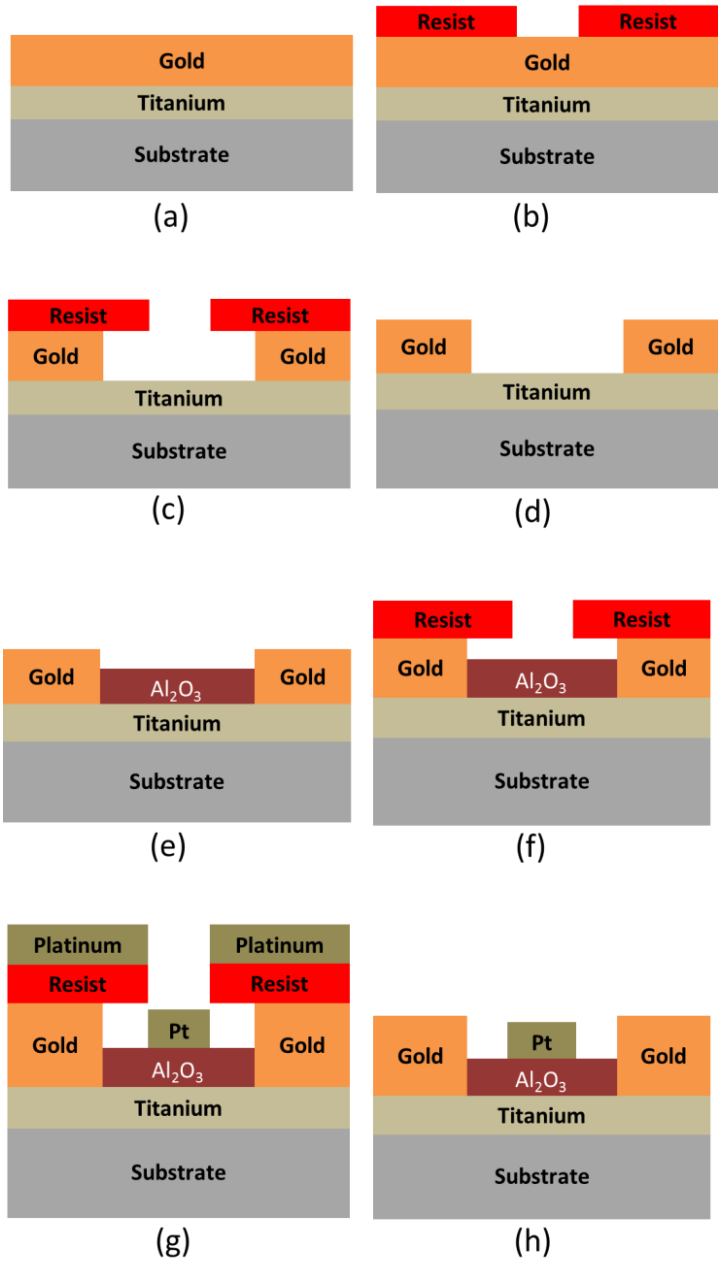

Figure 7.2 – The Ti/Al_2O_3/Pt MIM diode fabrication process. (a) Ti/Au bilayer on borosilicate glass. Photolithographic patterning (b) followed by Au wet etching (c). Photoresist stripping (d) and Al_2O_3 deposition (e). Photolithographic patterning (f), Pt deposition (g) and lift-off (h).

A sketch of the device cross-section and an AFM image of a fabricated structure can be seen in Figure 7.3. The crossover at the middle of the image defines the MIM junction. The feature size of the fabricated junction is approximately 10 µm x 10 µm.

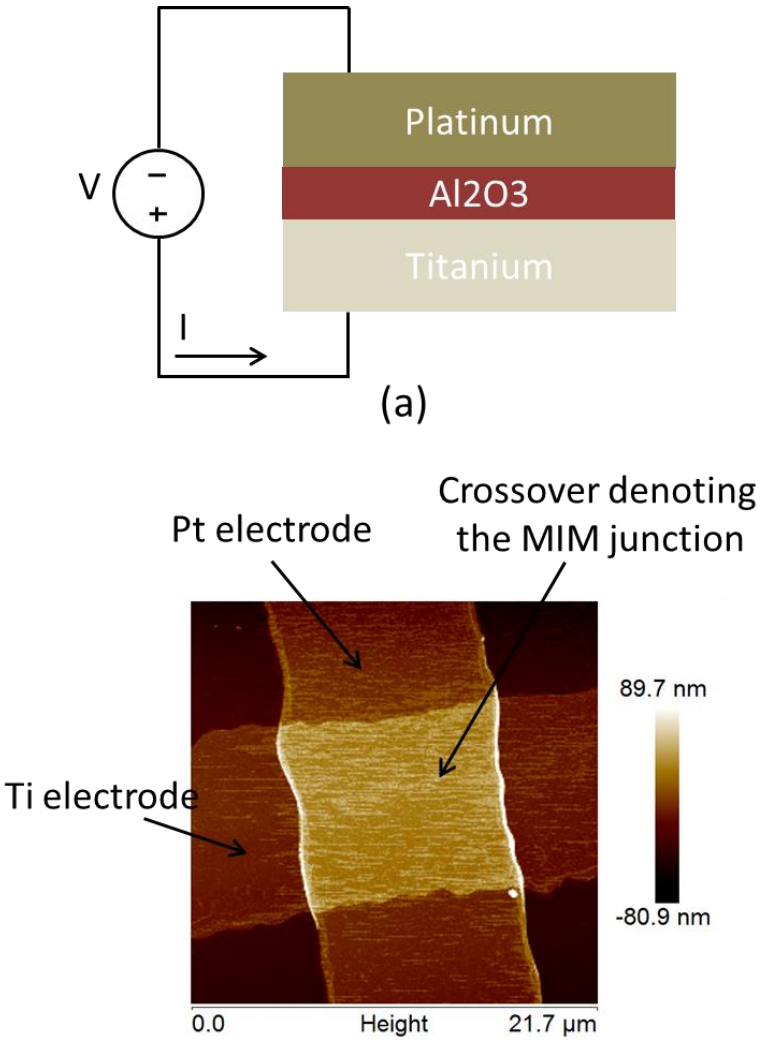

Figure 7.3 – A sketch of the device cross-section (a) and an AFM image of a fabricated Ti/Al_2O_3/Pt structure (b). The titanium and platinum electrodes act as the anode and the cathode, respectively.

7.4 DC characterisation of the Ti/ Al_2O_3/Pt diode

The devices were electrically characterised using a parameter analyser. The diodes were tested over a voltage range of ±0.2 V. A typical *J-V* characteristic of the diode is plotted in Figure 7.4, showing a strong non-linearity at zero bias (i.e. $V = 0$ V). The zero bias curvature coefficient (γ_{ZB}) shown in Figure 7.5, defined by Equation (5.1), was found to be approximately 5.4 V^{-1}. Also, the typical device resistance as a function of voltage can be seen in Figure 7.6, with the zero bias resistance (R_0) being approximately 118 kΩ.

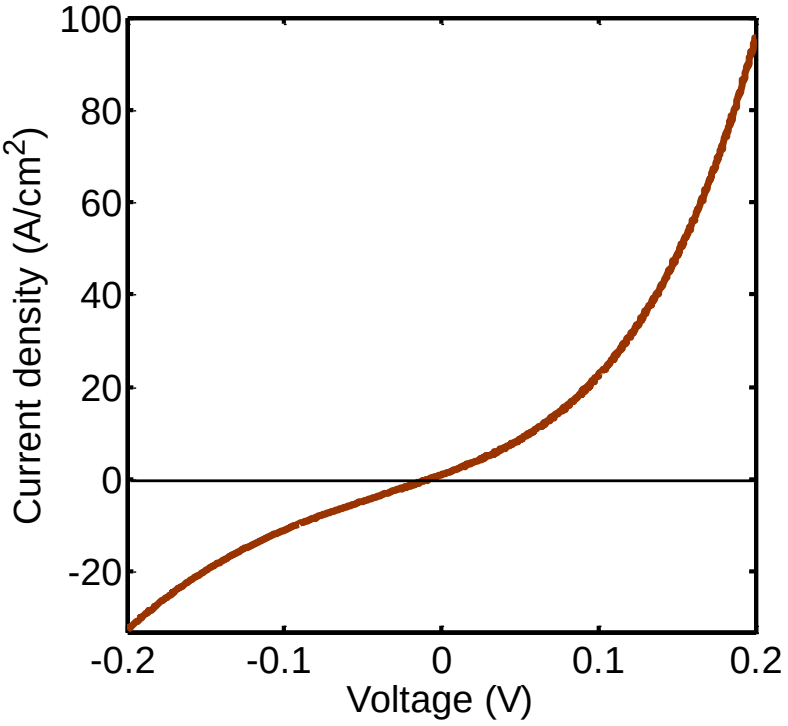

Figure 7.4 – Typical *J-V* characteristics of a fabricated Ti/Al_2O_3/Pt MIM diode.

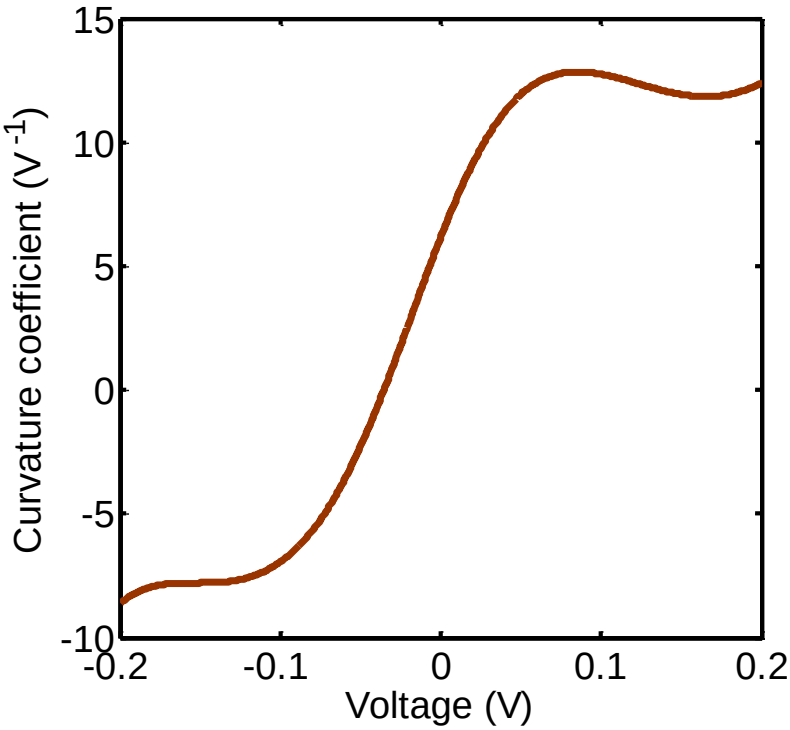

Figure 7.5 – Typical curvature coefficient plot of a fabricated Ti/Al_2O_3/Pt MIM diode.

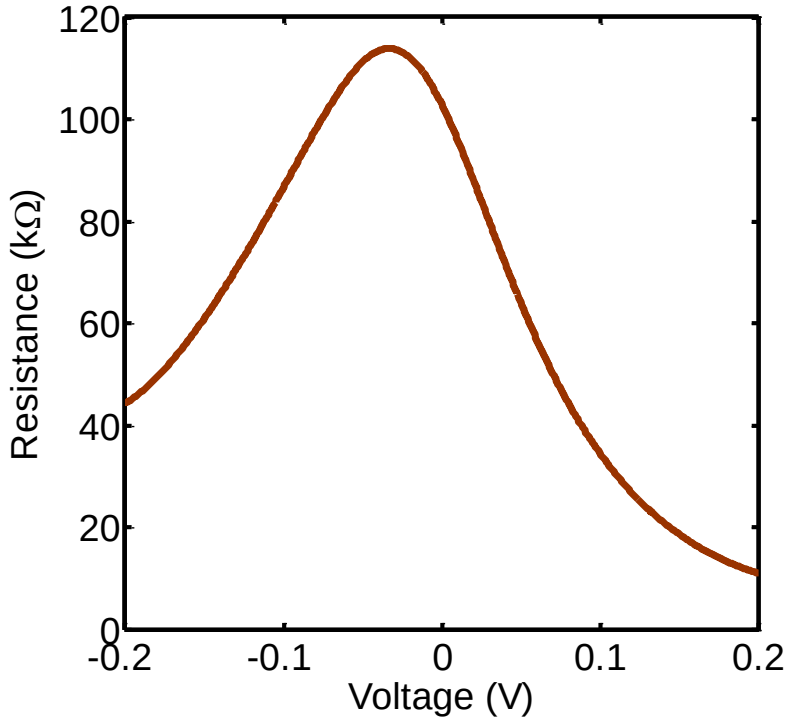

Figure 7.6 – Typical resistance plot of a fabricated Ti/Al_2O_3/Pt MIM diode.

7.5 Comparison between the DC electrical parameters of Al_2O_3 insulator diode and OTS insulator diode

The DC electrical parameters of diodes fabricated using Al_2O_3 and OTS (both approximately 2 nm thick) as insulators are compared. Shown in Figure 7.7 are the typical *J-V* characteristics of the two different diodes. As can be seen, the two *J-V* characteristics look similar; however, the Al_2O_3 insulator diode has a slightly higher current density than the OTS insulator diode. The Al_2O_3 insulator diodes were also found to have more uniform electrical results than the OTS insulator diodes. This is shown in Table 7.2. The table shows the average values of zero-bias curvature coefficient ($\gamma_{\_ZB}$), current ratio, current density and yield (with the standard deviation in those results shown in brackets). The more uniform results associated with the Al_2O_3 diodes may be due to the high-precision of the Al_2O_3 film deposition performed using the ALD.

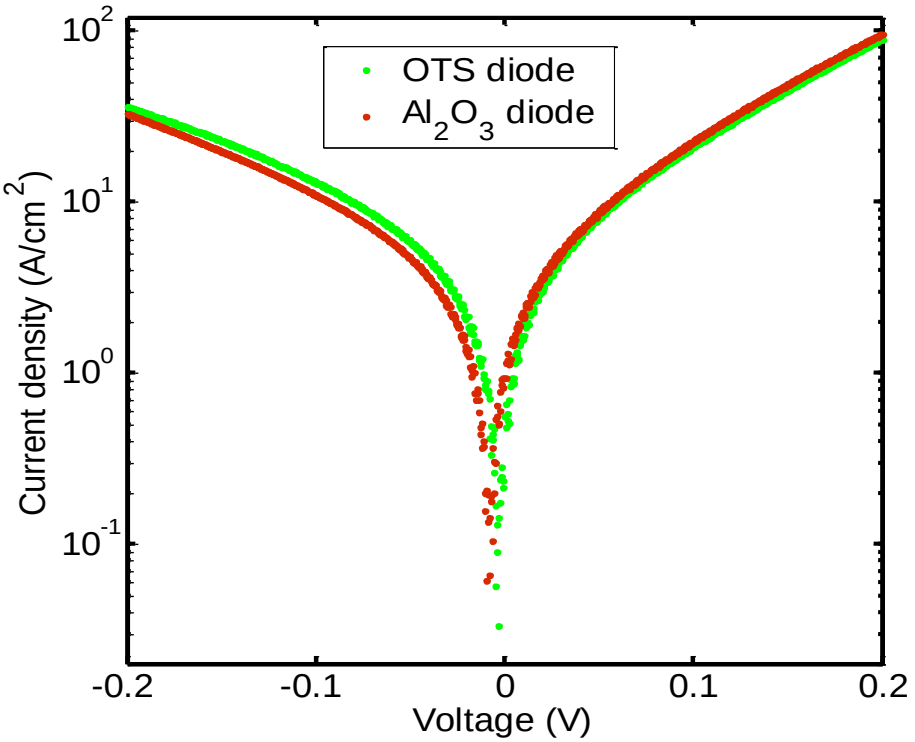

Figure 7.7 – Typical *J-V* characteristics of OTS and Al_2O_3 insulator diodes.

Table 7.1 – Comparison of electrical parameters between OTS and Al_2O_3 diodes.

Diode	Highest CC_{ZB} (V^{-1})	Average CC_{ZB} (V^{-1})	Average current ratio	Average current density (A/cm^2)	Yield (%)
2 nm OTS insulator diode	5.6	3.5 (0.4)	1.8 (0.5)	49	78
2 nm Al_2O_3 insulator (ALD) diode	5.9	3.8 (0.2)	1.8 (0.3)	56	82

7.6 Summary

The fabrication and DC electrical characterisation of MIM diodes with Al_2O_3 insulator, deposited using the ALD, has been discussed. The DC analysis showed that the devices have strong non-linear *J-V* characteristics with typical zero-bias curvature coefficient ($\gamma_{\_ZB}$) and

resistance of approximately 5.4 V^{-1} and 118 kΩ respectively. A comparison between the DC electrical results of the fabricated Al_2O_3 insulator diodes and OTS insulator diodes was made, with the Al_2O_3 insulator diodes producing slightly better results, in terms of current density, zero-bias curvature coefficient, and yield. Although the DC results of the Al_2O_3 insulator diodes here are slightly better, the advantages the OTS insulator diodes presents, such as low-cost of production, low-temperature manufacturing process and the possibility it presents for the roll-to-roll volume manufacture of MIM devices, cannot be ignored. It will be a case of making a choice between a slight improvement in electrical parameters and a huge difference in production cost, with the OTS device being the cheaper one.

References

[1] M. B. E. Griffiths, P. J. Pallister, D. J. Mandia, and S. T. Barry, “Atomic Layer Deposition of Gold Metal”, *Chem. Mater.,* Vol. 28, pp 44−46, (2016).

[2] P. G. Gordon, A. Kurek, and S. T. Barry, “Trends in Copper Precursor Development for CVD and ALD Applications”, *ECS J. Solid State Sci. Technol.,* vol. 4, Issue 1, pp 3188-3197, (2015).

[3] A. Niskanen, T. Hatanpaä, K. Arstila, M. Leskelä¨, and M. Ritala, “Radical-Enhanced Atomic Layer Deposition of Silver Thin Films Using Phosphine-Adducted Silver Carboxylates”. *Chem. Vap. Deposition,* Vol. 13, pp. 408−413, (2007).

[4] P. R. Chalker, S. Romani, P. A. Marshall, M. J. Rosseinsky, S. Rushworth, and P. A. Williams, “Liquid Injection Atomic Layer Deposition of Silver Nanoparticles”, *Nanotechnol.* Vol. 21, 405602, pp 1-7, (2010).

[5] M. Kariniemi, J. Niinisto, T. Hatanpaa, M. Kemell, T. Sajavaara, M. Ritala, and M. Leskela, “Plasma-Enhanced Atomic Layer Deposition of Silver Thin Films”, *Chem. Mater.* Vol. 23, pp 2901–2907, (2011).

[6] X. Wang, S. M. Tabakman, and H. Dai, “Atomic Layer Deposition of Metal Oxides on Pristine and Functionalized Graphene”, *J. Am. Chem. Soc.* Vol. 130, pp 8152–8153, (2008).

[7] D. M. Hausmann, E. Kim, J. Becker, and R. G. Gordon, “Atomic Layer Deposition of Hafnium and Zirconium Oxides Using Metal Amide Precursors”, *Chem. Mater.* Vol 14, pp 4350-4358, (2002).

[8] K. Kukli, M. Ritala, M. Schuisky, M. Leskelä, T. Sajavaara, J.i Keinonen, T. Uustare, and A. Hårsta, “Atomic Layer Deposition of Titanium Oxide from TiI_4 and H_2O_2”, *Chem. Vap. Deposition*, Vol. 6, Issue 6, pp 303-310, (2000).

[10] R. W. Johnson, A. Hultqvist, and S. F. Bent, “A Brief Review of Atomic Layer Deposition: From Fundamentals to Applications”, *Mater. Today*, Vol. 17, Issue 5, pp. 236-245, (2014).

Chapter 8

Rectenna Operation at Microwave and Millimetre Wave Frequencies

8.1 Introduction

This chapter discusses the design and fabrication of an impedance-matching structure to improve efficiency of rectenna devices. The experimental results were supported by numerical simulations, which suggest that the same impedance matching technique can be used for mm-waves and THz radiation.

8.2 Rectenna

A typical rectenna consists of a rectifier coupled to an antenna, and acts to convert electromagnetic radiation to an electrical DC signal [1-6]. Fast rectifiers, such as the Schottky diode [2], the metal-insulator-metal (MIM) diode [1, 3-4], and more recently the self-switching nanodiode [5], are often used in this application due to their ability to operate at frequencies well into the terahertz range. One of the major drawbacks of these devices, however, is the relatively low external conversion efficiency, caused mainly by the mismatch between the impedance of the antenna (typically between 10 to 100 Ω) and that

of the diode, which is typically as high as several kΩ [5-7]. In order to maximise the rectenna efficiency, a network, which can match the impedance of the rectifier to that of the antenna, is required. A basic equivalent circuit diagram of a rectenna with an impedance matching network placed between the antenna and the rectifier can be seen in Figure 3.8 in Section 3.2.3. The conversion efficiency is given as;

$$\eta = \frac{P_{OUT}}{P_{IN}} \tag{8.1}$$

where P_{OUT} is the rectified output power, and P_{IN} is the input power being fed into the rectifier by the antenna.

In this project, a simple and effective technique, consisting of a pair of coplanar strip lines, was used to match the impedance of a typical bow-tie antenna to a rectifier with a zero-bias impedance of several kΩ. The device operates as a high-efficiency rectenna, which can be used in applications where efficient narrow-band operation ranging from microwaves to terahertz is of paramount importance, such as radio frequency identification (RFID) devices and energy harvesting (with optimised dimensions) respectively, as well as to maximise the signal-to-noise ratio in detection and imaging systems. The impedance-matching technique was first modelled via numerical simulations, and then implemented experimentally, with the experimental results confirming the functionality of the model.

8.3 Transmission line

A transmission line can be considered as two conducting wires running parallel to each other, which provides a link between two points where current and voltage changes are transmitted instantaneously [8]. An ideal transmission line performs this function with no loss. This is, however, not possible in practice, as the finite resistance per unit length of the wire used as the line results in power loss when current is flowing through it. The measure

of losses in the lines can be determined from the line wave propagation constant γ_P, expressed as [8-9]:

$$\gamma_P = \alpha + i\beta \tag{8.2}$$

where α is the attenuation constant and β, the propagation velocity. The attenuation constant shows the measure of loss in the line and increases in value with increasing frequency due to dielectric loss and skin effect [10].

The geometry of the line (i.e. the gap between the two parallel lines, and the length and width of the lines) affects its parameters [8, 11], such as the inductance (L) per unit length due to metal wires and the capacitance (C) per unit length due to the coupling between the parallel wires. These in turn affects the line characteristic impedance (Z_0) and wave propagation speed (β).

Consider the infinite transmission line, which is cut and separated at a certain section of the length (*x*) of the line. An open circuit will ensue; in which case the current becomes zero and stays zero at all times since signal can neither be propagated forward nor be absorbed in an open circuit condition. The only possibility is for the signal to be reflected completely. The zero current condition through the open circuit forces the sum of the forward and reflected currents to be zero, as shown in Figure 8.1.

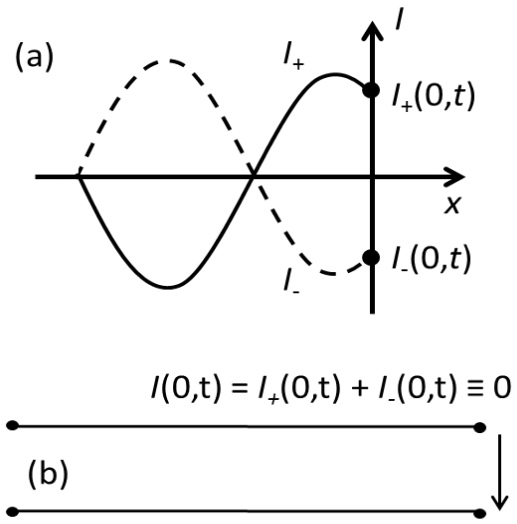

Figure 8.1 – Transmission line terminated on an open circuit. The forward wave (solid line) is completely reflected (dashed line) (a), and (b) the sum of the forward and reflected wave being zero (adapted from [8]).

Similarly, if the line is short circuited at a certain section, the signal will also be completely reflected as power dissipation cannot occur on a short circuit condition. However, things are different if the line is terminated on a load with an impedance (Z_L); if Z_L is not equal to the line characteristic impedance (Z_0) then part of the signal will be reflected and some dissipated on the real part of Z_L.

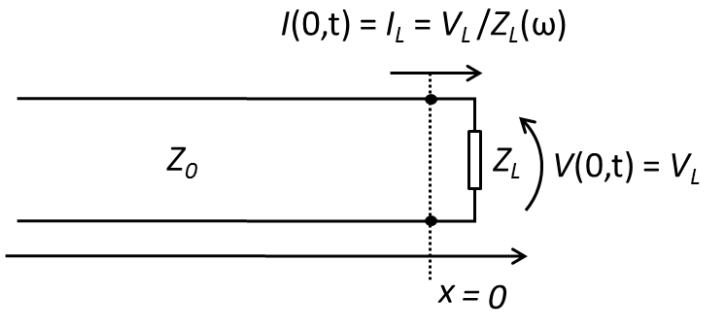

Figure 8.2 – Transmission line terminated on a load with an impedance Z_L (adapted from [8]).

Consider a sinusoidal signal propagating in a line with characteristic impedance (Z_0). If the signal is terminated on the load impedance (Z_L) at $x = 0$, as shown in Figure 8.2, the

overall voltage $V(x,t)$ and current $I(x,t)$ will consist of the sum of forward and reflected waves, expressed as [8]:

$$V(x,t) = V_{+}e^{-ikx}.e^{-i\omega t} + V_{-}e^{ikx}.e^{i\omega t}, \tag{8.3}$$

and

$$I(x,t) = \frac{V_{+}}{Z_0}e^{-ikx}.e^{-i\omega t} - \frac{V_{-}}{Z_0}e^{ikx}.e^{i\omega t} \tag{8.4}$$

respectively.

where $k = \omega/v$ is the phase constant, and x is the line length. At $x = 0$ the ratio between the voltage and the current is set by the load impedance (Z_L), expressed as [8, 12]:

$$\frac{V(0,t)}{I(0,t)} = \frac{V_{+}+V_{-}}{V_{+}-V_{-}}Z_0 = Z_L, \tag{8.5}$$

which results in a relation between the forward and reflected voltage amplitudes V_{+} and V_{-} [8, 12]:

$$\frac{V_{-}}{V_{+}} = \frac{Z_L - Z_0}{Z_L + Z_0} = \Gamma \tag{8.6}$$

where Γ is the reflection coefficient. The reflection coefficient is in general a complex number, with its modulus $0 \leq |\Gamma| \leq 1$, 0 being no reflection and 1 total reflection.

A special case is when $Z_L = Z_0$, in which case the reflection coefficient vanishes, which means that the forward signal is completely absorbed by the load without any reflection. When this special case occurs, the transmission line is said to be terminated on a matched load, as a source cannot distinguish between a line of an infinite length terminated on a

matched load from a truly infinitely long line, since in both cases it will not observe any signal coming back. A matched load thus enables the maximum power transfer.

8.4 Impedance matching

Impedance matching means matching the impedance of a source to that of a load in order to achieve maximum power transfer [8]. A given length of transmission lines if optimised can be used for this purpose [8, 12]. The lines' characteristic impedance (Z_0) is adjusted by changing their widths and the gap between them. The lines' lengths are further optimised in order to transform the load impedance (Z_L) to an equivalent impedance (Z_{eq}) (see Figure 8.3) expressed in Equation 8.7 [8], which can then be equalled to the complex conjugate of a source's impedance (Z_S) (i.e. $Z_{eq} = Z_S^*$), resulting in maximum power transfer between the source and the load [8, 12].

$$Z_{eq} = Z_0 \frac{1+\Gamma e^{-2ikx}}{1-\Gamma e^{-2ikx}} \tag{8.7}$$

where x is the position of the line being considered.

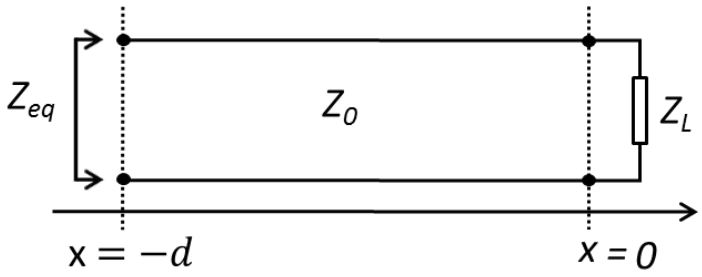

Figure 8.3 – Transformation of load impedance by a length (-d to 0) of a transmission line, resulting in an equivalent impedance Z_{eq} (adapted from [8]).

As well as the impedance-matching between a load and a source being critical for maximising power transfer, it is also vital in improving the signal-to-noise ratio in detection and imaging systems.

8.5 Numerical simulation of the developed impedance matching method used in this project

The method for transforming the equivalent antenna impedance seen by the rectifier used relies on two coplanar strip lines connected to the antenna feed-point, as shown in Figure 8.4(b). The function of the top line is that of an open-circuit stub of length L_{STUB}, whose susceptance B_{STUB} is in parallel to the antenna admittance Y_A. The line on the bottom, of length L_{FEED}, connects the diode to the antenna, and transforms the antenna-stub admittance to match the complex conjugate admittance of the diode Y_D so that:

$$Y_L = Y_D^* = \left[Y_0 \left(\frac{1-\Gamma e^{-2ikL_{FEED}}}{1+\Gamma e^{-2ikL_{FEED}}}\right)\right] \tag{8.8}$$

where

$$\Gamma = \frac{Y_0 - Y_A - iB_{STUB}}{Y_0 + Y_A + iB_{STUB}}, \tag{8.9}$$

is the reflection coefficient at the antenna feed-point,

$$B_{STUB} = Y_0 \tan(k_{STUB} d_{STUB}) \tag{8.10}$$

is the open-circuit stub susceptance, and Y_0 and k are the characteristic admittance and phase velocity of the coplanar strip lines, respectively.

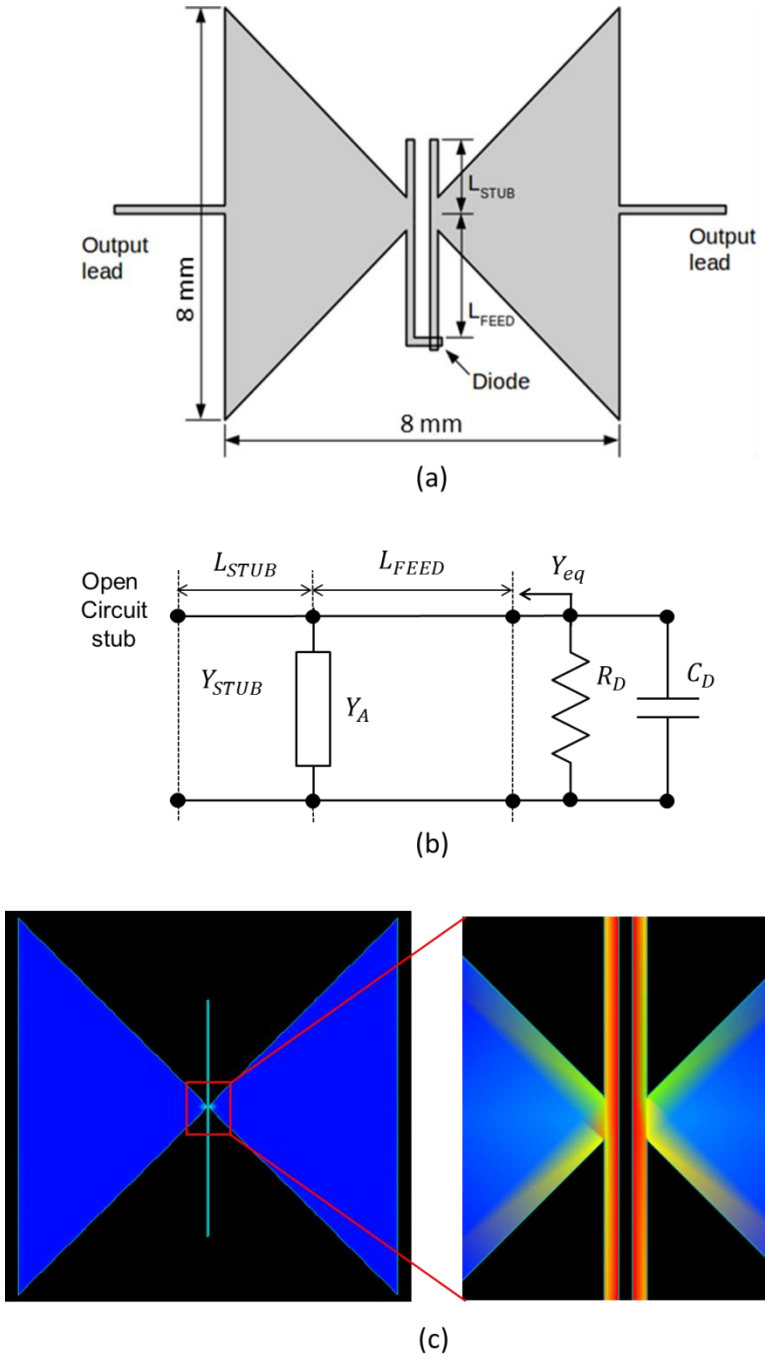

Figure 8.4 – Layout of the model rectenna and matching structure operating at microwave frequencies (a). The rectenna consists of a self-complementary bow-tie and a rectifier. (b) is the equivalent circuit diagram of the device. The parasitic series resistance R_S to the structure is embedded in the lines L_{STUB} and L_{FEED}. (c) is a picture of the simulated structure showing the electromagnetic intensity within it.

A model rectenna operating at microwave frequencies was designed with the self-complementary bow-tie antenna shown in Figure 8.4. The substrate was a low-loss

borosilicate glass (dielectric constant (ε_r) = 4.6, loss tangent (tan δ) = 3.7 x 10^{-3}, measured at room temperature and at a frequency of 1 MHz [13]). The antenna and lines consisted of a bilayer of titanium and gold with a combined thickness of 130 nm and an overall dc conductivity of 46.7 x 10^6 S/m [14]. One of the Ti/OTS/Pt MIM junctions (see Section 5.3) was used as the rectifier. The antenna and coplanar strip lines were modelled and simulated using Agilent Advance Design System (ADS).

As mentioned in Section 8.3, the coplanar strip lines geometry affects the lines' parameters, which are required to design the matching structure. As can be seen in Figure 8.5, the lines' characteristic impedance changes with the gap between the lines. Also, the finite resistance per unit length of the electrode used for the line results in a power loss [8], and needs to be accounted for in order to decouple the losses due to the line from losses due to the substrate used. The measure of losses in the line can be determined from the attenuation constant, a constituent of the line's wave propagation constant (see Equation 8.2).

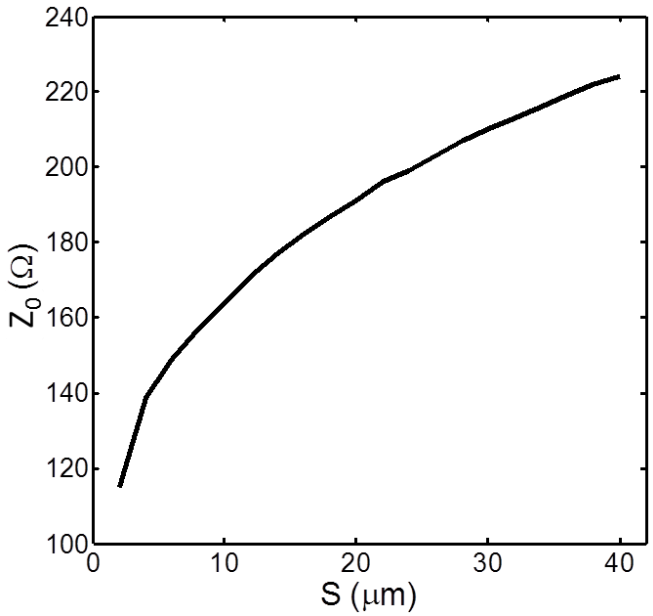

Figure 8.5 – Plot of coplanar strip line's real characteristic impedance as a function of gap between the parallel lines. Operating frequency was kept constant at 20 GHz.

As can be seen in Figure 8.6, the attenuation in the coplanar strip lines decreases as the gap between the lines increases, which was expected because the line characteristic impedance increases with an increase in S. As the characteristic impedance increases, current flowing across the line decreases, and hence the decrease in losses.

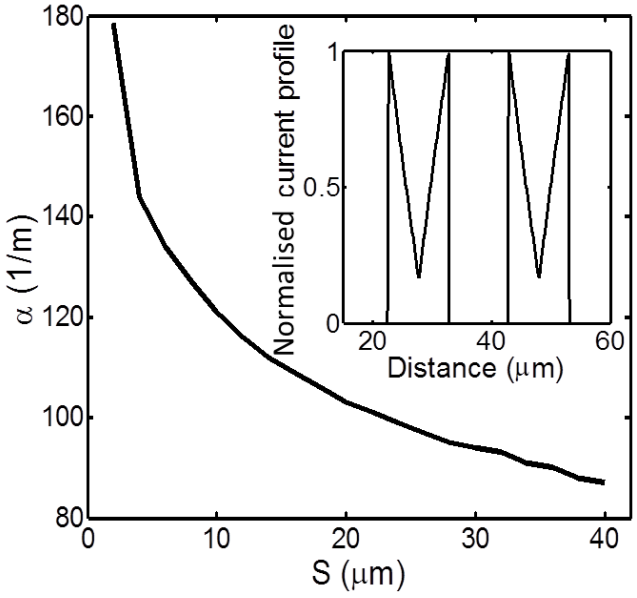

Figure 8.6 – Plot of transmission line attenuation (α) as a function of gap (S) between the parallel lines. In the inset is the typical normalised current profile of the coplanar strip lines. The operating frequency was kept constant at 20 GHz.

The normalised current profile in the inset of Figure 8.6 shows the distribution of current flowing in the lines, with more current densities seen towards the surface of the lines. This is due to skin effect. The distance represents a combination of the line widths and the gap between them, which is 10 μm each.

The coplanar strip lines width and gap were chosen to be 10 μm, which were a good compromise between the line characteristic impedance and losses, as well as fringe capacitances introduced by the line ends. The line dimensions are also compatible with most photolithography equipment and relatively easy to manufacture accurately. The characteristic impedance, propagation velocity and attenuation, as simulated using the

dimensions above, were plotted as a function of frequency in Figure 8.7.

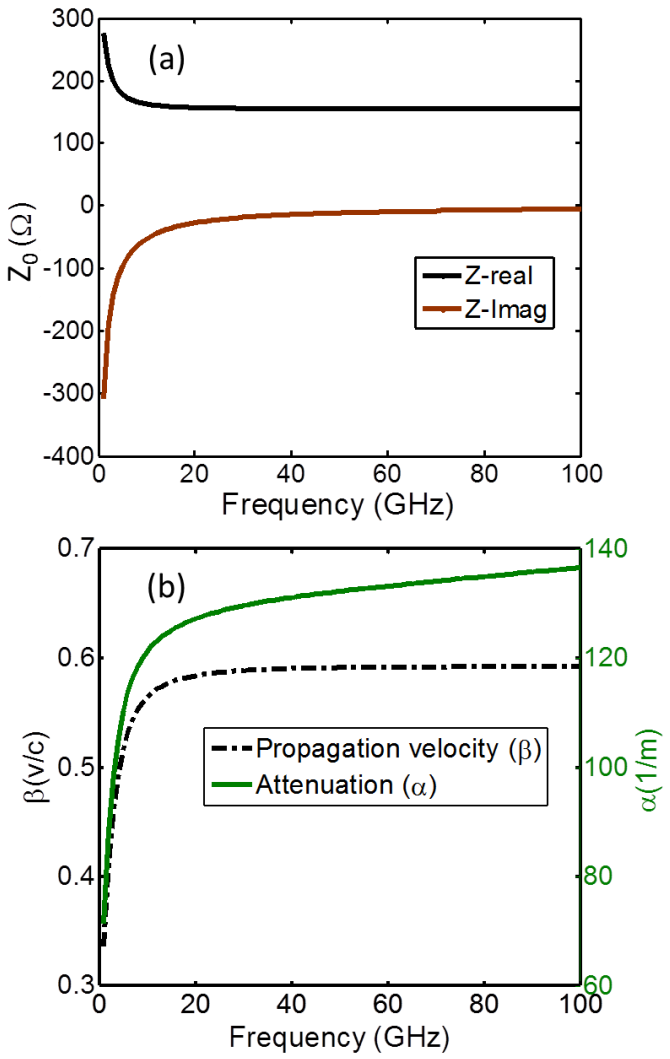

Figure 8.7 – (a) Plot of the coplanar strip line characteristic impedance, and (b) attenuation and propagation velocity as a function of frequency. The gap between the lines was kept constant at 10 µm.

As can be seen, the plotted line parameters show that the line functions well, with the wave propagation velocity at approximately 0.6c at frequencies above 5 GHz. At lower frequencies, the real part of the line characteristic impedance can be seen (see Figure 8.7(a)) to be increasing as the imaginary part decreases. This was expected because, as conductance (*G*) decreases, the line characteristic impedance increases accordingly (see Equation 8.11) [8].

$$Z_0 = \sqrt{\frac{R+j\omega L}{G+j\omega C}} \tag{8.11}$$

where R is the resistance, L is the inductance, G is the conductance and C the capacitance of the line.

Although the experimental work (which will be discussed later on) focusses only on a device operating at microwave frequencies, this technique can hypothetically be ported to devices operating at terahertz frequencies as demonstrated by Figure 8.8.

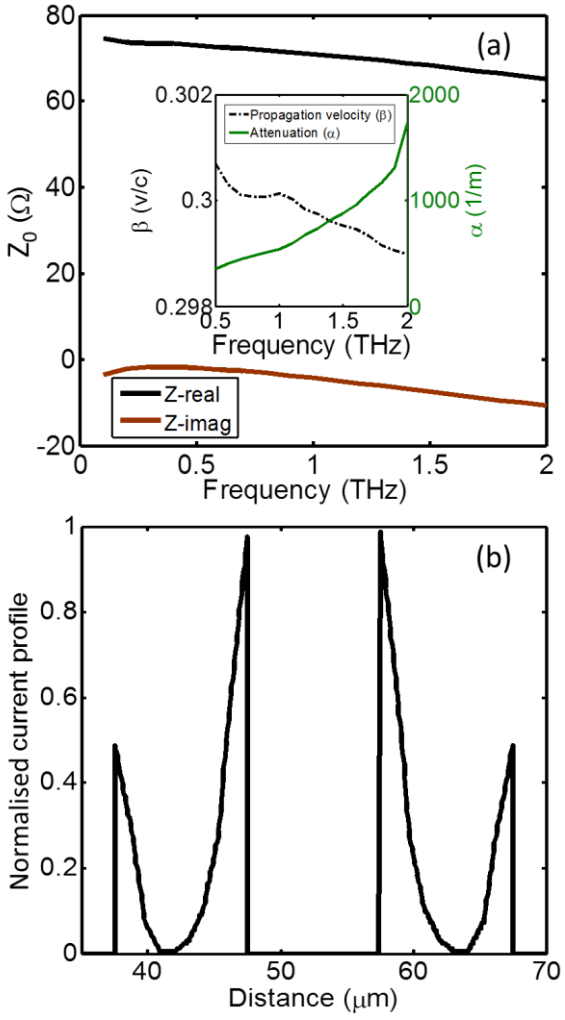

Figure 8.8 – (a) Plot of the terahertz coplanar strip line characteristic impedance, and (b) the normalised current profile of the line at 1 THz operating frequency. The current profile is asymmetric when compared with the microwave lines; this is attributed to dielectric loss and larger skin effect in the line due to the terahertz frequencies. In the inset of (a) is the plot of radiation attenuation, and propagation velocity as a function of frequency.

The terahertz coplanar strip line was modelled with the same electrical parameters as above, but a GaAs substrate ($\varepsilon_r \approx 10.89$), rather than glass ($\varepsilon_r \approx 4.6$) was used. GaAs is a typical substrate used for terahertz applications.

The initial line lengths used for the matching network were determined by solving Equations (8.8)-(8.10). The design was then imported into ADS for the simulation of the device impedance and radiation pattern. The optimal matching was found for $L_{STUB} = 2.26$ mm and $L_{FEED} = 2.74$ mm, dimensions which keep the overall structure compact and introduced only a negligible loss of 0.2 dB in the lines.

The computed antenna impedance at 20 GHz prior to the introduction of the impedance matching network (i.e. the coplanar strip lines) was $Z_A = 97 + i15\ \Omega$ as can be seen in Figure 8.9, whereas the diode impedance was to be $Z_D = (10 + 0.01i)$ kΩ, estimated using the diode junction area and *I*–*V* characteristics. If no matching network were used, a 96% power loss would result due to reflections.

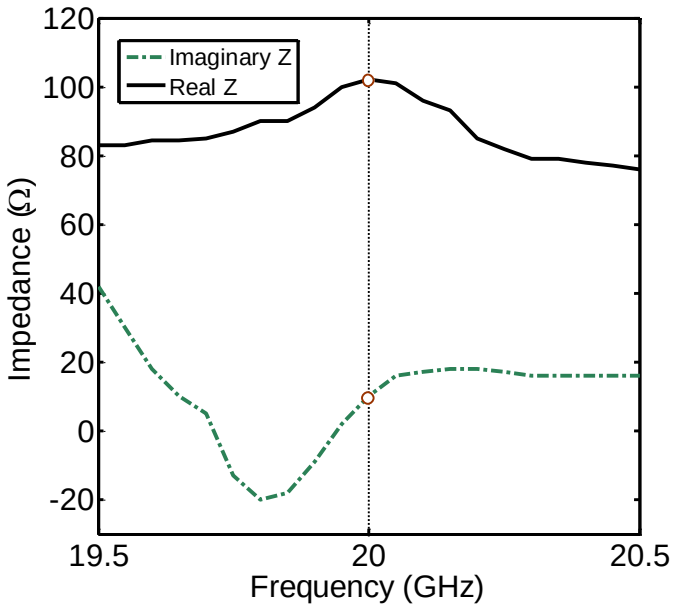

Figure 8.9 – A plot of the designed self-complementary bow-tie antenna computed impedance as a function of frequency before embedding the coplanar strip lines.
The impedance was $Z_A = 97 + i15\ \Omega$ at 20 GHz.

The matching network developed with the technique above was a narrowband one. As expected, after incorporating the matching network (i.e. L_{STUB} and L_{FEED}) into the layout, the antenna exhibited a narrowband behaviour where the desired impedance $Z_A = (10 + 0.01i)$ kΩ was only obtained at a frequency of 20 GHz (see Figure 8.10).

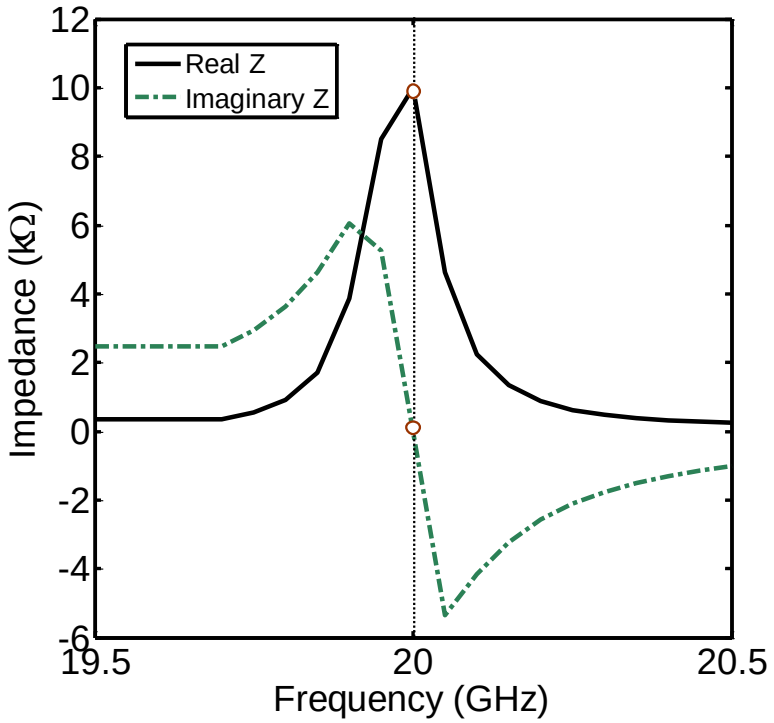

Figure 8.10 – A plot of the designed self-complementary bow-tie antenna computed impedance as a function of frequency after embedding the coplanar strip lines.
The impedance was $Z_A = (10 + 0.01i)$ kΩ at 20 GHz.

8.6 Experimental results and discussion of the implemented impedance-matching technique

8.6.1 The rectenna device fabrication

The control rectenna without a matching network and the rectenna with a matching network were fabricated on a 2 inch borosilicate glass substrate. The antenna patterns were transferred onto the glass wafer by conventional photolithography. A bi-layer of

titanium and of gold with a combined thickness of 130 nm was then deposited as the antenna conducting metal sheet by e-beam evaporation. The gold was selectively etched at the antenna feed-point for the control unmatched structure, and at the coplanar strip line (L_{FEED}) ends for the impedance-matched structure, leaving the titanium at those areas exposed. The exposed titanium was then coated with OTS followed by the deposition of a layer of platinum with a thickness of 40 nm by e-beam evaporation, resulting in the Ti/OTS/Pt junctions. The MIM diode detail fabrication process and OTS deposition can be found in [15] and Section 5.3. Figure 8.11 shows the fabricated control unmatched and impedance-matched rectenna devices.

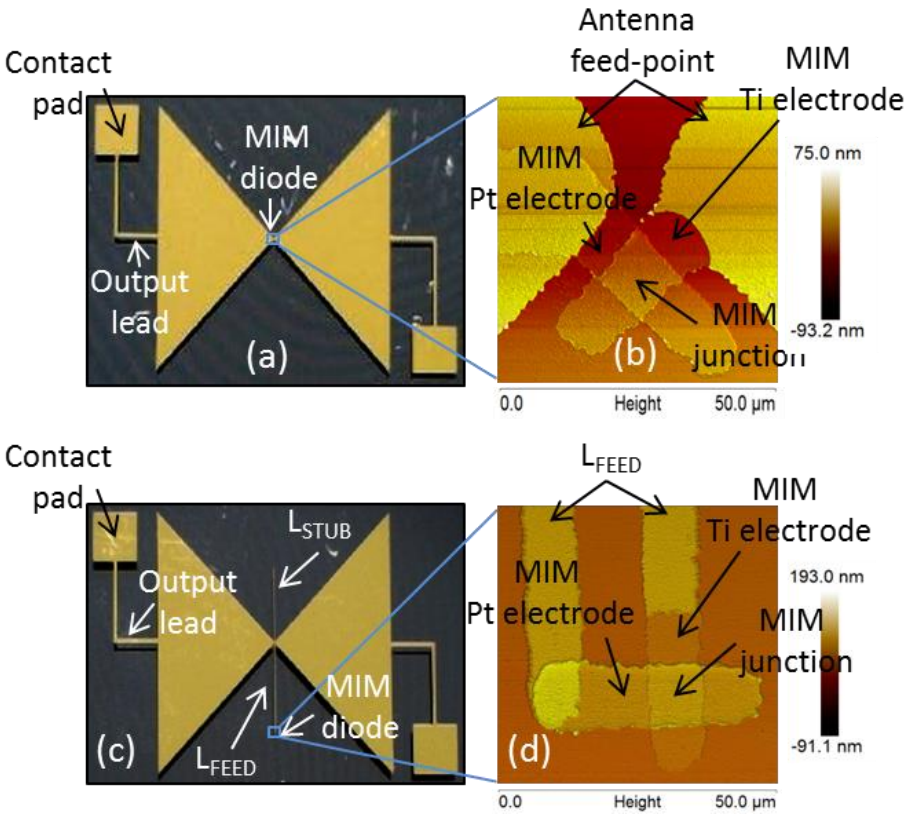

Figure 8.11 – Optical image of the fabricated rectenna devices. (a) Is the control unmatched device, (b) is an atomic force microscopy (AFM) image showing the MIM rectifier connected to the unmatched antenna feed-point, (c) is the matched device with the matching network (coplanar strip line) visible, and (d) is an AFM image showing the MIM rectifier connected to the coplanar strip line ends of the matched device.

8.6.2 Microwave characterisation of the rectenna devices

Microwave tests were performed on the two rectenna topologies using a vector network analyser (VNA) as a power source. The VNA was calibrated using a power meter. A broadband antenna was connected to one of the VNA ports and a mechanical chopper with large apertures was used to intermittently illuminate the rectenna while the signal was read out using a lock-in amplifier. All measurements were performed at room temperature. Figure 8.12 shows the typical set-up for the microwave characterisation.

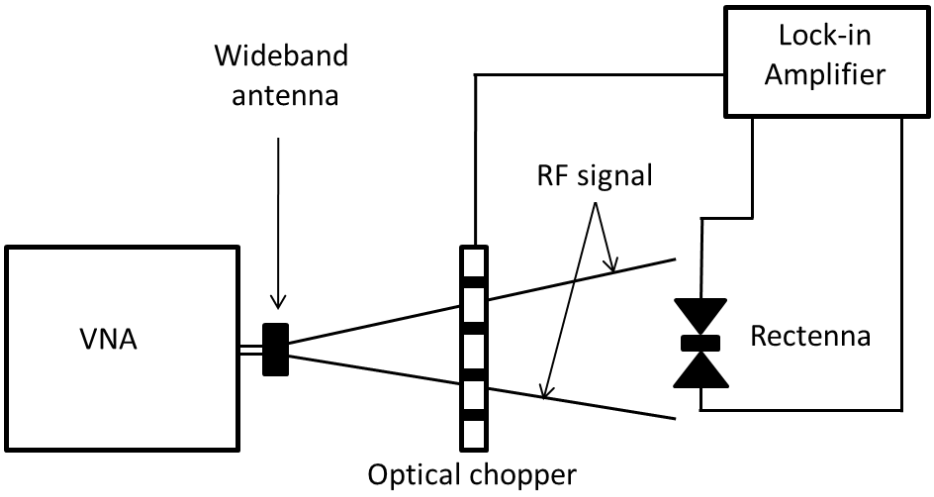

Figure 8.12 – Typical set-up for microwave characterisation of the rectenna devices.

The fabricated device radiation pattern was first measured and compared with that of the simulated model. As expected, the normalised responsivity has a maximum at the normal incidence as $\vartheta = 0$; and the experimental data were in good agreement with the simulated data, as can be seen in Figure 8.13.

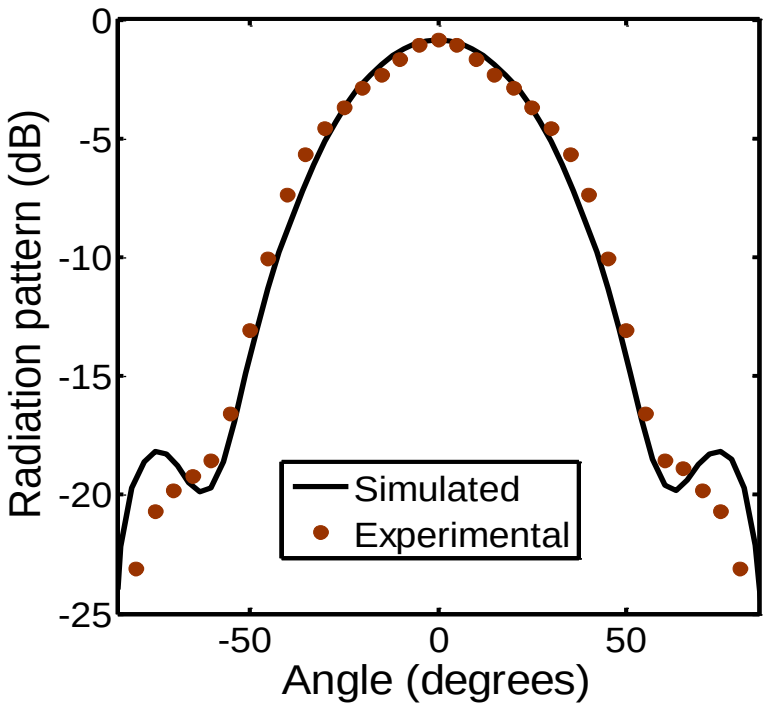

Figure 8.13 – Measured and simulated radiation pattern of the rectenna device in H-plane.

Voltage responsivity of the two rectenna topologies was measured over a frequency range of 19 GHz to 21 GHz (the frequency region where the matching technique was implemented), and a fixed microwave source power of 32 mW (15 dBm). As can be seen in Figure 8.14, the impedance-matched device produced a voltage responsivity almost an order of magnitude higher than the unmatched device. The difference in the responsivity of the two device topologies was calculated by taking the ratio of the responsivity of the matched to that of the unmatched device, and is plotted in the inset of Figure 8.14.

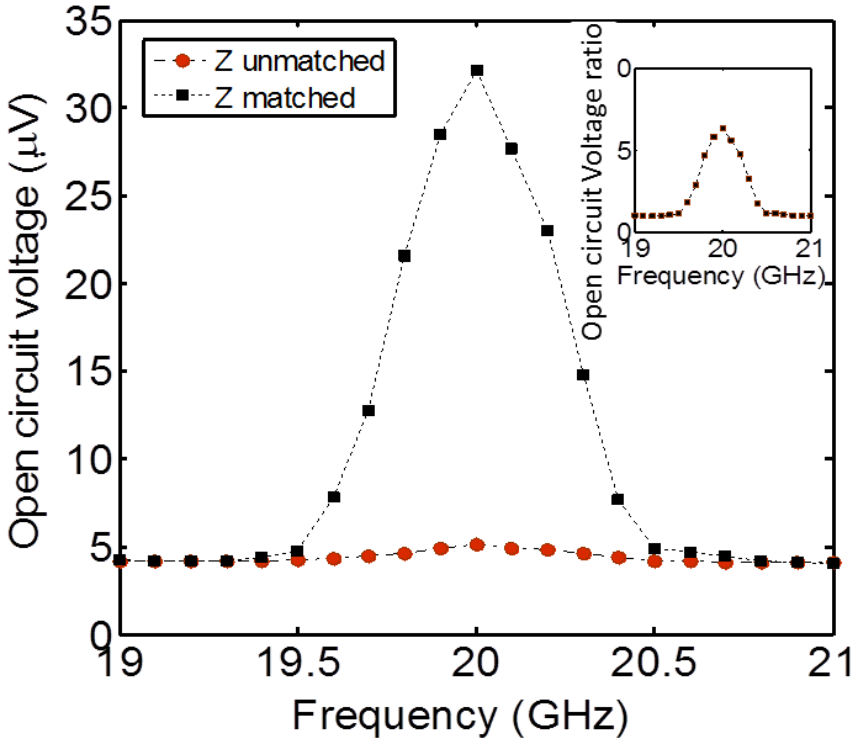

Figure 8.14 – Plot of voltage responsivity as a function of frequency for the impedance-matched and unmatched rectennas. In the inset is the ratio of the outputs of the two device topologies. The operating source power was kept constant at 32 mW (15 dBm).

The voltage and current responsivity of the devices were further tested using a source power ranging from 0.32 mW to 32 mW (-5 dBm to 15 dBm). Figures 8.15(a) and 8.15(b) show the plot of the measured voltage and current responsivity of the two device topologies as a function of source power (with operating frequency kept constant at 20 GHz). As can be seen, the responsivities increased linearly with increase in the source power. Also, the approximately one order of magnitude difference in the responsivities between the matched and unmatched devices can be seen at the source power of 32 mW (15 dBm).

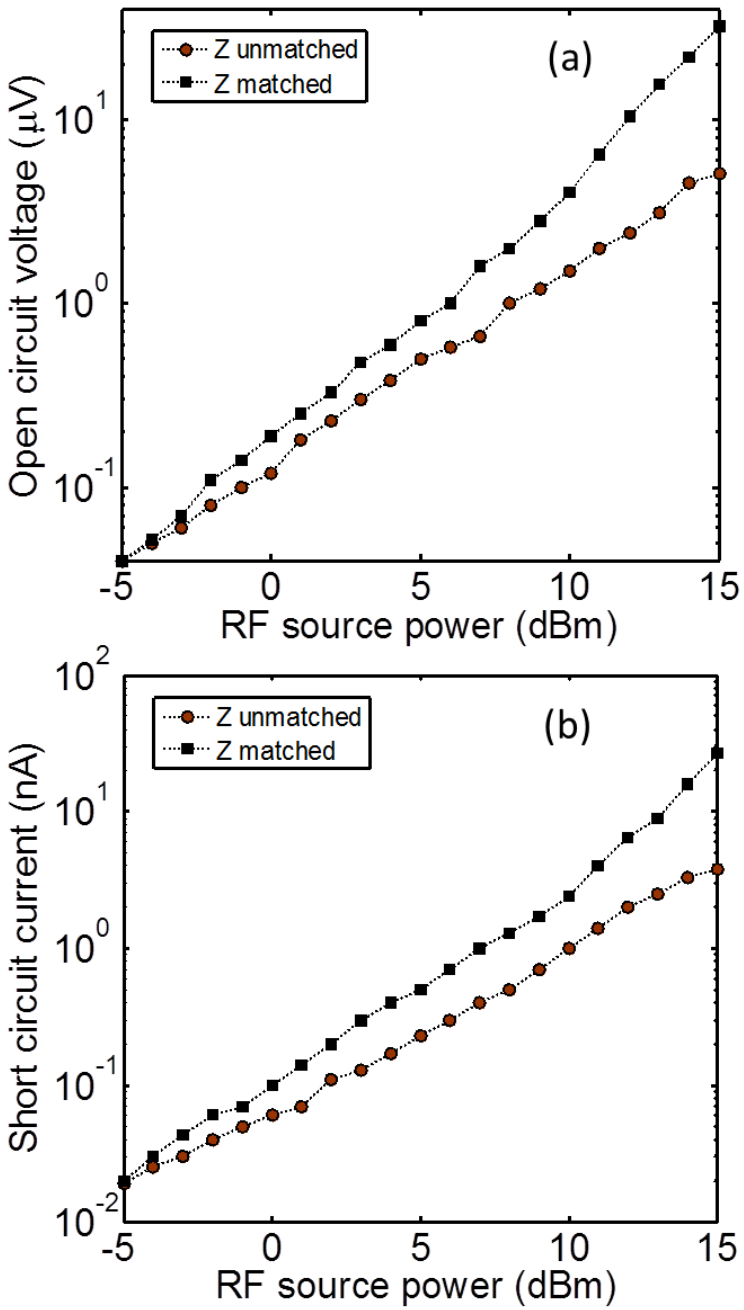

Figure 8.15 – Plot of (a) measured voltage responsivity, and (b) current responsivity as a function of source power for the matched and unmatched devices. The operating frequency was kept constant at 20 GHz.

The effective area of the radiating antenna and of the antennas used in the two rectenna topologies is the same. The antenna gains, line losses, and actual power being radiated and absorbed by the radiating and receiving antennas respectively are irrelevant for the purpose of this work, as we are only interested in the relative difference in the rectified

voltage between the unmatched and matched rectenna devices. Measurements were performed on the two rectenna topologies with the same set-up and under the same conditions.

8.7 Summary

A simple and effective technique to match the low impedance of an antenna to the high impedance of a fast rectifier has been modelled, implemented experimentally and tested in zero-bias rectennas. In the model, the matching network overcame the approximately 96% power loss due to impedance mismatch between the antenna and rectifier. Experimental results showed that the impedance-matched device produced a dramatically enhanced responsivity; seven times more than the unmatched device topology. The design is suitable for applications where efficient narrow-band operation is required, such as radio frequency identification (RFID) devices and energy harvesting (with optimised dimensions), as well as to maximise the signal-to-noise ratio in detection and imaging systems. A broadband impedance matching technique, which involves more complex structure with multiple transmission lines, e.g. the Chebyshev transformer [8], can potentially be developed.

References

[1] R. E. Drullinger, K. M. Evenson, D. A. Jennings, F. R. Petersen, J. C. Bergquist, L. Burkins, and H.U. Daniel, "2.5 THz Frequency Difference Measurements in the Visible Using Metal-Insulator-Metal Diodes", *Appl. Phys. Lett*. Vol. 42, pp. 137-138, (1983).

[2] J. L. Hesler and T. W. Crowe, "NEP and Responsivity of THz Zero-Bias Schottky Diode Detectors", *32nd Int. Conf. Infrared Millimeter Waves (IRMMW)*, pp. 844–845, (2007).

[3] K. J. Siemsen and H. D. Riccius, "Experiments with Point-Contact Diodes in the 30-130 THz Region" *Appl. Phys. Lett*. *A*, Vol. 35, pp. 177-187, (1984).

[4] M. Bareiß, P. M. Krenz, G. P. Szakmany, B. N. Tiwari, D. Kälblein, A. O. Orlov, G. H. Bernstein, G. Scarpa, B. Fabel, U. Zschieschang, H. Klauk, W. Porod, and P. Lugli, "Rectennas Revisited", *Trans. Nanotechnol.* Vol. 12, pp. 1-4, (2012).

[5] Y. Pan, C. V. Powell, A. M. Song, and C. Balocco, "Micro Rectennas: Brownian Ratchets for Thermal-Energy Harvesting", *Appl. Phys. Lett*. Vol. 105, 253901, (2014).

[6] C. H. Lee and Y. H. Chang, "Design of a broadband circularly polarized rectenna for microwave power transmission", *Microwave and Optical Technol. Lett.* Vol. 57, pp. 702-706, (2015).

[7] K. Choi, F. Yesilkoy, G. Ryu, S. H. Cho, N.l Goldsman, M. Dagenais, and M. Peckerar, "A Focused Asymmetric Metal–Insulator–Metal Tunneling Diode: Fabrication, DC Characteristics and RF Rectification Analysis," *IEEE Trans. Electron Devices*, Vol. 58, No. 10, pp. 3519-3528, (2011).

[8] D. M. Pozar, "Microwave Engineering*," 4th Edition, published by John Wiley & sons, Inc. Hoboken, NJ,* pp. 48-87, 228-268, (2011).

[9] W. R. Eisenstadt, and Y. Eo, "S-Parameter-Based IC Interconnect Transmission Line Characterisation," *IEEE Trans. Compon. Hybrid Manuf. Technol*. Vol. 15, No. 4, pp. 428-490, (1992).

[10] M. Y. Frankel, S. Gupta, J. A. Valdmanis, and G. A. Mourou, "Terahertz Attenuation and Dispersion Characteristics of Coplanar Transmission Lines," *IEEE Trans. Microwave Theory Tech.* Vol. 39, No. 6, pp. 910-916, (1991).

[11] E. M. T. Jones, and J. T. Bolljahn, "Coupled-Strip-Transmission-Line Filters and Directional Couplers," *lRE Trans. Microwave Theory Tech.* Vol. 4, Issue 2, pp. 75-81, (1956).

[12] R. E. Collin, "Foundations for Microwave Engineering," 2nd Edition, published by Wiley-IEEE Press, pp. 72-180, 303-393, (2000).

[13] SCHOTT BOROFLOAT ® 33 http://psec.uchicago.edu/glass/borofloat_33_e.pdf, Accessed online: 05 September 2016.

[14] TIBTECH "Properties table of Stainless steel, Metals and other Conductive materials," http://www.tibtech.com/conductivity.php, Accessed online: 03 December 2016.

[15] D. Etor, L. E. Dodd, D. Wood and C. Balocco, "An Ultrathin Organic Insulator for Metal–Insulator–Metal Diodes," *IEEE Trans. Electron Devices,* Vol. 63, No 7, pp. 2887–2891, (2016).

Chapter 9

Conclusions and Suggestions for Future Work

9.1 Conclusions

There is a high demand for rectenna devices for potential applications such as high frequency signals rectification, thermal imaging, detection of terahertz radiation, and the recovery of heat energy [1-3]. The optical rectenna, which consist of a rectifier coupled to an antenna, is a good device choice for these applications if optimised. Fast rectifiers, such as MIM junctions, Schottky diodes, and more recently the self-switching nanodiodes, can be used as the rectifying component [3-5] due to their high inherent speed. The major drawback of the rectenna device, however, is the relatively low external conversion efficiency, caused mainly by the mismatch between the impedance of the antenna and that of the rectifier [5].

Although there are varieties of devices that can be used as the rectifying component for the rectenna, this thesis focused on the MIM diode as a rectifier. The MIM diode consists of two metals separated by an insulating layer which must be thin, corresponding to only a few atomic layers. With the conventional deposition methods, such as furnace oxidation

and plasma-etch [6-8], this often results in a defective layer [7-8], with a large number of pin holes, short-circuiting the diode terminals and drastically reducing yield.

In order to overcome these problems, the work presented in this thesis investigated:

- The use octadecyltrichlorosilane (OTS), which self-assembles as a monolayer onto the surface of a metal, as an alternative method for depositing a thin insulator for MIM junctions. OTS consists of carbon chains strongly packed together with an overall thickness of approximately 2 nm. Due to the nature of self-assembly, a second layer cannot grow on top of the first one, resulting in a uniform thickness over large areas determined by the SAM chemistry [9, 10].
- The manufacture of MIM diodes on a flexible plastic substrate (which is an added advantage particularly in the emerging field of plastic electronics where flexibility is a key property), on the back of the successful production of the OTS insulator junctions, since the OTS deposition is a low temperature process. The low temperature process not only provides reduced production costs, but also presents the possibility of roll-to-roll volume manufacture of MIM diodes.
- An effective method for narrow-band matching of the impedance of an antenna to that of a rectifier in order to improve power transfer between the two components and, consequently, result in a more efficient rectenna device.

Subsequently, 2 µm x 2 µm in dimensions MIM diodes with Ti/OTS/Pt layers have been successfully fabricated on a borosilicate glass substrate and tested. DC and AC electrical results obtained are among the best published, with a high yield of working devices. Electrical results were also found to be uniform and consistent between different diodes, as well as repeatable. These demonstrated that the OTS deposition technique was effective. The transport mechanism occurring in the device was also investigated. It was found that electron tunneling was the dominant transport mechanism occurring in the

diode for temperature of 2.5 K up to approximately 25 K, while emission transport mechanisms dominated the transport of electron from temperature of approximately 25 K up to room temperature. This implies that the transport mechanism that would be dominating in the device for most application is the emission transport mechanisms, as most of the potential applications operates at room temperature or higher.

The Ti/OTS/Pt diodes were found to be unaffected by temperature up to approximately 450 °C, compared to a typical Ti/TiO_x/Pt diode, which starts to degrade at approximately 200 °C. This is significant in thermal energy harvesting applications, where the diodes may be exposed to high temperature environments. An encapsulation method to prevent MIM diodes current degradation due to the atmosphere (water vapour and oxygen) penetrating through the MIM junction and oxidising the Ti layer has also been developed.

The Ti/OTS/Pt device with 10 µm x 10 µm dimensions has also been successfully fabricated on a flexible plastic substrate, with electrical results similar to those of the devices fabricated on a (rigid) borosilicate glass substrate. This MIM structure is therefore suitable for applications where a large area and a low manufacturing cost are of paramount importance, such as radio-frequency identification (RFID) tags operating at for example 980 MHz [11-14], and energy harvesting if the structure dimensions are further optimised [12-14]. Also, this has opened up the possibility of roll-to-roll volume manufacturing of fast MIM diodes.

The DC electrical results of the OTS devices were compared with those of diodes fabricated using ALD. The ALD device produced slightly better results, in terms of current density, and zero-bias curvature coefficient. Although the DC results of the ALD diodes were slightly better, the advantages the OTS diodes presents, such as low-cost of production, low-temperature manufacturing process and the possibility for the roll-to-roll volume manufacture of MIM devices, cannot be ignored. It would be a case of making a choice

between a slight improvement in electrical parameters and huge difference in robustness and production cost, with the OTS device being the cheaper one.

Furthermore, a simple and elegant impedance-matching method for rectennas operating in a narrow frequency range has been developed. The method used two coplanar strip lines emerging from the antenna feed-point, to correct for the reactive component of the antenna impedance on one side, and to connect the rectifier and transform its impedance on the other side. Microwave characterisation of the fabricated devices (impedance-matched and non-matched) showed that the responsivity of the impedance-matched rectenna was almost an order of magnitude higher at 20 GHz than that of a control device without a matching network. The experimental results were supported by numerical simulations, which suggest that the same impedance matching technique can be used for mm-waves and THz radiation.

9.2 Suggestions for future work

The smallest Ti/OTS/Pt junctions fabricated were 2 µm x 2 µm in dimension, which was thought to be a major factor limiting its cut-off frequency, as an extrapolation of the device cut-off frequency showed that these diodes would be fast enough to rectifying terahertz signals if they were fabricated with feature sizes in the sub 100 nm range. These feature sizes cannot be achieved using the conventional photolithography process. Electron beam lithography (EBL) could be used to achieve these feature sizes but is a very slow process. A good technique that could be used is the nano-transfer printing (nTP) [15]. It involves transfer-printing of nanostructured metal from a stamp onto a substrate of interest. Trenches are created on the surface of a wafer (usually silicon), which serves the stamp, using a combination of EBL and dry etching to produce raised nanometre thick lines. The wafer is then coated with a SAM, which makes the surface of the wafer hydrophobic, to

enhance delamination of metals [15]. The wafer is then coated with metal, with the metal on the raised nanometre thick lines being transferred by stamping it onto the substrate of interest. With this stamp, nanometer scale MIM junctions can be fabricated, and can be used to rectify terahertz signals. The stamp is reusable [15].

The impedance-matching structure developed in this project is a narrowband. A broadband matching technique, which involves more complex structure with multiple transmission lines, for example the Chebyshev transformer [16], can potentially be developed. This will broaden the potential applications in which the rectenna could be used.

References

[1] R. E. Drullinger, K. M. Evenson, D. A. Jennings, F. R. Petersen, J. C. Bergquist, L. Burkins, and H.U. Daniel, "2.5 THz Frequency Difference Measurements in the Visible Using Metal-Insulator-Metal Diodes", *Appl. Phys. Lett*. Vol. 42, pp. 137-138, (1983).

[2] K. J. Siemsen and H. D. Riccius, "Experiments With Point-Contact Diodes in the 30-130 THz Region" *Appl. Phys. Lett*. *A*, Vol. 35, pp. 177-187, (1984).

[3] Y. Pan, C. V. Powell, A. M. Song, and C. Balocco, "Micro Rectennas: Brownian Ratchets for Thermal-Energy Harvesting", *Appl. Phys. Lett*. Vol. 105, 253901, (2014).

[4] C. H. Lee and Y. H. Chang, "Design of a Broadband Circularly Polarized Rectenna for Microwave Power Transmission", *Microwave and Optical Technol. Lett.* Vol. 57, pp. 702-706, (2015).

[5] J. L. Hesler and T. W. Crowe, "NEP and Responsivity of THz Zero-Bias Schottky Diode Detectors", *32nd Int. Conf. Infrared Millimeter Waves (IRMMW),* pp. 844 – 845, (2007).

[6] L. E. Dodd, A. J. Gallant, and D. Wood, "Ti-TiOx-Pt Metal-Oxide-Metal Diodes Fabricated via a Simple Oxidation Technique", *MRS Proceedings*, Vol. 1415, pp. 1-4, (2012).

[7] L. E. Dodd, A. J. Gallant, and D. Wood, "Controlled Reactive ion Etching and Plasma Regrowth of Titanium Oxides of Known Thickness for Production of Metal-Oxide-Metal Diodes", *IET Micro and Nano Letters*, Vol. 8, No. 8, pp. 476-478, (2013).

[8] L. E. Dodd, "Fabrication Optimization of Metal-Oxide-Metal Diodes", *PhD thesis*, pp 127-132, http://etheses.dur.ac.uk/9474/1/Linzi_Dodd_d51hqe_thesis.pdf?, Accessed online: 04 July 2016.

[9] T Kawanagoa, and S. Oda, “Utilizing Self-Assembled-Monolayer-Based Gate Dielectrics to Fabricate Molybdenum Disulfide Field-Effect Transistors” *Appl. Phys. Lett.* Vol. 108, pp. 041605, (2016).

[10] M. Rittner, M. S. Martin-Gonzalez, A. Flores, H. Schweizer, F. Effenberger, and M. H. Pilkuhn, “Nanostructural and Electrical Properties of Functionally Terminated Self-Assembled Monolayers on Silicon Surfaces” *J. Appl. Phys.* Vol. 98, pp. 054312, (2005).

[11] V. Subramanian, P. C. Chang, J. B. Lee, S. E. Molesa, and S. K. Volkman, “Printed Organic Transistors for Ultra-Low-Cost RFID Applications” *IEEE Trans. Compon. Packag. Technol,* Vol. 28, Issue 4, PP. 742-747, (2005).

[12] R. A. Potyrailo, W. G. Morris, T. Sivavec, H. W. Tomlinson, S. Klensmeden, and K. Lindh, “RFID Sensors Based on Ubiquitous Passive 13.56-Mhz RFID Tags and Complex Impedance Detection” *Wireless Commun. Mob. Comput.* Vol. 9, pp. 1318-1330, (2009).

[13] H. T. Hsu, and T. J. Huang, “A Koch-Shaped Log-Periodic Dipole Array (LPDA) Antenna for Universal Ultra-High-Frequency (UHF) Radio Frequency Identification (RFID) Handheld Reader” *IEEE Trans. Antennas Propag.* Vol. 61, No. 9, pp. 4852-4856, (2013).

[14] K. Myny, S. Steudel, P. Vicca, J. Genoe, and P. Heremans, “An Integrated Double Half-Wave Organic Schottky Diode Rectifier on Foil Operating at 13.56 MHz” *Appl. Phys. Lett.* Vol. 93, pp. 093305, (2008).

[15] M. Bareiß, D. Kälblein, C. Jirauschek, A. Exner, I. Pavlichenko, B. Lotsch, U. Zschieschang, H. Klauk, G. Scarpa, B. Fabel, W. Porod, and P. Lugli, “Ultra-Thin Titanium Oxide”, *Appl. Phys. Lett.* Vol. 101, pp. 083113, (2012).

[16] D. M. Pozar, “Transmission Line Theory,” in Microwave Engineering, 4th ed. New York, NY, USA: Wiley, pp. 48–51, 228–271, 2011.